

N 7 3 - 1 2 6 9 2

**CASE FILE  
COPY**

Report L-910900-12

Development of RF Plasma Simulations  
of In-Reactor Tests of Small Models  
of the Nuclear Light Bulb Fuel Region

NASA Contract No. SNPC-70

**CASE FILE  
COPY**

**U**  
UNITED AIRCRAFT CORPORATION  
**A**

**United Aircraft Research Laboratories**

EAST HARTFORD, CONNECTICUT

# United Aircraft Research Laboratories



EAST HARTFORD, CONNECTICUT 06108

Report L-910900-12

Development of RF Plasma Simulations  
of In-Reactor Tests of Small Models  
of the Nuclear Light Bulb Fuel Region

NASA Contract No. SNPC-70

REPORTED BY Ward C. Roman  
Ward C. Roman

Jerome F. Jaminet  
Jerome F. Jaminet

APPROVED BY James W. Clark  
James W. Clark, Chief  
Fluid and Systems Dynamics

DATE September 1972

NO. OF PAGES 130

COPY NO. 26

# United Aircraft Research Laboratories



October 13, 1972

National Aeronautics and Space Administration  
Office of Scientific and Technical Information  
Washington, D. C. 20546  
Attention: AFSS-LL

Subject: Transmittal of reports comprising the Final Technical Report under Contract SNPC-70, "Investigation of Gaseous Nuclear Rocket Technology"

Enclosures: (A) Report L-910900-12 (F) Report L-910900-17  
(B) Report L-910900-13 (G) Report L-910904-3  
(C) Report L-910900-14 (H) Report L-990929-3  
(D) Report L-910900-15 (I) Report L-910905-13  
(E) Report L-910900-16

Gentlemen:

Copies of nine reports, Enclosures (A) through (I), which comprise the Final Technical Report under Contract SNPC-70 between the joint AEC-NASA Space Nuclear Systems Office and the Research Laboratories of United Aircraft Corporation, are being sent to you as part of the general distribution of reports under this Contract.

Very truly yours,

UNITED AIRCRAFT CORPORATION  
Research Laboratories

*George H. McLafferty*  
George H. McLafferty  
Senior Program Manager

Encl.

GHM:bwz

FOREWORD

An exploratory experimental and theoretical investigation of gaseous nuclear rocket technology was conducted by the United Aircraft Research Laboratories under Contract SNPC-70 with the joint AEC-NASA Space Nuclear Systems Office. The Technical Supervisors of the Contract for NASA were Captain C. E. Franklin (USAF) of SNSO for the initial portion of the Contract performance period, and Dr. Karlheinz Thom of SNSO and Mr. Herbert J. Heppler of the NASA Lewis Research Center for the final portions. The following nine reports (including the present report) comprise the required Final Technical Report under the Contract:

1. Roman, W. C. and J. F. Jaminet: Development of RF Plasma Simulations of In-Reactor Tests of Small Models of the Nuclear Light Bulb Fuel Region. United Aircraft Research Laboratories Report L-910900-12, September 1972. (Present report)
2. Klein, J. F.: Nuclear Light Bulb Propellant Heating Simulation Using a Tungsten-Particle/Argon Aerosol and Radiation from a DC Arc Surrounded by a Segmented Mirror Cavity. United Aircraft Research Laboratories Report L-910900-13, September 1972.
3. Jaminet, J. F.: Development of a Model and Test Equipment for Cold-Flow Tests at 500 Atm of Small Nuclear Light Bulb Configurations. United Aircraft Research Laboratories Report L-910900-14, September 1972.
4. Kendall, J. S. and R. C. Stoeffler: Conceptual Design Studies and Experiments Related to Cavity Exhaust Systems for Nuclear Light Bulb Configurations. United Aircraft Research Laboratories Report L-910900-15, September 1972.
5. Rodgers, R. J. and T. S. Latham: Analytical Design and Performance Studies of the Nuclear Light Bulb Engine. United Aircraft Research Laboratories Report L-910900-16, September 1972.
6. Latham, T. S. and R. J. Rodgers: Analytical Design and Performance Studies of Nuclear Furnace Tests of Small Nuclear Light Bulb Models. United Aircraft Research Laboratories Report L-910900-17, September 1972.
7. Krascella, N. L.: Spectral Absorption Coefficients of Argon and Silicon and Spectral Reflectivity of Aluminum. United Aircraft Research Laboratories Report L-910904-3, September 1972.



8. Palma, G. E.: Measurements of the UV and VUV Transmission of Optical Materials During High-Energy Electron Irradiation. United Aircraft Research Laboratories Report L-990929-3, September 1972.
9. Kendall, J. S.: Investigation of Gaseous Nuclear Rocket Technology -- Summary Technical Report. United Aircraft Research Laboratories Report L-910905-13, September 1972.

Report L-910900-12

Development of RF Plasma Simulations of In-Reactor Tests  
of Small Models of the Nuclear Light Bulb Fuel Region

TABLE OF CONTENTS

	<u>Page</u>
SUMMARY . . . . .	1
RESULTS AND CONCLUSIONS . . . . .	3
INTRODUCTION. . . . .	6
DESCRIPTION OF PRINCIPAL EQUIPMENT. . . . .	9
UARL 1.2-MW RF Induction Heater . . . . .	9
Background . . . . .	9
Primary Heater Components and Test Tank. . . . .	9
Argon Gas and Cooling Water Flow Systems . . . . .	11
Plasma Starting System . . . . .	11
Test Chambers. . . . .	12
Diagnostic Equipment, Test Procedures and Data Analysis Methods . . . . .	12
Total Radiation Measurements . . . . .	12
Photographic Equipment and Viewing System for Recording and Observing Plasma Behavior. . . . .	13
Optical Scanning System for Determination of Plasma Diameter . . . . .	14
Spectral Emission Measurements . . . . .	14
Optical System for Determining "Edge-of-Plasma" Location . . . . .	15
Determination of Energy Balance. . . . .	15
Determination of Source Radiation Characteristics. . . . .	16
RADIANT ENERGY SOURCE RESEARCH. . . . .	17
RF Plasma Tests with 7/8-Scale IRG Fused Silica Pressure Vessel	
Configuration . . . . .	17
Background . . . . .	17
Objective. . . . .	17
Basic Test Configuration . . . . .	17
Test Procedures. . . . .	19
Discussion of Test Results . . . . .	19

## TABLE OF CONTENTS (Continued)

	<u>Page</u>
RF Plasma Tests with 7/8-Scale IRG Filament-Wound Pressure	
Vessel Configuration . . . . .	23
Background . . . . .	23
Objective . . . . .	23
Basic Test Configuration . . . . .	23
Test Procedures . . . . .	25
Discussion of Test Results . . . . .	25
SIMULATED-FUEL INJECTION RESEARCH . . . . .	28
Particle Feeder System . . . . .	28
Background . . . . .	28
Objective . . . . .	28
Description of Equipment and Procedures . . . . .	29
Discussion of Test Results . . . . .	30
RF Plasma Tests at Pressures up to 40 Atm Using 7/8-Scale IRG	
Configuration and Tungsten Particle Feeder System . . . . .	32
Background . . . . .	32
Objective . . . . .	32
Description of Configuration and Procedures . . . . .	32
Discussion of Test Results . . . . .	33
RF Plasma Tests at Pressures up to 40 Atm Using 7/8-Scale IRG	
Configuration and Injection of Uranium Hexafluoride (UF <sub>6</sub> ) . . . . .	35
Background . . . . .	35
Objective . . . . .	36
Description of Equipment and Procedures . . . . .	36
Discussion of Test Results . . . . .	38
Simulated-Fuel Containment Measurement Techniques . . . . .	41
Background . . . . .	41
Objective . . . . .	41
Discussion of Results . . . . .	41
TRANSPARENT-WALL MODEL RESEARCH . . . . .	46
RF Plasma Tests with Axial-Coolant-Tube Transparent-Wall Models . . . . .	46
Background . . . . .	46
Objective . . . . .	47
Description of Equipment and Procedures . . . . .	48
Discussion of Test Results . . . . .	50

TABLE OF CONTENTS (Continued)

	<u>Page</u>
REFERENCES . . . . .	54
LIST OF SYMBOLS . . . . .	58
APPENDIX A: SUPPORTING RESEARCH WITH TUNGSTEN PARTICLES AND PARTICLE FEEDER SYSTEMS . . . . .	61
APPENDIX B: RADIATION CHARACTERISTICS AND PROPERTIES OF NIGROSINE DYE. . . .	65
TABLES. . . . .	67
FIGURES . . . . .	73

Development of RF Plasma Simulations of In-Reactor Tests  
of Small Models of the Nuclear Light Bulb Fuel Region

SUMMARY

Experiments were conducted to develop test configurations and technology necessary to simulate the thermal environment and fuel region expected to exist in in-reactor tests of small models of nuclear light bulb configurations. Particular emphasis was directed at rf plasma tests of approximately full-scale models of an in-reactor cell suitable for tests in Los Alamos Scientific Laboratory's Nuclear Furnace. The in-reactor tests will involve vortex-stabilized fissioning uranium plasmas of approximately 200-kW power, 500-atm pressure and equivalent black-body radiating temperatures between 3220 and 3510°K.

The test program was conducted using the UARL 1.2-MW rf induction heater operating with 8.6-cm-i.d. work coils at approximately 5.4 MHz. One portion of the program employed a fused silica pressure vessel in the test configuration --- a 15.5-cm-long chamber with an inside diameter of 5.7 cm. The end walls of this chamber were made of copper; they were water cooled and were polished to increase surface reflectivity. Argon gas, injected at the periphery of each end wall, was used to drive the vortex. Chamber pressures up to 42 atm, rf plasma power levels up to 180 kW, and equivalent black-body radiating temperatures up to 4320°K were attained. In other rf tests, an opaque fiberglass filament-wound pressure vessel was used. These tests demonstrated the structural integrity of the vessel in the rf electrical and thermal environments at pressures up to 43 atm and total power levels up to 203 kW. Similar vessels have previously been hydrostatically tested to 550 atm; i.e., above the pressure level expected to be required in future rf and in-reactor tests.

The maximum operating pressure levels in the rf plasma tests were limited primarily by the water pumps and plumbing installed at the 1.2-MW rf heater facility. A gas and water-cooling system which can be used for future rf plasma tests up to 500 atm has been developed and is now available. The maximum power levels were determined by operating limits on the dc current from the 1.2-MW power supply; these limits permitted achieving the goals of the present program. The limits can be increased, if required, for future tests.

Another portion of the program involved tests with condensible simulated fuels --- micron-sized tungsten particles and gaseous uranium hexafluoride --- injected into the rf plasma. To permit injection of the particulate fuel in a steady and

controlled manner into the 40-atm rf plasma environment, a particle feeder system was developed and tested. This design can be extended for operation at 500 atm.

An important area of research in future rf tests is to contain sufficient amounts of fuel for simulating the nuclear tests. In preparation for these tests, an analytical investigation of several methods suitable for measuring the amount of simulated fuel in the plasma and, if possible, its density distribution, was conducted. Two methods were selected as most promising: a time-of-flight mass spectrometer technique and an x-ray absorption technique. These techniques are applicable to rf plasma tests up to 500 atm in which opaque filament-wound pressure vessels are used.

Additional tests were conducted with thin-walled fused-silica transparent walls similar to the transparent walls of a nuclear light bulb engine. Using axial tube wall thicknesses down to 0.125 mm, tests were conducted at pressures up to 35 atm and total discharge powers up to 193 kW. The walls were successfully cooled at total incident heat fluxes (radiation and conduction) up to 1.5 kW/cm<sup>2</sup>, compared with an estimated 0.4 kW/cm<sup>2</sup> net radiant heat flux expected in in-reactor tests.

RESULTS AND CONCLUSIONS

1. RF plasma tests of an in-reactor configuration which had a fused silica pressure vessel, but did not have simulated-fuel injection, yielded the following results:

- (a) The maximum chamber pressure reached was 42 atm --- twice as high as in prior tests, and limited primarily by the characteristics of the installed water-cooling equipment.
- (b) The maximum power deposited into the plasma was 180 kW --- about the same as the power expected in the Nuclear Furnace in-reactor tests.
- (c) The maximum radiant energy flux at the surface of the plasma was approximately 2 kW/cm<sup>2</sup> --- about three times as large as the flux expected in the in-reactor tests. The corresponding equivalent black-body radiating temperature is 4320°K, compared with 3220 to 3510°K expected in the in-reactor tests.
- (d) The fraction of total discharge power that was radiated through the inner transparent wall (i.e., the radiation efficiency) increased only gradually with increasing pressure, reaching approximately 0.75 at 40 atm.
- (e) The plasma was cylindrical over most of its length and had conically shaped end regions. Although the pressure, the power in the discharge and the argon weight flow rate were varied over wide ranges, the diameter of the plasma at the axial midplane varied only over the range from 1.65 cm to 2.1 cm, compared with the peripheral-wall i.d. of 5.7 cm.
- (f) View ports at several radii in the end walls were successfully used to observe the "edge-of-plasma" location. This method appears applicable in future rf tests at high pressures where the opaque filament-wound pressure vessel will preclude direct viewing of the plasma from the side.

2. RF plasma tests of a similar configuration which had an opaque filament-wound pressure vessel, also without simulated-fuel injection, resulted in the following:

- (a) The maximum chamber pressure reached was 43 atm; the maximum power deposited into the plasma was 203 kW. In prior tests, similar pressure levels were attained; however, the maximum power level exceeded that of the prior tests by a factor of four.

- (b) Comparisons of the measured electrical, fluid dynamic and heat transfer quantities with measurements made during tests of the model having a fused silica pressure vessel indicated no significant differences in the plasma characteristics. Thus, the radiation efficiency was approximately 0.75 at 40 atm, and the flux exceeded that expected in the in-reactor tests, in both the fused silica and filament-wound pressure vessel models.
- (c) No potential limitations were found in these tests which would prevent use of filament-wound pressure vessels in future rf plasma tests up to 500 atm.

3. The following results were obtained in the portion of the program directed toward development of fuel injection technology for rf plasma and in-reactor tests:

- (a) A particle feeder system was developed that is capable of injecting approximately micron-sized tungsten particles in a steady and controlled manner at pressures up to 40 atm. The design of this system can be extended for operation at pressures up to 500 atm.
- (b) RF plasma tests with simulated-fuel injection in the form of tungsten particles in argon carrier gas were conducted, using the in-reactor configuration having a fused silica pressure vessel. At radiant energy flux levels about equal to those expected in the in-reactor tests and at chamber pressures up to 40 atm, the simulated fuel was injected into the plasma region through probes located at the centers of the end walls. The mass fraction (i.e., the tungsten weight flow rate divided by the sum of the tungsten weight flow rate and the argon carrier gas weight flow rate) at the 40-atm test condition was 0.4; the maximum tungsten weight flow rate was 0.13 g/sec (limited by the installed motor drive gear system). Addition of simulated fuel resulted in significant changes in the electrical and radiative characteristics of the plasma. In general, the radiation increased significantly. The peripheral wall of the chamber remained relatively free from fuel deposition, even after several minutes of steady-state fuel injection.
- (c) To permit injecting gaseous uranium hexafluoride as simulated fuel, a four-concentric-tube, water-cooled injection probe (incorporating an insulating air space between the fuel passage and the outer cooling water passages) was developed. This probe permits the simulated-fuel injection temperatures to be maintained high enough to prevent solidification of the fuel within the probe. A  $UF_6$  supply system incorporating an electrically heated, high-pressure canister was also developed.



- (d) RF plasma tests with simulated-fuel injection in the form of gaseous  $UF_6$  diluted by an argon carrier gas were conducted, also using the configuration having a fused silica pressure vessel. These tests were also conducted at radiant energy flux levels about equal to those expected in in-reactor tests and at chamber pressures up to 40 atm. The corresponding  $UF_6$  concentration within the argon carrier gas by partial pressure was 1 percent (the maximum attainable at the high pressure without further modifications to the  $UF_6$  supply system). The results were similar to those obtained with tungsten particle injection: significant changes were noted in the electrical and radiative characteristics of the plasma, and the peripheral wall remained relatively clean.
- (e) Analytical investigations were conducted of three methods for measuring the amount of simulated fuel contained in the rf plasma. These methods utilize a time-of-flight mass spectrometer, a radioactive tracer, and x-ray absorption. The mass spectrometer and x-ray absorption techniques appear to be the most promising and should be evaluated further in experiments.

4. Development and testing of models having peripheral walls constructed from large numbers of thin-walled fused silica tubes, as in the full-scale nuclear light bulb engine, was continued. An improved peripheral-wall argon-buffer-gas injection manifold was designed. In rf plasma tests, a model consisting of sixty 0.125-mm-wall tubes arranged axially around a 3.25-cm diameter was tested at pressures up to 35 atm and powers up to 193 kW. These pressure and power levels are about twice the levels achieved in prior tests. The maximum total heat flux (radiation and conduction) on the peripheral wall was approximately  $1.5 \text{ kW/cm}^2$ , compared with  $0.4 \text{ kW/cm}^2$  net radiant heat flux expected in in-reactor tests.

## INTRODUCTION

An experimental and theoretical investigation of different phases of gaseous nuclear rocket technology has been conducted by the United Aircraft Research Laboratories (UARL) under Contract SNPC-70 administered by the joint AEC-NASA Space Nuclear Systems Office. This investigation has been primarily directed toward evaluating the feasibility of the nuclear light bulb engine concept.

Details of this engine concept are discussed in Refs. 1 through 6. Figure 1 illustrates the principle of operation with sketches of the overall configuration and one nuclear light bulb reference engine unit cavity. The full-scale reference engine consists of a cluster of seven such cavities. In brief, the concept is based on the transfer of energy by thermal radiation from fissioning gaseous nuclear fuel (uranium) contained in a vortex, through an internally cooled transparent wall, to seeded hydrogen propellant flowing in an annulus surrounding the transparent wall. The hydrogen propellant is seeded with sub-micron tungsten particles to increase its opacity. A transparent buffer gas (neon) is injected near the inner surface of the transparent wall to form the vortex which contains and isolates the fuel from the wall. In addition, the neon buffer gas prevents diffusion of the nuclear fuel to the wall. High purity, internally gas-cooled, fused silica tubes (tube wall thicknesses in the range of 0.125 to 0.25 mm) appear suitable for the transparent wall. The neon and the entrained gaseous nuclear fuel and fission products exit through ports located on the centerline of the end wall of the cavity. Cold neon bypass gas is used to rapidly cool the hot exhaust gas mixture, thereby condensing the fuel. The condensed fuel is centrifugally separated from the neon and pumped back into the fuel containment region of the vortex. The neon is further cooled and pumped back into the cavity to drive the vortex.

Because of the high temperatures obtainable in the fuel region, engines of this type offer the ultimate potential of providing values of specific impulse greater than 3000 sec and engine thrust-to-weight ratios greater than unity. A summary of the performance characteristics is presented in Ref. 7. This closed-cycle fuel system concept is also unique because the physical interface between the nuclear fuel and the seeded hydrogen propellant (the internally cooled transparent wall) offers the possibility of providing perfect containment of the gaseous nuclear fuel and fission products.

Determination of the feasibility of a nuclear light bulb engine requires research in a number of technological areas including fluid dynamics, heat transfer, nuclear criticality, fuel handling, engine dynamics, and transparent-wall optical transmission properties, fabrication techniques and cooling techniques. Recently completed investigations related to several of these areas of nuclear light bulb engine technology are reported in Refs. 8 through 13.

Previous investigations (Refs. 14, 15 and 16) were directed at developing a non-nuclear rf plasma light source that could ultimately provide steady-state radiant energy fluxes similar to those expected in a full-scale reactor. The research program discussed in this report was directed at simulating the thermal environment and fuel region in small models of nuclear light bulb unit cells. Primary emphasis was placed on research necessary to develop test configurations and technology in preparation for tests in a driver reactor with high thermal neutron flux levels. The most promising candidate reactor is the Nuclear Furnace, designed and constructed at the Los Alamos Scientific Laboratory and tested at the Nuclear Reactor Development Station in Nevada.

Analytical studies have been conducted (Refs. 6 and 17) to define the characteristics and operating parameters of an in-reactor geometry (IRG) for the Nuclear Furnace. Figure 2 is a preliminary layout of the test cell. The vortex region consists of a cylindrical cavity, 6.6-cm i.d. by 17.8-cm long. As in the reference engine unit cavity (Fig. 1), the buffer gas is injected tangentially at the periphery of the cavity. Uranium fuel is injected at the centers of the symmetrical end walls. Additional details of this configuration can be found in Ref. 6.

The primary tasks of the research reported herein were:

- (1) To test an in-reactor geometry configured in general like the model for the Nuclear Furnace tests at chamber pressures up to 40 atm and radiant energy fluxes (from the surface of the plasma) equivalent to those expected during the in-reactor tests. Some of these tests were to incorporate a filament-wound pressure vessel.
- (2) To develop and demonstrate at 40 atm a particle feeder system capable of injecting micron-sized tungsten particles in a steady and controlled manner. This technique should be extendable to 500 atm operation.
- (3) To conduct uranium-hexafluoride-argon and tungsten-argon simulated-fuel injection tests at pressures up to 40 atm to obtain high fuel concentration with minimum fuel deposition on the transparent wall. Included was the development of an end wall optical technique for determining the "edge-of-plasma" location relative to the peripheral wall.
- (4) To analytically investigate and select methods for determining the location and concentration of simulated fuel within the test section (methods should be applicable to future 500-atm rf tests with an opaque pressure vessel surrounding the plasma).

- (5) To fabricate and test transparent wall models (configured similar to those that might be used in a reference nuclear light bulb engine) at high radiant energy fluxes and pressures exceeding 20 atm.

The experimental investigation was divided into three parts which are reported in separate sections: RADIANT ENERGY SOURCE RESEARCH, SIMULATED-FUEL INJECTION RESEARCH, and TRANSPARENT-WALL MODEL RESEARCH. The principal equipment common to the investigation is described in the next section.

In the research discussed in this report, the UARL 1.2-MW rf induction heater was used to create high-temperature plasmas in place of the fissioning uranium plasmas. Figure 3 shows sketches of the three basic test configurations employed. Table I summarizes the type of tests conducted with each configuration, including the figure numbers where pertinent data can be found. All configurations were basically cylindrical vortex chambers with concentric peripheral walls and copper end walls.

Figure 3(a) shows the basic configuration used in the majority of rf tests to simulate the thermal environment of the IRG test configuration, including injection of simulated fuel into the test section. The test section is configured similar to the proposed IRG and is approximately 7/8 as large. To establish the required radial-inflow vortex flow pattern, argon buffer gas is injected tangentially through vortex injectors located at the periphery of each end wall. Each end wall contains a thru-flow port (an annulus) on the centerline to remove the exhaust gas from the vortex chamber. The rf plasma discharge occurs in the region between the end walls with the major axis colinear with the thru-flow port axis. Simulated-fuel injection probes located on-axis at each end wall permit injecting seed material into the plasma region.

Figure 3(b) shows a similar configuration except that (1) the outer peripheral wall is an opaque fiberglass filament-wound tube and (2) no simulated-fuel injection probes are installed. The pressure vessel is of the type suitable for future high-pressure IRG simulation tests at 500 atm.

Figure 3(c) is a sketch of the configuration used for tests with the thin-walled, internally-cooled axial fused silica tube models (wall structure similar to that envisioned in the reference nuclear light bulb engine). This configuration was also tested without simulated fuel injection probes. The dimensions of this model were chosen primarily to provide high radiant energy flux levels at the wall.

## DESCRIPTION OF PRINCIPAL EQUIPMENT

The experiments described in this report were conducted using the UARL 1.2-MW rf induction heater. This section contains descriptions of the heater and the principal diagnostic equipment. Details of the individual test configurations used in each of the three test programs and other special equipment are discussed later under the appropriate program.

UARL 1.2-MW RF Induction HeaterBackground

The UARL 1.2-MW rf induction heater was constructed during 1966 and 1967 as part of the UARL Corporate-sponsored program on gaseous-core nuclear rocket technology. This heater was designed to ultimately be capable of depositing approximately 0.6 MW of rf power into a relatively small (approximately  $10 \text{ cm}^3$ ) plasma discharge. To date, the heater has deposited a maximum power of 0.22 MW into an approximately  $10 \text{ cm}^3$ , steady-state, argon plasma discharge (in other tests, up to 0.26 MW was deposited into a  $39 \text{ cm}^3$  plasma). Corporate-sponsored tests employing a salt-water load (uniform electrical conductivity) have continued to further develop and verify operation of all rf induction heater components. During these tests, up to 0.315 MW was deposited into the salt-water load (within a fiberglass filament-wound tube) at an overall system efficiency, defined as total rf power deposited in the load divided by the total dc power supplied to the heater, of about 45 percent.

Primary Heater Components and Test Tank

A detailed description of this equipment is given in Ref. 14. A block diagram showing the primary components of the heater is presented in Fig. 4. The operating frequency is selected by means of an L-C type variable frequency oscillator whose 0.5-W output is amplified to approximately 2 kW using a neon amplifier. The rf operating frequency is approximately 5.4 MHz. The 2-kW output is used to provide rf excitation for the basic rf induction heater stages which receive dc power from a common saturable-reactor-controlled power supply. The 2-kW excitation drives a 40-kW output amplifier which in turn drives a 80-kW buffer amplifier. This buffer amplifier is the actual driving stage for the final power amplifiers. All these stages contain controls for tuning the matching circuit at the final power amplifier input. This allows individual adjustment to be made to the various amplifier systems, thus aiding in increasing the overall system efficiency. The rf output power of up to 880 kW is supplied by two power amplifier tubes which drive a resonant tank circuit (resonator section) of unique design. Each power amplifier tube requires 600 kW of dc input power to produce the 440 kW of rf output power. The output of the two power amplifiers is resonated by a push-pull resonator. All

stages are operated class "C" to provide maximum efficiency. The saturable-reactor-controlled power supply for the 40-kW, 80-kW and final power amplifier stages is continuously variable in dc voltage from 2 kV to approximately 24 kV. This provides flexibility in selecting the power levels for the various experimental test requirements.

The power and voltage levels noted in Fig. 4 correspond to the maximum rated rf output and dc voltage for the various amplifier stages. The maximum total dc input power to the power amplifier employed in rf plasma tests during this program was approximately 600 kW.

A photograph of the resonator section is shown in Fig. 5. It is located within a 1.7-m-diam, cylindrical, aluminum test tank. The resonator section consists of two arrays of ten vacuum capacitors and two work coils for coupling of the rf power to the plasma discharge. Each array is connected with a single-turn work coil. Each work coil consists of five water-cooled, 0.475-cm-o.d. copper tubes which are silver soldered together to form a single structure. For most of the tests, a set of 8.6-cm-diam work coils were used. The coils are silver plated to reduce resistive heating due to the high coil current. The ends of the capacitors are water-cooled and rf chokes are installed in the cooling water lines. To suppress arc-over within the test tank, most tests were conducted with a 33 percent (by volume) mixture of sulfur hexafluoride in nitrogen at a test tank pressure of 2.5 atm.

The front of the test tank is a removable aluminum dome containing five 10-cm-diam windows which allow observation of the test section from different angles. An overhead trolley and winch system permits removal of the dome and allows rapid access to the test section for inspection after completion of a test series. Interchangeable test tank end flanges were used to accommodate the different gas and coolant lines associated with the three test configurations. A Micalox support fixture is attached to the base of the aluminum test tank and forward section of the resonator to hold the end walls of the test configurations concentric within the rf work coils. A pair of water-cooled tie-rods are installed horizontally within the test tank to minimize tank deflection under high axial pressure loads (see Fig. 5).

All components of the rf induction heater are water-cooled, requiring a total of approximately 50 gpm of cooling water. Measurements are made of all the cooling water and gas flow rates, associated temperature rises, and all electrical quantities necessary for performing a component and overall-system energy balance on the rf equipment. A detailed description of the control consoles used in the 1.2-MW rf induction heater tests is given in Ref. 15. Meters to monitor the voltage, current and power in various stages of the rf induction heater are used during the tests. Strip-chart recorders are also used to continuously monitor the plate voltage, plate current, and resonator voltage. The rf voltage applied to the resonator

section is measured with a capacitive-type voltage probe. A set of dual-channel strip-chart recorders (approximately 0.5-sec response time) and an automatic stepping-type temperature recorder are used to permit simultaneous monitoring of the critical measurements during the tests.

The rf input power to the plasma discharge is determined by the rf voltage supplied to the resonator section of the heater (Fig. 4) and the impedance of the plasma and resonator which, in turn, determines the current level. The impedance of the plasma is determined by its size and electrical conductivity.

#### Argon Gas and Cooling Water Flow Systems

Figure 6 is a schematic of the argon gas and high-pressure cooling water flow systems. Argon gas is supplied to the test chamber (i.e., to the vortex injectors) from an eleven-bottle supply having a total capacity of 2500 scf. This permits long run time capability, particularly during tests at high power with high argon weight flow rates. Flowmeters were used to measure the argon weight flow rate during most of the tests. For some tests at chamber pressures up to 43 atm, a sonic orifice flow-metering system was used (see Fig. 6). The exhaust gas was removed from both ends of the test chamber and routed through two flow control valves which were connected in parallel. One valve provided fine control of the chamber pressure in the higher pressure operating regime. The exhaust gases were ducted to the exhaust system and trap located on the laboratory roof.

To provide the necessary water cooling, two closed-loop, high-pressure cooling systems, each having a total storage capacity of approximately 75 gal, are used. Each system employs a positive displacement pump which supplies up to 20 gpm of cooling water at approximately 40 atm. A surge suppressor is used in each coolant loop to damp out the pressure pulsations, inherent in positive displacement type pumps, to less than one percent. Each coolant loop has a 70-gal capacity, open top, stainless-steel tank as a storage reservoir. Figure 6 shows additional details, including the locations of the heat exchangers and flow-metering equipment.

#### Plasma Starting System

The basic starting system consists of a high-frequency, high-voltage spark starter and an auxiliary dc arc starter. Reference 14 contains a schematic of the plasma starting system and a detailed description. Briefly, a pair of retractable tungsten tipped electrodes, located along the centerline of the test chamber, was used. A centrally located control panel permitted selection of one of three starting sequences which would provide the ionization level necessary for sustained coupling with the rf power: only the high-frequency mode, only the auxiliary dc arc mode, or a combination of the two. These starting systems permitted the rf plasma to be started at chamber pressures of about 1 atm (sometimes higher) in less than 10 msec.

In tests with simulated fuel injection, the fuel probes located within the thru-flow ducts precluded the use of auxiliary starting rods. For these tests, a vacuum start technique was used. With this technique, the rf plasma was ignited at approximately 10 torr using argon gas breakdown occurring at a resonator voltage of about 4 kV.

### Test Chambers

Figure 3 shows the three basic test chamber configurations for the rf plasma tests. A pair of water-cooled peripheral walls located concentrically within the rf work coils form the outer boundary of the test chamber. Tests with the filament-wound pressure vessel were conducted with the outer fused silica tube removed and replaced with the 2.9-mm-thick filament-wound tube (compare pressure vessels in Figs. 3(a) and 3(b)). Tests with simulated-fuel injection and transparent-wall models were conducted with inner and outer fused silica tubes having nominal inside diameters of 5.7 cm and 6.5 cm, respectively. In all configurations, the annulus between the tubes was used for water cooling.

A pair of symmetrical end walls are used to form the axial boundary of the test chamber. In the majority of tests, the distance between the end walls was 15.5 cm. This permitted a length-to-diameter ratio of 2.7 (identical to that of the proposed in-reactor test configuration) to be maintained. An exception to this was the 10.2-cm axial distance between the end walls used in the transparent-wall model tests. This dimension, with the 3.25-cm i.d. of the axial tube transparent-wall model, gives an  $L/D = 3.1$ . Additional details on each of the end-wall configurations used in the rf plasma tests will be described subsequently under the individual test program.

To reduce the intense radiation from the source incident on the surrounding components within the aluminum test tank (see Fig. 5) and to protect the fiberglass filament-wound pressure vessel and silicone rubber liner, known concentrations of nigrosine dye (organic, water-soluble dye with a color index of 50420) were added to the test chamber annular cooling water. Appendix B contains additional information on the dye and its properties.

### Diagnostic Equipment, Test Procedures, and Data Analysis Methods

#### Total Radiation Measurements

The power radiated from the plasma was measured using a specially constructed radiometer and chopper wheel assembly. A block diagram of the radiometer optical system and its associated transmission characteristics are shown in Fig. 7. A Reeder RLB-500 thermopile detector with a barium fluoride ( $BaF_2$ ) window was used



as the radiometer sensing element. The output was connected to an operational amplifier and displayed on a strip-chart recorder. Internal rf shielding and chokes were used to isolate the radiometer electronic system. A low speed synchronous motor drives a chopper wheel containing four apertures. Calibrated filters with the specific transmission characteristics shown in Fig. 7(b) were located in the apertures. For the tests reported herein, total radiation was determined in the following wavelength bands: 0.25 to 0.3, 0.3 to 0.72, 0.72 to 1.0, and 1.0 to 1.3 microns. The cutoff wavelengths were determined by the 50-percent transmission levels of the individual filters, BaF<sub>2</sub> window, or annular cooling water layer located between the fused silica tubes forming the test chamber (see Fig. 3). Transmission characteristics, obtained from Ref. 18, for a 2-mm-thick layer of pure water corresponding to the water-coolant annulus between the fused silica walls is also shown in Fig. 7(b).

The response of the thermopile with filters was calibrated using an Eppley Laboratory Calibrated Standard of Spectral Irradiance. Following calibration of the radiometer, a calibration constant for each wavelength range was determined. The total power radiated from the plasma in each wavelength range was then calibrated from the radiometer measurements by assuming isotropic radiation. Allowance was made for blockage due to the presence of the rf work coils.

To provide a continuous record of the total radiation in the wavelength band of 0.25 to 1.3 microns for selected tests, the chopper wheel was held stationary at the open aperture location.

As discussed previously, nigrosine dye was used to reduce the radiation from the rf plasma to the surroundings. Nigrosine was selected after tests were conducted to determine the type of dye or pigment with the most desirable characteristics (see Ref. 14). In addition, tests were conducted to verify that the absorption characteristics of the coolant with nigrosine added were not influenced by radiation from the plasma source or by the bulk temperature of the coolant for the range of test conditions employed. Results of other tests showed the water-dye coolant in the concentrations used absorbed negligible amounts of rf energy, thereby introducing no errors into the energy balance calculations. For the tests reported, nigrosine dye in concentrations varying from 100 to 10,000 ppm (on a weight basis) were used. Additional details on the physical and optical properties of nigrosine dye, including comments on a dye deterioration effect noted only in the simulated-fuel injection portion of the test program, are included in Appendix B.

#### Photographic Equipment and Viewing System for Recording and Observing Plasma Behavior

Photographs and high-speed movies taken from several of the view ports permitted an estimation to be made of the plasma size, shape, and stability for selected tests. Continuous observation of the plasma was accomplished using a projection screen

system. A 45.7-cm focal length convex lens and neutral density filter system was used to project an image of the plasma discharge onto an overhead viewing screen. Horizontal and vertical grid lines placed on the screen also permitted estimates to be made of the changes in the discharge size and shape as the test parameters were changed.

#### Optical Scanning System for Determination of Plasma Diameter

The optical scanning system used to obtain the plasma diameter is described in detail in Ref. 14. Figure 8(a) is a sketch of the basic system which includes a photomultiplier (RCA 6655), collimating tube with two apertures, fiber optic tube attached to a traversing mechanism and a rotatable filter wheel containing neutral density filters. The apertures were sized and located such that a 1-mm-diam spot was viewed. The output from the phototube (proportional to light intensity) enters a signal conditioner and is then fed to a strip-chart recorder. As shown in Fig. 8(a), the fiber optic tube and traversing mechanism were located on the top view port of the dome of the test tank. This permitted scans of the plasma diameter at the axial midplane location. A 1.0-percent cutoff criterion (i.e., local intensity equal to 1.0 percent of the peak intensity; see Ref. 14) was used for establishing the plasma diameter from the scanner trace; agreement within about 5 percent of the diameter determined from photographs using neutral density filters was obtained. See Ref. 14 for additional details on the system and cutoff criterion, and for comparison with diameters determined from photographs using neutral density filters.

#### Spectral Emission Measurements

A sketch of the optical system used to obtain spectral measurements is shown in Fig. 8(b). Details of the system, calibration and data processing procedures are discussed in Ref. 14. The basic system consisted of a Jarrell-Ash 82-410 0.25-meter Ebert monochromator and EMI 9558 photomultiplier detector mounted on a traversing table to allow chordal scans of the plasma. The monochromator had 25-micron-wide entrance and exit slits. A calibrated 34.2-cm focal length lens was positioned between the rf plasma and the entrance slit of the monochromator such that the image size was equal to the spot size. Wavelength scans between 3700 Å and 6500 Å were made at a scanning rate of 1000 Å/min. In selected tests, scans were made of the continuum at 4320 Å and of several spectral lines. In these tests, the monochromator was diametrically traversed through the plasma image at the axial midplane as shown in Fig. 8(b). The continuum at 4320 Å was selected since it represents a well-documented continuum region of an argon plasma (Refs. 19 and 20) and eliminates the possible influence of line broadening and self-absorption effects, particularly in the higher pressure/power operating regime. Several calibrated neutral density filters were located in front of the monochromator entrance slit to reduce the intensity of the incident light corresponding to different test conditions. The photomultiplier output went into a signal processor and was then displayed on a strip-chart recorder modified to operate at a high feed rate (up to 76.2 cm/min).

### Optical System for Determining "Edge-of-Plasma" Location

Figure 9 is a sketch of the rf plasma source, including the optical system used for determining the "edge-of-plasma" location relative to the inner peripheral wall. The basic system includes a series of optical view ports (located in one end-wall assembly at several radial locations), fiber optic tubes, a photomultiplier assembly, a signal processor, and a strip-chart recorder. The optical view ports were 0.58-mm-diam stainless steel tubes and were located at radius ratios (i.e., ratio of the radial location of the port center to the radius of the test chamber) of 0.36, 0.40, 0.45, 0.50, 0.60, and 0.75, respectively. During final fabrication of the end-wall assembly, difficulties were encountered in the installation of these view ports. In particular, electron beam welding of the small stainless steel tubes to the massive copper end wall proved to be successful in only two of the six view ports. (radius ratio of 0.4 and 0.6). It was therefore necessary to seal off (using electron-beam puddling techniques) the four leaking view ports. The measurements obtained using this end-wall optical view port technique were compared with those obtained using the optical scanner system and the photographs to verify the feasibility of this technique.

### Determination of Energy Balance

The total power deposited into the plasma was obtained from an overall energy balance as shown in Fig. 9. The total power deposited into the plasma,  $Q_T$ , was obtained by adding together the power lost by radiation,  $Q_R$ ; the power deposited into the annular coolant, (water-dye mixture)  $Q_W$ ; the power deposited into the end-wall assemblies,  $Q_E$ ; the power convected out the thru-flow exhaust ducts and deposited into the heat exchangers,  $Q_L$ ; and the power deposited into the simulated-fuel injection probes,  $Q_P$  (applicable in tests when these probes were used).

The power radiated from the rf plasma which passed through the internally cooled transparent peripheral wall and water-dye coolant was measured using the radiometer system described previously. By monitoring the flow rate and associated temperature rise of the coolant flowing in the annulus between the inner and outer fused silica tubes, the total power deposited in the peripheral wall was calculated. In the majority of tests, dye was used in the annular coolant loop; thus, it was necessary to replace the standard flowmeters (Rotameters) with calibrated magnetic-type flowmeters. The associated inlet and exit coolant temperatures were monitored with copper-constantan thermocouples located as close to the test region as possible. Similarly, by monitoring the flow rate and associated temperature rise of the coolant flowing in each end wall, simulated-fuel injection probes, and exhaust gas heat exchangers, the total power deposited in each of these components was determined. Depending on the test configuration, two types of water-cooled exhaust gas heat exchangers located in each of the two separate exhaust lines permitted determination of the power convected out the thru-flow exhaust ducts. In all tests reported, sufficient time was allowed for all temperatures to reach a steady-state level, thus permitting an accurate calorimetric determination of the overall power breakdown.

### Determination of Source Radiation Characteristics

To permit calculation of the radiant energy flux at the surface of the plasma, it is necessary to determine the plasma size and shape and the total heat radiated through the inner fused silica tube of the test chamber. The optical scanning device, described previously, permitted a determination of the plasma diameter,  $d$ , at the axial midplane. The end-wall optical view port technique was also used at several selected test conditions to verify the plasma diameter determined using the optical scanning device. Photographic techniques using different filter densities, camera shutter speeds, and film exposure times, allowed an estimate to be made of the overall shape of the plasma. The photographs were taken through the view ports in the aluminum test tank.

For the data reported herein, the total heat transferred through the inner fused silica tube,  $Q_{R,T}$ , is defined as the sum of the radiated power as measured by the radiometer system and the power deposited in the peripheral wall annular coolant minus the power conducted through the inner peripheral wall. Since the amount of heat conducted through the inner peripheral wall was not measured directly, estimates were made by calculating the maximum heat flux which could be conducted through the inner fused silica tube for the range of test conditions and test configurations reported herein. The estimates were based on experimental test experience and careful examination of the inner fused silica peripheral wall under polarized light both before and after the rf plasma tests. For the tests reported herein (except in several simulated-fuel injection tests), no significant traces of residual thermal stress were found in the peripheral walls after steady-state exposure to the high radiant energy flux conditions. A value of 4 percent of the power deposited in the peripheral wall annular coolant was typical for the maximum possible conducted power at the high power test conditions. Refer to Ref. 15 for additional details on the assumptions used and the calculation procedure.

The values of total radiated heat emitted from the plasma quoted herein are conservative by amounts which depend upon the operating conditions. This is because the radiation contribution to the power deposited in the copper end walls has not been separately accounted for. Initially, the water-cooled copper end walls were highly reflective, but after several tests, their surface reflectivities decreased. Therefore, a significant fraction of the total power deposited into the end walls comes from the radiation contribution.

## RADIANT ENERGY SOURCE RESEARCH

## RF Plasma Tests with 7/8-Scale IRG Fused Silica Pressure Vessel Configuration

Background

Earlier tests using the 1.2-MW rf induction heater concentrated on investigating vortex fluid dynamic techniques for confining rf plasma discharges and on determining the effects of chamber pressure, total discharge power, vortex gas flow rate, and rf operating frequency on the plasma discharge radiation characteristics and behavior (Refs. 14 and 15). These earlier experiments were aimed at developing an intense radiant energy source capable of producing radiant energy fluxes approaching those expected in a full-scale nuclear light bulb engine. The tests demonstrated that it is possible to deposit large amounts of steady-state rf power into a relatively small plasma discharge. In addition, an operating envelope was established which permitted successful operation of the confined plasma discharge at thermal conditions approaching those required for full-scale engine simulation. The maximum steady-state radiant energy flux achieved was  $7.6 \text{ kW/cm}^2$  (exceeding that of the sun), which corresponds to an equivalent black-body radiating temperature of  $6040^\circ\text{K}$ . The nuclear light bulb reference engine operates at  $8333^\circ\text{K}$ .

Part of the continued research effort permitted establishing design, operating characteristics, and test conditions of a Nuclear Furnace test configuration (Ref. 17). During the FY 1971 program, a 2/3-scale version of an early in-reactor test unit cell was developed and tested at chamber pressures up to 22.5 atm (Ref. 16).

The radiant energy source research program reported herein has emphasized tests both at high power and high pressure levels using an approximately full-scale version of a possible in-reactor test configuration.

Objective

The primary goal of this portion of the research effort was to develop and test an in-reactor geometry configured in general like the model for the Nuclear Furnace tests at chamber pressures up to 40 atm and radiant energy fluxes (from the surface of the plasma), greater than, or equal to, those expected during the in-reactor tests.

Basic Test Configuration

Figure 10 shows a cross-section of the basic test configuration used in these tests. Also shown for comparison is the unit cell for the Nuclear Furnace in-reactor tests. The chamber inner diameter and length are 7/8 of those of the

nominal in-reactor test cell designed for the Nuclear Furnace. The distance between the end walls for the nominal in-reactor unit cell is 17.78 cm, compared with 15.5 cm in the rf test configuration. The length-to-diameter ratio for both configurations is 2.7.

To provide a design for safe operation at chamber pressures slightly exceeding 40 atm and plasma discharge power levels of approximately 200 kW, calculations were performed to estimate the stress limits (both hoop and thermal) in the transparent fused silica tubes used in the test configuration. The results indicated that by using a concentric set of fused silica tubes having the dimensions shown in Fig. 10(b), the desired test conditions could be achieved with a reasonable margin of safety.

Use of a fused silica tube as the pressure vessel instead of a filament-wound tube offers several advantages. By permitting continuous visual observations (side-on), much information can be obtained relative to plasma starting procedures; discharge size, shape and stability; and, condition of the inner transparent wall and end walls. Measurements leading to estimation of the equivalent black-body radiating temperature and spectral emission characteristics can also be more readily made.

Based on information received from various fused silica tube fabricators and suppliers, it was decided to fabricate the 9-mm-wall-thickness, 65-mm-i.d. tube using a cast ingot technique. Alternate techniques, such as drawing, double lamination, or direct bore-out are also possible, but the wall thickness tolerances obtainable ( $\pm 30$  percent) and other associated fabrication difficulties and development costs made them unacceptable. All tubes fabricated by the cast ingot technique conformed to the dimensions shown in Fig. 10(b). The ends of the i.d. were flat ground to provide an adequate O-ring seal. Following the grinding operation, the entire tube was polished, annealed and the ends flame polished. Inspection of the tubes under polarized light indicated them to be free of any residual thermal stresses.

Each copper end wall contains a 1.14-cm-diam thru-flow duct on the centerline used to remove the exhaust gases from the vortex chamber. The surfaces of both end walls are highly polished to increase their reflectivity. To establish the desired radial-inflow vortex flow pattern, eight stainless-steel vortex injectors are equally spaced around the periphery of each end wall; these injectors are flush with the end-wall face. The injectors are positioned such that the argon buffer gas will enter the vortex chamber in a circumferential direction only. The inner diameter of the vortex injectors is 0.234 cm. These were sized to permit relatively low injection velocities, thus minimizing the radial acceleration present in the fuel region. In this way, "g" levels comparable with those expected in the Nuclear Furnace (approximately 20 to 50 g) were realized.

Figure 10(b) shows a symmetric pair of simulated-fuel injection probes used in these tests. These probes were located concentrically within the thru-flow duct and (based on exploratory tests) protruded 1.9 cm into the test chamber from the face of each end wall. This distance can be varied should another axial location of the probe tip provide better fuel injection in future tests.

### Test Procedures

Figure 11 is a photograph of the test configuration installed in the 1.2-MW rf induction heater. Prior to rf plasma tests, the entire configuration was statically pressure checked to 42 atm.

Earlier tests of a similar geometry with 7.8-cm-i.d. work coils permitted a direct gas breakdown starting technique to be used. Due to the combined effects of an increased diameter rf work coils (increased to 8.6 cm due to the 9-mm-wall thickness outer fused silica tube), the associated unloaded resonant frequency shift, and small changes in the configuration overall size, the plasma could not be initiated at 1 atm using the usual gas breakdown technique (i.e., without the auxiliary starter system). The simulated-fuel injection probes located within the thru-flow ducts precluded using the auxiliary starter systems. Therefore, an alternate low pressure (< 10 torr) vacuum start technique was employed. This technique proved to be reliable and was employed in all tests with this configuration.

### Discussion of Test Results

Figure 12 illustrates the range of discharge diameters and total discharge powers obtained in the tests. The table at the top of the figure indicates the range of operating conditions. The diameters shown were determined from measurements made at the axial midplane location using the optical scanning system. For reference, the upper two horizontal dashed lines show the inside diameter of the rf work coils and the inside diameter of the inner fused silica tube of the test chamber.

These tests verified that the discharge could be maintained in a stable geometry over the range of test conditions shown with diameters of approximately 2 cm. The envelope of 19 data points shown illustrates the ability to increase the chamber pressure from 22 to 41 atm while still maintaining the discharge diameter and total discharge power approximately constant.

The highest pressure achieved in prior tests (FY 1971) with a fused silica pressure vessel configuration was 22.5 atm. The highest pressure/highest power test condition achieved in FY 1972 is also shown in Fig. 12. At this condition, 180 kW of power was deposited steady-state into the plasma while operating at a chamber pressure of 42 atm. Additional details of the power breakdown for this

highest-pressure/highest-power operating condition, which also was the test condition for maximum radiation through the inner transparent wall, are shown in Fig. 13 and in Table II. The corresponding key test conditions are shown at the top of the figure. The power breakdown for each component is shown below the sketch.

The discharge diameter at the axial midplane in the test shown in Fig. 13 was 1.65 cm. The discharge shape is shown by the shaded area in Fig. 13. Photographs taken through the various view ports indicated the discharge was cylindrical over the central portion with approximately conical end regions. The plasma-discharge radius to peripheral-wall radius ratio,  $r_6/r_1$ , was 0.3. Based on estimates made from the photographs, the discharge surface area was  $71.5 \text{ cm}^2$ . The fraction of the discharge power radiated through the inner peripheral wall was 0.75. Thus, the plasma was operating in a highly radiation-dominated mode. For this test condition, the radiant energy flux achieved at the surface of the discharge was  $1.9 \text{ kW/cm}^2$ , corresponding to an equivalent black-body radiating temperature,  $T^*$ , of  $4320^\circ\text{K}$  (based on total heat flux and equivalent surface area). For reference, the total radiated heat flux expected at the edge of fuel in the reference in-reactor unit cell is  $0.67 \text{ kW/cm}^2$ ; the corresponding  $T^*$  is  $3333^\circ\text{K}$ .

Figure 14 presents photographs of the test configuration and the plasma operating at 36 atm (no photographs were taken at 42 atm). Figure 14(a) shows the 7/8-scale IRG configuration viewed through the right view port of the test tank with no plasma present. For the test shown in Fig. 14(b), the equivalent black-body radiating temperature was  $3830^\circ\text{K}$ . A simulated-fuel injection probe protruding from the right end-wall assembly is just visible in both photographs. The approximately cylindrical shape is evident in the photograph.

Figure 15 illustrates the variation of power radiated through the inner peripheral wall with total discharge power for the range of test conditions shown. The dashed lines are lines of constant radiation efficiency (i.e., the fraction of the total discharge power that is radiated through the inner peripheral wall). The solid circle symbol corresponds to the approximate total power level of the reference in-reactor test and the radiated power incident on the reflecting wall. As shown by the least-squares curve, the trend to 42 atm has been relatively well established in the tests reported. The 42-atm test condition was a limit based on the gas and cooling water systems available for the tests. Also, further hydrostatic tests would have to be conducted to determine whether the fused silica pressure vessel could be safely taken to higher pressures.

Figure 16 shows the variation of radiant energy flux with total discharge power obtained in the tests. The corresponding range of test conditions are shown in the table at the top of the figure. The discharge surface area was computed based on the diameter measured at the axial midplane. The radiant energy flux,  $Q_{R,T}/A_S$ , is based on the power radiated through the inner peripheral wall of the test chamber.



The range of flux levels expected in Nuclear Furnace in-reactor tests (corresponding to 3230°K to 3510°K) is shown by the horizontal shaded area; the reference in-reactor performance level is 3333°K. The results indicate total discharge power levels of 80 to 100 kW were sufficient, for the pressures and plasma diameters of these tests, to achieve the flux levels expected in a Nuclear Furnace in-reactor test. The ratio of discharge (as measured at the axial midplane of the test chamber) to test chamber inner diameter ranged from about .3 to 0.4 for the data shown in Fig. 16. For the reference Nuclear Furnace in-reactor test condition the ratio of the uranium plasma diameter to test chamber inner diameter is 0.6. Thus, larger discharge diameter ratios are desirable to simulate the uranium plasma. Increasing power and injection of simulated fuel favors increases in diameter ratio. For reference, the equivalent black-body radiating temperature,  $T^*$ , is shown at the right ordinate in Fig. 16. Note that the single data point at 42 atm corresponds to a discharge power of 180 kW and a relatively high argon weight flow rate (8.6 g/sec). This resulted in a high flux level, primarily due to the smaller discharge diameter obtained.

Figure 17 illustrates the effect of chamber pressure on the fraction of total discharge power radiated through the inner peripheral wall. The trend to about 20 atm has been relatively well established by previous tests (Ref. 16). A least-squares curve fit applied to all the data points indicates a leveling off of the radiation efficiency at approximately 75 percent as higher pressures, up to 42 atm, are reached. It should be noted that addition of simulated fuel will affect several parameters (e.g., power in the plasma, plasma impedance, diameter, etc.) in a manner which may have appreciable influence on the radiation efficiency trend shown in Fig. 17.

Typical results for the radial distributions of temperature obtained from the argon rf plasma operating in the 7/8-scale IRG configuration are shown in Fig. 18. The spectral emission measurements were made using the optical system shown in Fig. 8(b) (discussed previously in the section entitled DESCRIPTION OF PRINCIPAL EQUIPMENT). Measurements were made at the axial midplane. The monochromator system was aligned so that it scanned across chords of the discharge at the axial midplane location. The absolute value of the continuum radiation was measured at a wavelength of 4320 Å. By assuming thermodynamic equilibrium, the radial temperature distribution through the plasma was determined from the continuum radiation measurements using the method described in Ref. 21 for relating the continuum intensity to the temperature. A machine program employing the Abel inversion method was used to convert the measured chordal intensities to radial intensities. A complete description of the data reduction techniques is presented in an appendix of Ref. 22.

The test conditions for the temperature distribution measurements are shown in the table at the top of Fig. 18. Three typical radial distributions of temperature are shown. The corresponding plasma radius at the axial midplane, determined

using the fiber optic scanning system, is also shown in the lower right-hand corner of Fig. 18. As also noted in earlier tests (Refs. 15 and 16), the temperature profiles exhibit a distinct off-axis peak. For the three cases shown, the peak temperatures ranged from about 10,900° K to 11,500° K; they occurred at radius ratios (radius corresponding to peak temperature divided by measured radius of plasma at axial midplane) of about 0.5. The three cases shown were selected since they represented a relatively wide range of total discharge powers and chamber pressures. Note that Case I corresponds to the highest-pressure/highest-power operating condition achieved with the 7/8-scale IRG configuration using the fused-silica pressure vessel. To illustrate the effects of chamber pressure and total discharge power on the temperature profiles, Case III represents decreases in pressure and power by factors of 4 and 3, respectively, relative to Case I.

It is worthwhile to note from the radial distributions of temperature shown, which occur over a relatively wide range of discharge powers and pressures, that only small differences in profile shape and peak temperature occur (only approximately a 6-percent difference in temperature). The same is basically true for the centerline temperature change between the three cases illustrated. The relatively small changes in radial distribution of temperature over the range of cases shown make it worthwhile to compare these results with results obtained from theoretical considerations. To aid in this comparison, various temperature ranges are shown on the ordinate of Fig. 18. The uppermost set is the range of the intensity-averaged temperatures for the three cases shown. These were calculated from the integrated average intensity using the relationships between intensity, temperature, and radius. The middle set represents the temperature range calculated from the variation of radiated power per unit volume with pressure (see Fig. 19). The bottom set corresponds to the average temperature range (for all flow in the chamber) calculated from exhaust gas enthalpy measurements.

Calculated variation of radiated power per unit volume with temperature, with pressure as a parameter, is shown in Fig. 19. Also shown are three experimental points for the same cases shown in Fig. 18. The calculations (including both line and continuum contributions) were made over the wavelength range from 0.3 to 1.0 microns using the procedure of Ref. 23. The three data points shown were located using the test chamber pressure and the measured radiation and plasma volume determined from photographs. These results appear to indicate that, for the 7/8-scale IRG configuration and over the range of test conditions corresponding to Cases I through III, changes in the total discharge power and chamber pressure do not significantly alter the temperature of the rf plasma.

## RF Plasma Tests with 7/8-Scale IRG Filament-Wound Pressure Vessel Configuration

### Background

To extend the operating pressure range of the rf plasma in-reactor geometry test configuration to 500 atm (the chamber pressure of the reference Nuclear Furnace IRG), research efforts have been devoted to developing the technology required to operate an rf plasma within a filament-wound pressure vessel. At 500 atm, thick-walled fused silica tubes (as used in the tests described above) are not practical as pressure vessels. The pressure vessel also must carry both the axial and radial loads. In addition, physical constraints (larger rf coils and end-wall compression rods) would make simulation of full-size IRG models difficult. Fiberglass filament-wound tubes can be utilized at these pressures, provided they are compatible with the rf and radiant energy source environment. Earlier research (Ref. 15) included hydrostatic tests of small fiberglass filament-wound tubes (fabricated at UARL) to pressures exceeding 500 atm. In exploratory hot-flow tests, a filament-wound tube was tested as the pressure vessel surrounding an rf plasma at low power ( $\approx 12$  kW) and low pressure ( $\approx 1$  atm). Other tests demonstrated the feasibility of fabricating filament-wound pressure vessels in a size suitable for IRG simulation testing; these pressure vessels were operated with flowing argon and coolant water at pressures exceeding 500 atm with no rf plasma present (Ref. 11). In addition, compatibility with an rf plasma environment at total discharge powers up to 50 kW (Ref. 16) was also demonstrated. Reference 16 provides a detailed description of the method of fabrication, including details of the epoxy resins used and their associated properties.

### Objective

The goal of the present program was to develop and test a fiberglass filament-wound pressure vessel capable of operating reliably in an approximately full-size IRG test configuration with an rf plasma present. The pressure vessel must permit steady-state operation with chamber pressures up to 40 atm and with the radiant energy flux emitted from the plasma greater than, or equal to, that of the reference in-reactor configuration.

### Basic Test Configuration

Figure 20 is a sketch of the 7/8-scale IRG filament-wound pressure vessel test configuration. This geometry is similar to that shown previously in Fig. 10(b). A 6.6-cm-i.d. x 7.2-cm-o.d., filament-wound fiberglass tube and silicone rubber sealing liner replaced the outer 9-mm-thick fused silica pressure vessel used in the tests reported in the previous section. The 0.29-cm wall thickness of the

filament-wound tube provides the necessary strength requirements to permit safe operation at 40 atm with plasma power levels of about 200 kW. Two types of resins (63 and 2256) were used in making the pressure vessels used in the tests (see Table V of Ref. 16 for properties of these resins).

As in the fused silica tube configuration, the end walls were spaced 15.5 cm apart and were located concentrically within the fused silica tube, filament-wound pressure vessel, and rf work coils. Both copper end walls were polished to increase their reflectivity. A thru-flow duct of 0.79-cm diam was used to convect out the exhaust gases from the test chamber. No simulated-fuel injection probes were used in this model. Eight stainless steel vortex injectors were located equally spaced around the periphery of each end wall. In the hot-flow tests, two size injectors were used. One set had an i.d. of 1.07 mm and the other set an i.d. of 2.34 mm. The injector tips were flush with the end-wall surface and were positioned such that the argon entered the test chamber in the circumferential direction only. A static pressure tap for measurement of the chamber pressure (see Fig. 20) was located in one end wall at a radius ratio of 0.75.

Stainless-steel retainer flanges (four individual 90° segments) provide the required structural integrity to withstand the shear forces (see Fig. 20). The axial and radial loads are carried by the pressure vessel. The axial pressure load is transmitted to the filament-wound pressure vessel from the end walls by shear forces in the retainer flanges. Water-cooled copper rf shields (see Fig. 20) surrounded the retainer flanges to further minimize the rf heating effects. The retainer flanges were silver plated (3-mil thickness).

Figure 21 is a photograph of the disassembled configuration. The silicone rubber sealing liner prevents seepage of the annular coolant through the wall of the filament-wound tube. The liner contains 5-percent titanium dioxide which was added to increase its opacity and provide additional thermal protection for the filament-wound tube. A ridge is integrally molded into each end of the liner (see Figs. 20 and 21). This ridge fits into a groove in the sealing ring to prevent leakage at the ends of the tube assembly. Strong concentrations of nigrosine dye in the water coolant (greater than  $10^4$  ppm) were used in the tests to prevent excessive thermal radiation from reaching the liner and filament-wound tube. The small amount of radiation which passes through the water-dye coolant (less than 1 percent) is absorbed by the liner which is convectively cooled by the coolant. The operating limit of the tube and liner, based on the manufacturer's recommended service temperature for the epoxy binder and silicone rubber, is approximately 425°K.

Figure 22 is a photograph of the 7/8-scale IRG filament-wound pressure vessel configuration installed in the rf induction heater with the front dome of the test tank removed. The temperature sensitive paint used to monitor the outside surface

temperature of the pressure vessel and the water-cooled rf shield surrounding the stainless-steel retainer flanges is visible in the photograph. A Micallex cradle used to support the test chamber is shown attached to the lower resonator section. The relatively short end-wall assemblies can be quickly removed from the test tank by disconnecting the quick-disconnect gas and cooling water connections between the end walls and test tank flanges shown in Fig. 22.

### Test Procedures

Prior to any rf plasma tests, the entire configuration was hydrostatically pressure checked in a series of cyclic tests to 50 atm. The internal pressure on the liner and filament-wound pressure vessel was increased to 50 atm (10-atm factor of safety) maintained for 3 min, and then reduced to 1 atm. This procedure was repeated 3 times. Separate tests conducted using the 1.2-MW rf power supply, but with no plasma present, verified that no excessive rf heating of the filament-wound tube, stainless-steel retainer flanges, or other individual components which made up the test configuration occurred. These tests also verified that the clearances between the retainer flanges and main rf transmission lines were adequate to prevent arc-over.

The auxiliary dc arc starting system (combination high frequency and arc mode) permitted moderately high-power-level rf plasma discharges to be reliably started at pressures of about one atm. Prior to starting the rf plasma, the rf drive system (see Fig. 2) was pretuned for the proper resonant frequency. Following initiation of the discharge, the starter electrode assemblies were removed from the end-wall thru-flow ducts and the plugs were reinserted. The rf drive system was then retuned to compensate for the resonant frequency change due to the presence of the plasma within the rf work coils. Following this, the argon weight flow rate was increased and the chamber pressure was increased by throttling the exhaust valves (see Fig. 6). After a routine calibration check was made of the recording equipment and exit temperatures for each of the critical components, the rf input power, argon weight flow rate and chamber pressure were increased to the level desired for a particular test condition.

### Discussion of Test Results

Figure 23 is a sketch of the power breakdown for the highest power operating point. For this test, a total of 203 kW was deposited steady-state into the plasma discharge at 40 atm. Other test conditions are shown at the top of Fig. 23. As indicated previously, the highest power achieved in prior high-pressure tests (FY 1972) with a filament-wound tube pressure vessel was about 50 kW (at a chamber pressure of 22.5 atm). The maximum power corresponding to an earlier 40-atm test was 35 kW.

As shown in Fig. 23, 151 kW of the total power deposited into the discharge ( $\approx 75$  percent) was absorbed by the water-dye coolant at the 40-atm test condition. Both end-wall assemblies absorbed a total of 26 kW, or about 13 percent of the total power deposited into the discharge. Included in this was the small contribution (less than 5 percent) due to the rf heating effect in the end-wall and shield assembly. The remaining power, 26 kW or 13 percent, was deposited into the inter-stage and thru-flow exhaust gas heat exchangers.

In all the high-power/high-pressure tests, dye concentrations greater than  $10^4$  ppm were used. The opaque nature of the filament-wound vessel and liner, combined with the heavy dye concentrations, resulted in no measurable radiation emitted from the test chamber. The complete loss of visibility precluded any direct measurements of the plasma diameter; therefore, only estimates could be made. However, based on similar operating conditions using the fused-silica pressure vessel configuration, the radiant energy fluxes achieved were estimated to equal or exceed those of the reference in-reactor geometry.

Figure 24 summarizes the results of the test series conducted with the filament-wound pressure vessel over the range of chamber pressures from 5 to 43 atm. Shown is the variation of power deposited into the annular coolant with total discharge power. These tests were conducted using the basic test configuration shown in Fig. 20. The dashed lines shown correspond to lines of constant fraction of total discharge power deposited into the annular coolant. Also shown for reference by the solid circle is the approximate reference in-reactor test condition. A least-squares curve fit is shown through all the data. In some of the initial tests, a different resin material, rf work coil diameter and test chamber length were employed. These are illustrated by the open circle symbols (see table at the top of Fig. 24). (The increase in rf work coil diameter from 7.8 to 8.6 cm was necessitated by the 9-mm wall thickness fused silica tube tests discussed previously.) To maintain as much similarity as possible between the fused-silica tube tests and those using the filament-wound pressure vessel, the 8.6-cm-diam rf work coils were employed in all subsequent tests (shown as square and triangular symbols in Fig. 24).

In FY 1971 tests using a filament-wound pressure vessel, no attempt was made to maximize the plasma discharge power as the pressure was increased above 20 atm, i.e., the saturable reactor power control was held constant, as was the argon weight flow rate. As a result, the total discharge power decreased as the chamber pressure was increased above 20 atm. At 40 atm, the total discharge power decreased by about 30 percent over what it had been at 20 atm (from 50 kW to 35 kW). In the tests reported herein, both the saturable reactor power control and the argon weight flow rate were increased at pressures above 20 atm. This resulted in more power being deposited into the plasma as increasingly higher chamber pressures were reached.

Figure 25 shows the effect of chamber pressure on the fraction of total discharge power deposited in the annular coolant. The range of test conditions is shown in the table at the top of Fig. 25. A least-squares fit was used for establishing the curve through the data. The maximum pressure of 43 atm was limited by the gas and cooling water systems --- primarily the case and glands of the positive displacement pump. Comparison of this data with the data obtained over a similar power and pressure range using the fused-silica tube pressure vessel (Fig. 17) indicates the similarity of the results. It is apparent that a leveling off of the fraction of total power transmitted through the inner peripheral wall occurs in both cases; however, this is more pronounced in the test results using the filament-wound pressure vessel. Reasonably good agreement is seen between the two least-squared data curves over the entire pressure range.

To permit a direct comparison between the operating envelopes of the tests using the fused-silica pressure vessel and the filament-wound pressure vessel, Fig. 26 shows the operating range of total discharge powers and chamber pressures for the two configurations. Also shown is the approximate power level of the reference in-reactor test. The overlapping areas indicate it is possible to operate both test configurations over a relatively wide range of power and pressure operating conditions. The radiant energy flux corresponding to these high-pressure tests exceeds that required for the reference Nuclear Furnace IRG test configuration.

These test results demonstrate that it is feasible to employ a filament-wound tube as a pressure vessel in an approximately full-scale IRG test configuration at test chamber pressures to 43 atm and total discharge power levels exceeding 200 kW. No rf system limitations were evident to indicate it would not be possible to operate an argon rf plasma at chamber pressures up to 500 atm --- the chamber pressure corresponding to the reference engine and early in-reactor unit cell test.

## SIMULATED-FUEL INJECTION RESEARCH

## Particle Feeder System

Background

Operation of the nuclear light bulb engine and in-reactor test unit cell requires that gaseous or particulate uranium fuel be continuously and uniformly injected into the fuel region of the vortex at high pressures (500 atm). Operation is also dependent upon achieving ratios of fuel partial pressure to chamber total pressure of about 0.3 with minimum diffusion of the fuel to the transparent wall.

Injection of simulated fuel in particulate form offers advantages over gaseous fuel injection, particularly from the standpoint of preventing condensation of simulated fuel in the fuel injection duct at high pressures. Preliminary particulate simulated-fuel injection tests were conducted in FY 1971 (Ref. 16) using a feeder system employing a worm-screw feed technique. Argon served as the carrier gas and tungsten particles (1-to-10- $\mu$  nominal diameter) were used as the particulate simulated fuel. The feeder system consisted of a powder canister mounted on an electromagnetic vibrator, a variable-speed worm screw to meter powder out of the canister, and a carburetor assembly to disperse the powder within the argon carrier gas. The powder canister was limited to a working pressure of 3 atm. Results of cold-flow tests indicated random pulsations occurred in the seed feed system. These pulsations were also evident in the rf hot-flow tests and manifested themselves as perturbations in the electrical parameters of the rf plasma. Several modifications were made to the feeder system in an attempt to improve its performance. Further tests still resulted in unsteady and pulsating flows over wide ranges of vibrator setting, screw feed rotational speed, argon carrier gas flow rate, and canister chamber pressure. The primary cause of the unsteady operation observed is believed to be intermittent packing of the tungsten seed material in the worm screw (apparently an inherent characteristic with this type of feed system when used with tungsten particles). Accordingly, in the present program, a new type and improved particle feeder system was developed.

Objective

The objective of the particle feeder system research effort was to develop the equipment and technology required for injecting tungsten particles in a uniform and controllable manner into the rf plasma IRG configuration at chamber pressures up to 40 atm. In addition, the system selected should be such that it can be extended in capability for future use in rf plasma tests at chamber pressures up to 500 atm.



## Description of Equipment and Procedures

Several types of particle feeder systems were investigated, and exploratory tests were conducted, before the feeder system used in the tests reported herein was selected. These included systems employing tungsten powder in both the pre-packed and non-prepacked form. Three candidate particle feeder systems were considered in detail; Appendix A contains a discussion of these systems and the associated exploratory tests conducted. Also contained in Appendix A is additional information on the tungsten particles employed in the tests.

A schematic diagram of the basic particle feeder system used in the cold-flow tests reported herein is shown in Fig. 27. Based on component stress limitations, the maximum canister pressure was limited to 2.5 atm. A photograph of the modified high-pressure particle feeder system as used in the rf plasma hot-flow tests at pressures up to 40 atm is shown in Fig. 28. The difference is primarily in the incorporation of a high-pressure canister and deagglomerator assembly. Also included were modifications to the valves, lines, and fittings to provide a smooth flow path for the seed-laden stream. The thick-wall steel pressure canister and tie-bolts are visible in Fig. 28. The design of the system is such that extension of the seeder capability to 500-atm operation would involve only fabrication of a new canister assembly and some associated hardware.

For most of the tests, approximately 100 g of tungsten powder was loaded into the canister. A variable-speed motor control (see Fig. 28) permitted the perforated wheel carrying the particles to be varied in speed over a range from zero to 1.4 rad/sec. A valve located downstream of the deagglomerator (see Fig. 27) permitted the seeds and carrier gas to be directed into either the transfer line connected to the simulated-fuel injection probes or the line connected to the seed collection system. The seed collection system, composed of a foam collector and balance system, permitted measurements of the time-averaged seed mass flow rate. The system was completely purged with argon gas after each test sequence.

The cold-flow seeding tests using the basic particle feeder system were conducted under a hood and utilized a synchronous variable-speed motor to drive a spool of chart paper perpendicularly in front of the tip of the simulated-fuel injection probe (see Fig. 27). The probe tip was positioned 5 cm away from the paper. This distance is representative of the distance between the probe tip and center of the rf plasma in the IRG configuration. The paper feed rate could be varied to speeds up to 0.5 m/sec. This permitted the steadiness and flow characteristics of the particle-laden stream to be monitored continuously. In all the cold-flow tests, the seed carrier transfer line lengths were chosen to closely simulate the requirements of the hot-flow seeding tests to be conducted using the 1.2-MW rf heater system and the 7/8-scale IRG configuration.

After fabrication and assembly of the high-pressure modified particle feeder system, hydrostatic tests were successfully conducted to 110 atm. To investigate the performance of the modified feeder system at high discharge chamber pressures, an approximately 400 cm<sup>3</sup> stainless-steel pressure vessel (autoclave) rated for 200-atm operation was employed. This volume is approximately equal to that of the 7/8-scale IRG test chamber used in the rf plasma tests. Figure 29(a) is a photograph showing the test arrangement. Two 6.4-cm-diam, 2.5-cm-thick fused silica view ports were used to allow visual observations and photographs to be made of the seeds (Fig. 29(b)) as they were discharged from the tip of the simulated-fuel injection probe.

In the hot-flow tests, the argon carrier gas was set at a predetermined value prior to initiating the seed flow. The rotary wheel variable-speed motor control was also preset; this permitted the seeded stream to be actuated solely by the drive motor on-off switch. At the end of a test, both the argon carrier gas and the drive motor were shut off simultaneously. This eliminated the possibility of seed material which may have collected in the transfer lines from being discharged in a random manner into the test chamber.

#### Discussion of Test Results

Figure 30(a) is a photograph, taken during the initial cold-flow tests, of the strip-chart paper trace of the tungsten particles discharged from the simulated-fuel injection probe shown in Fig. 27. In this particular test, which is representative of the initial tests with the particle feeder system, no deagglomerator was used. During these tests the seed-laden carrier-gas stream was periodically diverted into the plenum containing the foam filter assembly (see Fig. 27). Determination of the tungsten seed mass flow rate was made by weighing the particles which accumulated in the plenum over a 2-min time interval. For the data shown in Fig. 30, the strip-chart paper feed speed was 0.5 m/sec from left to right.

After incorporating the various modifications to the feeder system discussed previously and in Appendix A, a considerable improvement was noted in the steadiness of the seed-laden stream. Inclusion of the deagglomerator significantly improved the steadiness of the flow as did switching to a different vendor for tungsten particles. The tungsten particles from the new vendor had a nominal diameter of approximately 0.1  $\mu$ , compared with the 1-to-10- $\mu$  nominal diameter range of the particles from the prior vendor. Appendix A contains additional information on the 0.1- $\mu$  nominal diameter tungsten particles.

Figures 30(b) and 30(c) illustrate the improvements obtained using the modified particle feeder system. Note that the tungsten seed mass flow rate was increased by about a factor of two in each case. With this system it was possible to provide a steady and controllable stream of tungsten particles for many minutes (limited

solely by the tungsten loading in the canister) and then to shut the seeder off and start another test with reproducible results.

Using the test configuration shown in Fig. 27, three simulated-fuel injection probes having different inside diameters (0.08, 0.168 and 0.232 cm) were tested over a range of argon carrier-gas and tungsten particle flow rates. A summary of the test results is given in Table III. Note that in these tests, only a single simulated-fuel injection probe discharging into atmospheric pressure was used. For the range of test conditions shown, a steady and easily controlled stream of tungsten-laden argon resulted. The upper limits shown in Table III were primarily based on the pressure limitation (2.5 atm) of the canister. However, with the 0.08-cm-diam probe and the 0.232-cm-diam probe, argon carrier-gas flow rates less than 0.09 g/sec and 0.12 g/sec, respectively, resulted in plugging of the feeder system transfer lines. This usually occurred in the vicinity of the probe exit. The results of these tests indicate that it is important in handling tungsten-particle gas mixtures to maintain the flow rates and carrier-gas velocities high enough to eliminate any settling out and/or accumulation in the lines.

One of the most important aspects of these tungsten feeder system tests was tungsten mass flow reproducibility. All the tungsten mass flow rates at a given condition could be reproduced to within about 2 percent.

Prior to the rf plasma tests, a series of high-pressure cold-flow tests was conducted using the test arrangement shown in Fig. 29(a). Table IV is a summary of the test conditions employed in the tests. In these tests, only the 0.168-cm-i.d. simulated-fuel injection probe was used. A range of autoclave chamber pressures between 1.0 and 40 atm were used to verify that satisfactory operation of the feeder was possible at intermediate pressures. The tungsten mass fraction (defined as the mass flow rate of tungsten divided by the mass flow rate of argon plus tungsten in the simulated-fuel injection probe) ranged from 0.09 to 0.3. The maximum tungsten seed mass flow rate reached was 0.134 g/sec. This upper limit was based on the motor drive gear system used with the particle feeder. Figure 29(b) shows a 0.168-cm-i.d. simulated-fuel injection probe discharging tungsten particles into the autoclave at a chamber pressure of 40 atm. The corresponding tungsten mass flow rate is 0.038 g/sec.

Satisfactory test results obtained with the modified particle feeder system prompted the decision to use this type system, modified for high-pressure operation as discussed in the previous section, in the 7/8-scale IRG configuration rf plasma tests employing particulate seed material. These tests are discussed in the following section.

## RF Plasma Tests at Pressures up to 40 Atm Using 7/8-Scale IRG Configuration and Tungsten Particle Feeder System

### Background

During FY 1971 (Ref. 16), several preliminary rf plasma tests were conducted using 1-to-10- $\mu$  nominal diameter tungsten particles and a worm-screw type particle feeder system. The aim of these initial tests was to inject the particulate seed material into the rf plasma region with minimum deposition of the seed material on the transparent peripheral wall. Due to the pressure limitation on the powder canister, the maximum chamber pressure reached in the tests was only about 2 atm. Due to this low chamber pressure, the argon vortex buffer-gas weight flow rate was reduced to permit maintaining relatively low radial accelerations (comparable to those expected in an early in-reactor test configuration --- 20 to 50 g). In these tests, the tungsten seeds were fed into the test chamber through a single simulated-fuel injection probe located in the thru-flow duct of one end wall. The total rf power deposited into the plasma in these tests was approximately 35 kW. Random pulsations occurred in the tungsten feeder system which adversely affected the diagnostic read-outs during the hot-flow tests. In addition, relatively large diameter particles were noted rotating in the test section at approximately the axial midplane location. Post-test inspection of the inner transparent wall indicated some wall coating and several grams of tungsten particles (approximately 100- $\mu$  diam) were found loose at the bottom of the model at the axial midplane location.

These preliminary tests indicated further research was required to develop a particle feeder system capable of operating in a steady and controlled manner, and capable of injecting tungsten particles into a high-pressure, high-radiant-energy-flux plasma. The particulate simulated-fuel injection tests reported herein have emphasized tests at both higher pressure and higher power levels using an approximately full-scale version of an in-reactor test configuration.

### Objective

The primary goal was to conduct tungsten-argon rf plasma tests at pressures up to 40 atm with simulated fuel in particulate form injected into the plasma, and with minimum deposition on the transparent peripheral wall.

### Description of Configuration and Procedures

The test configuration used in the majority of tests was similar to that shown in Fig. 10(b). To maintain the buffer-gas injection velocities low, eight 0.234-cm-i.d. vortex injectors were used on each end wall. Two types of simulated-fuel

injection probes were used; a 3-concentric-tube type with an i.d. of 0.17 cm and a 4-concentric-tube type with an i.d. of 0.09 cm. Each probe was located concentrically within the thru-flow duct and the probe tip protruded 1.9 cm into the test chamber from the face of the end wall. Additional details on the 3-concentric-tube type probe are contained in Ref. 16. Details of the 4-concentric-tube type probe are discussed in the following section.

Prior to hot-flow tests, the test chamber was statically pressure checked to 40 atm. The rf plasma was initiated in the test chamber using the vacuum and resonator voltage breakdown technique discussed earlier. In all tests, argon served as the carrier gas for the submicron-sized tungsten particles (nominal diameter of  $0.1 \mu$  - see Appendix A). The modified high-pressure particle feeder system shown in Fig. 28 and discussed in the previous section was used in all tests.

Several exploratory tests were conducted using only argon carrier gas in the probes. This permitted an estimate to be made of the effects of the argon carrier-gas weight flow rate and injection velocity on the behavior of the rf plasma. Early tests indicated that the discharge was very sensitive to changes in the carrier-gas weight flow rate. Part of this was attributed to the relatively low power levels (less than 40 kW) used in these tests. In general, the exploratory tests helped establish operating conditions compatible with the simulated-fuel injection flow rates used such that minimum distortion of the plasma discharge occurred. When argon carrier-gas flow rates exceeded a certain value, corresponding to a given set of test conditions (i.e., total discharge power, buffer-gas weight flow rate, and chamber pressure), distortion occurred in the central region of the plasma where the cores of the two stream of high axial convection interacted. Indications of plasma unsteadiness also occurred in the end regions near the probe tips; this was particularly true in tests when the axes of both simulated-fuel injection probes were not colinear.

### Discussion of Test Results

Typical test results using the 7/8-scale IRG configuration are presented in Table V. Included are the rf operating conditions, vortex flow conditions, and simulated-fuel flow conditions. The five cases shown, both with and without tungsten simulated-fuel injection, cover a chamber pressure range from 10 to 40 atm. Adjustments were made in the exhaust gas back-pressure valve after initiation of the argon seed carrier to permit maintaining approximately constant chamber pressures. For the data shown in Table V, the rf plasma was operated steady-state with the tungsten seed material injected for a fixed time interval of 2 min.

The equivalent black-body radiating temperatures achieved were in the range of interest for the reference Nuclear Furnace IRG test ( $3333^{\circ}\text{K}$ ). In all cases except Case V, the equivalent black-body radiating temperature increased when the

tungsten simulated-fuel was injected into the plasma. A corresponding increase was also noted in the total discharge power and the fraction of total discharge power that was transmitted through the inner peripheral wall. In contrast, Case V showed a significant decrease in both the equivalent black-body radiating temperature and the fraction of total power transmitted through the inner peripheral wall. In addition, the total power deposited into the plasma decreased. It was during this 40-atm test with simulated-fuel injection that a dark deposit partially coated (nonuniformly) the outside of the 57-mm-i.d. fused silica tube. This occurred primarily at the axial midplane location. This affected the radiometer measurements used to determine the radiation emitted and in turn the total power deposited into the plasma. Additional details of this coating are discussed in Appendix B. It is believed to be due to deterioration of the nigrosine dye due to strong uv absorption. The coating which occurred during the 40-atm test did not permit a recalibration radiation check to be completed. Therefore, it is not known exactly how much of the total power decrease was due to partial blockage of the radiometer due to coating and how much was due to an actual decrease in total rf power deposited into the plasma (decrease in coupling efficiency into the load). Case V had the highest injection flow rate of tungsten seeds (0.13 g/sec --- a factor of two greater than the other cases) and quite possibly an impedance mismatch occurred which may have significantly affected the coupling efficiency. This may necessitate retuning and a change in rf operating frequency in future tests when still higher tungsten seed weight flow rates are employed.

To permit an estimate of the quantity of tungsten seed material left within the test chamber after a typical high-power/high-pressure test, the configuration was carefully disassembled after the Case IV test. Prior to disassembly, all the cooling water was purged from the individual components to eliminate contamination of the seed material. Figure 31 is a photograph taken before the test chamber was removed from the test tank. Both end walls and probes had a fairly uniform coating of the tungsten seed material. This coating is visible in the photograph and was easily removed. A relatively light coating was located within the 57-mm-i.d. fused-silica tube at the axial midplane and at the end sections adjacent to the buffer-gas vortex injectors. The deposit collected from the end walls and tips of the simulated-fuel injection probes was weighed. The measurements indicated approximately 57 mg had deposited on these surfaces. The material removed from the fused silica tube was less than 10 mg. The exact quantity of seed material deposited during the actual seed test time (2 min) was difficult to determine accurately. Part of this accumulation occurs during the initial start-up and shutdown of the flow of tungsten seed material into the test chamber. After future tests, in addition to measuring the weight of material deposited on the wall, radiation attenuation and densitometer measurements should be made at several points on the tube to permit comparisons between the wall coatings in different tests.

The presence of tungsten in the argon rf plasma was evident from the color change and from spectral emission data taken from 3700 Å to 6500 Å. As an example, Figs. 32 and 33 compare representative emission spectra between 4000 Å and 4400 Å obtained from the argon plasma alone and with the addition of the tungsten. The test conditions correspond to those of Case III in Table V. The data were taken on the centerline of the discharge at the axial midplane location. Catalogued argon I and tungsten I lines are indicated in Figs. 32 and 33 over a wavelength interval where the tungsten lines present were relatively free from the influence of overlapping argon lines.

In general, the test results are encouraging. They demonstrate that submicron-sized tungsten particles can be uniformly injected into an rf plasma in an approximately full-size IRG test configuration. These tests were at chamber pressures up to 40 atm with approximately 100 kW of rf power deposited into the plasma. The corresponding equivalent black-body radiating temperature,  $T^*$ , ranged from about 3000 to 3600°K. The maximum tungsten injection flow rate employed was 0.13 g/sec and was limited solely by the motor-gear drive in the particle feeder system. The maximum simulated-fuel mass fraction ratio achieved was 0.06.

It is expected that similar results will be obtained with uranium dioxide particles as the simulated fuel. With appropriate modifications to the high-pressure particle feeder system, the test results and experience gained in the present program should lead to significant increases in the mass ratios in future tests. This will aid in increasing the mass of fuel contained in the plasma; approximately 6 g of fuel will be required for simulation of the in-reactor test when the pressure is increased to 500 atm. Future tests will have to include investigations of the rf system coupling efficiency and impedance matching aspects, particularly when increased concentrations of simulated fuels are introduced into the plasma.

#### RF Plasma Tests at Pressures up to 40 Atm Using 7/8-Scale IRG Configuration and Injection of Uranium Hexafluoride ( $UF_6$ )

##### Background

Preliminary gaseous simulated-fuel injection tests were conducted in FY 1971 (Ref. 16) using dilute concentrations of  $UF_6$  in an argon carrier gas. A glass-lined pressure canister (rated working pressure of 10 atm) was used to store the pressurized, premixed simulated fuel. A neutralizing gas trap was used to trap the exhaust gases during the rf plasma tests.  $UF_6$  concentrations up to 0.5 percent (by partial pressure) relative to the carrier gas were employed. The tests were conducted at chamber pressures up to 5 atm and total discharge power levels up to 55 kW.

The results of these preliminary tests indicated that the discharge was very sensitive to changes in any of the primary variables. In addition, operating the plasma steady-state with  $UF_6$  injected for several minutes resulted in no significant deposition of uranium or uranium compounds on the inner fused silica tube.

### Objective

The primary goal was to conduct uranium-argon rf plasma tests at pressures up to 40 atm with simulated fuel in gaseous form injected into the plasma, and with minimum deposition on the transparent peripheral wall.

### Description of Equipment and Procedures

Figure 34 shows a cross section of the test configuration used in the gaseous simulated-fuel injection tests. This test configuration is similar to that shown in Fig. 10(b). The principal difference is in the end-wall assemblies, interstage heat exchangers, and use of 4-concentric-tube type simulated-fuel injection probes.

The new end walls used in this test configuration contain enlarged thru-flow ducts (1.14-cm diam) to accommodate the 0.89-cm-o.d., 4-concentric-tube type probes. In the assembled test configuration, the spacing between the end walls was maintained at 15.5 cm. To establish the desired radial-inflow vortex flow pattern, eight 0.234-cm-i.d. stainless-steel vortex injectors were located equally spaced around the periphery of each end wall. These injectors were located flush with the end-wall face such that the argon buffer gas enters the vortex chamber in a circumferential direction only. The relatively large i.d. of the vortex injectors was selected, as in previous tests, to provide low injection velocities, thus minimizing the radial accelerations present in the fuel region.

Figure 34 shows the location of one of the pair of probes and an interstage heat exchanger. This heat exchanger was constructed to permit operation with the new type probes. It also provides adequate cooling for the hot exhaust gases, particularly at the interface between the exit of the end-wall thru-flow duct and the entrance to the interstage heat exchanger. In addition, the interstage heat exchanger design permits rapid removal of the fuel probes for inspection, cleaning or repair. Moreover, the axial position of the probes can be adjusted should another axial location of the probe tip provide better fuel-injection characteristics in future tests.

Figure 35 shows a cross-sectional sketch of the tip region of the 4-concentric-tube type simulated-fuel injection probe. These 23-cm-long, water-cooled probes were fabricated from four tubes. The outside diameter of the probe is 0.89 cm. The outer three tubes form the water-cooling passages. The innermost and outermost tubes are copper; the other two tubes are stainless steel. Cooling water



enters the rear end of the probe and flows meridionally around the tip region (accomplished using the concentric annular spaces shown in Fig. 35). These probes were water flow checked at inlet pressures up to 34 atm. To permit maintaining the simulated fuel at higher temperatures than the adjacent water-cooled copper tube, another inner annulus was added. This provides an insulating air space between the fuel and the adjacent water-cooling passage.

Calculations were completed and separate simulated-fuel quench tests were conducted using these probes to verify that the temperature of the simulated fuel flowing in the inner probe-passage could be maintained above  $64^{\circ}\text{C}$ ; which is the condensation temperature for solidification of pure  $\text{UF}_6$  vapor at 40-atm pressure. Figure 37 shows the vapor pressure curve for  $\text{UF}_6$ . In the probe quench tests, argon was used as the simulated fuel and electrical resistance tape was used to preheat the argon to the desired temperature at the probe inlet. The probe was instrumented with copper-constantan thermocouples at the cooling water and gas inlets and exits. A calibrated temperature recorder was used to continuously monitor the temperature variations. For comparison, similar quench tests were conducted with the 3-concentric-tube type probes used in the tungsten particle simulated-fuel injection tests. The test results indicated that the exit temperature of the gas passing through the inner passage of the probe closely approached the bulk cooling water temperature of the probe. This was true over a relatively wide range of cooling water temperatures, argon gas preheat temperatures, and gas mass flow rates. It was not desirable to raise the bulk temperature of the probe cooling water significantly above  $64^{\circ}\text{C}$  during actual hot-flow tests with the probe tip in the plasma. This is what motivated the incorporation of the annular insulating air gap in the 4-concentric-tube type probe design. The results of quench tests with the new probes indicated that cooling water temperatures of 5 to  $10^{\circ}\text{C}$  above room temperature are sufficient, within the range of simulated-fuel carrier-gas flow rates tested (0.45 to 1.5 g/sec), to maintain the gas temperatures at the tip of the probe above approximately  $64^{\circ}\text{C}$ .

Figure 36 is a schematic of the flow system used. The schematic also shows the pressurized argon system used for the vortex buffer-gas injection. A stainless-steel high-pressure canister (rated working pressure of 200 atm) was used to store the pre-mixed simulated fuel. An electrical heater assembly surrounding the pressure canister kept the pressure canister and simulated fuel at an elevated temperature. The batching procedure used is discussed in Ref. 16. Figure 36 shows the location of the various flowmeters and monitoring equipment used, the location of the electrical resistance heater tape, and the simulated-fuel exhaust gas neutralizing trap.

The operating procedures used during typical tests employing gaseous simulated-fuel injection were similar to those for the rf plasma with tungsten particles. The rf plasma was initiated in the test chamber using the vacuum and resonator voltage-breakdown technique.

During exploratory tests conducted prior to simulated-fuel injection, argon carrier gas (without  $UF_6$ ) was injected through the simulated-fuel injection probes into the plasma. As in earlier tests, this helped establish operating conditions and flow rates which reduced disturbances to the rf plasma.

For tests using the premixed  $UF_6$  simulated fuel, the transition from pure argon carrier gas to premixed simulated fuel was made at the high-pressure operating test condition. In the majority of tests, the rf plasma was operated steady-state with the  $UF_6$  simulated fuel injected for a fixed time interval of 1 min.

### Discussion of Test Results

Typical test results using the 7/8-scale IRG configuration are presented in Table VI. Included are the rf operating conditions, vortex flow conditions, and simulated-fuel flow conditions. The five cases shown, both with and without  $UF_6$  simulated-fuel injection, cover a chamber pressure range from 4 to 40 atm. In all cases, except Case I, adjustments were made in the exhaust gas back pressure during the simulated-fuel injection portion of the test to permit maintaining approximately constant chamber pressures. As noted, the tests were conducted at pressures similar to those used in the particulate simulated-fuel injection tests.

In all tests, the equivalent black-body radiating temperatures (see Table VI) increased when the  $UF_6$  simulated-fuel was injected into the plasma. The levels attained were in the range of interest for the reference Nuclear Furnace IRG test conditions ( $3333^\circ K$ ). The injection of  $UF_6$  simulated-fuel into the plasma was also accompanied by an increase in both the total power deposited into the plasma and the fraction of total discharge power that was transmitted through the inner peripheral wall. The presence of the uranium in the argon plasma was evident from the diagnostic measurements and color photographs taken during the tests.

Included in these tests were measurements to demonstrate the feasibility of using the end-wall optical view ports to determine the "edge-of-plasma" location in future tests employing a filament-wound tube pressure vessel where direct side-on measurements are not possible. The maximum plasma diameters attained in the tests (2.4 cm) precluded use of the view port location corresponding to a plasma diameter of 3.4 cm (radius ratio of 0.6). The view port location corresponding to a plasma diameter of 2.28 cm (radius ratio of 0.4) was used during the test series. The results of these tests indicated the optical system provided a sufficiently strong light intensity to be transmitted by the fiber optics to the photomultiplier assembly. This intensity varied with plasma diameter and was correlated with side-on measurements using the optical scanning system. This permitted an approximate determination of the "edge-of-plasma" location relative to the inner peripheral wall. Thus, it was concluded that with several closely spaced view ports, it will be possible to make satisfactory measurements of the "edge-of-plasma" location.

Results of the spectral emission and radiation measurements for a test with 1 percent (by partial pressure)  $UF_6$  as the simulated fuel are shown in Fig. 38. These data correspond to the test conditions of Case I shown in Table VI. The spectral emission data shown in the graph on the left of Fig. 38(a) were obtained using the optical system shown in Fig. 8. In selected tests, spectral emission measurements were made on the discharge diameter at the axial midplane at wavelengths from 3700 Å to 6500 Å. Figure 38(a) shows a representative portion of the emission spectrum between about 3940 Å and 4340 Å. The wavelengths for several of the known argon I lines are denoted on the abscissa. The argon-only trace is shown at the bottom; the argon plus 1 percent  $UF_6$  trace is shown on top. The corresponding test conditions are shown in the table in Fig. 38. No argon carrier gas was injected through the simulated-fuel injection probes during the argon-only test condition. The argon buffer-gas flow rate was 2.7 g/sec for both test conditions. This corresponds to a buffer-gas injection velocity of about 16 m/sec. No attempt was made to re-adjust the chamber pressure back to the argon-only test condition. Thus, part of the increased radiation may be attributed to the 1 atm increase in chamber pressure.

To illustrate these effects, the bar graph in Fig. 38(b) shows the approximate spectral distribution of power radiated through the peripheral-wall coolant. These measurements were obtained using the radiometer system shown in Fig. 7. A low-speed synchronous motor and speed reducer was added to the radiometer system to permit continuous display of the radiation output in various wavelength bands on a strip-chart recorder. The ordinate shows the fraction of the total discharge power that is radiated through the two fused silica tubes and the peripheral-wall cooling water (no dye). The abscissa indicates the breakdown in the four wavelength bands. A significant increase in the radiation, particularly in the visible and near-uv, is noted. The injection of the  $UF_6$  simulated fuel also affected the electrical characteristics of the plasma (reflected impedance). The impedance of the plasma is determined by its size and electrical conductivity. An impedance change results in a change in the total rf power coupled into the plasma. In these tests, no change was made to the saturable reactor power control of the 1.2-MW rf power supply during the without and with fuel condition.

Figure 39 shows photographs of the 7/8-scale IRG test configuration both with and without injection of  $UF_6$  at a chamber pressure of 20 atm. Figure 39(a) is a view through the central view port with no plasma present. Refer to Fig. 34 for additional details of the test configuration. Figure 39(b) shows the rf plasma operating steady-state at the 20-atm test condition prior to injection of simulated fuel. The corresponding equivalent black-body radiating temperature,  $T^*$ , was 2440°K. Figure 39(c) illustrates the results of injecting the  $UF_6$  simulated fuel (1 percent concentration). Note that with simulated-fuel injection, the equivalent black-body radiating temperature increased to 3300°K, approximately the value corresponding to the reference IRG test. As in earlier tests, the saturable

reactor power control was not changed once the 20-atm test condition was reached. The film and camera settings used for these photographs are shown at the right. Note the change in intensity with the increased f/stop setting between Figs. 39(b) and 39(c).

Post-test inspection after each simulated-fuel injection test conducted in the moderate-pressure/moderate-power regime (i.e., 5 atm, 50 kW) revealed no significant coating on the inner peripheral wall. In the majority of tests, a slight greenish-white deposit was noted on the copper end-wall assemblies, the simulated-fuel injection probes, and the ends of the inner transparent peripheral wall in the vicinity of the vortex injectors. Part of this may be attributed to a secondary flow effect near the end wall and vortex injectors. To determine the nature of this coating, a series of tests using an electron probe microanalyzer was conducted. A cluster of the deposit was removed from the test chamber peripheral wall following the simulated-fuel injection test. An electron beam, from the electron probe microanalyzer, was focused on the surface of the specimen. The beam energy used was 20 kV with a focused beam diameter of approximately  $1.0\ \mu$ . The irradiated specimen emitted a spectrum of characteristic x-rays which were diffracted using a crystal and then analyzed by means of an x-ray spectrometer. Photomicrographs of the distribution of an element within the sample were obtained by scanning the beam and spectrometer across the specimen. Figure 40 presents photographs which indicate the distribution of uranium, oxygen, and fluorine, respectively, on a cluster of deposited particles removed from the test chamber peripheral wall. The magnification used was 330. For reference, a  $30\text{-}\mu$  division is indicated in the top photograph. In each photograph the white area represents the distribution of the particular element. Analysis of the results of the tests indicated the primary constituent to be  $UF_4$ .

Figure 41 is a photograph of several of the 57-mm fused-silica tubes used in the simulated-fuel injection tests. At the far left is a new (as-received) tube. This tube has not been flat ground at the ends to the tolerances required by the O-rings; following the grinding process, the tubes were furnace annealed and the ends flame polished. Prior to rf plasma tests, all tubes were inspected under polarized light to verify the absence of stresses. The middle tube shown in Fig. 41 illustrates the type of local coating which occurred during initial simulated-fuel injection tests using  $UF_6$  when the buffer-gas injection velocity was relatively high. In this particular test, many small cracks developed in the vicinity of the coating, prohibiting use of the tube for another test. The tube at the far right of Fig. 41 illustrates the unexpected dark deposition which occurred on the o.d. of the 57-mm tube during several of the simulated-fuel injection tests. This deposition occurred with both simulated fuels and high-power/high-pressure test conditions. The coating was generally heaviest near the axial midplane of the tube. The coating was analyzed using an infrared spectrophotometer. The results indicated the deposit was carbon-like with some absorbed dye. It is believed to be caused by uv deterioration of the nigrosine dye (see Appendix B for additional discussion).

## Simulated-Fuel Containment Measurement Techniques

### Background

Recent rf plasma tests have demonstrated success in injecting gaseous and particulate simulated fuels ( $UF_6$ ,  $WF_6$ , W) through injection probes located on the axial centerline of each end wall. The tests were conducted using geometries configured in general like the Nuclear Furnace IRG unit cell. The results indicate that a condensible simulated fuel can be injected in sufficiently strong concentrations to significantly alter the characteristics of the plasma while the transparent peripheral wall is maintained relatively deposit-free. For successful operation of the full-scale reference engine and in-reactor test configuration, average fuel partial pressure ratios of 0.35 and 0.25, respectively, must be attained. Average simulated-fuel partial pressure ratios of the same magnitude should be demonstrated in rf plasma tests prior to any in-reactor tests. Thus, a diagnostic technique to determine the amount of simulated fuel contained within the test chamber is required.

The technique selected must be applicable over a pressure range from 40 to 500 atm and usable in the 1.2-MW rf induction heater where there are constraints due to high voltages and a small allowable size envelope. Also, at pressures above 40 atm, a fiberglass filament-wound pressure vessel is used which allows no direct visibility of the vortex chamber. It is desirable that the method selected yield information about the distribution of the simulated fuel, as well as the total amount of simulated fuel contained.

Measurement techniques utilized in the past were all based on light absorption or emission in a certain wavelength band by a gaseous simulated fuel (see Refs. 21, 24, and 25). These techniques require a high degree of visibility not available in high-pressure test configurations which have an opaque fiberglass filament-wound pressure vessel.

### Objective

The objective in this portion of the fuel region research program was to determine candidate techniques for the measurement of the amount and, if possible, distribution of simulated fuel contained within the vortex region of the rf plasma IRG configuration. These techniques must be capable of application within an rf environment at chamber pressures up to 500 atm using fiberglass filament-wound pressure vessels.

### Discussion of Results

In this portion of the fuel region research program, three proposed containment measurement schemes have been evaluated. The methods investigated involve the use of (1) a time-of-flight mass spectrometer, (2) a radioactive tracer, and (3) gamma-ray absorption.

In the first method, time-of-flight mass spectrometer measurements are made using a tracer gas added to the simulated fuel in a known ratio to determine the amount of simulated fuel contained in the chamber of the test configuration. A schematic of a time-of-flight mass spectrometer system which could be used for making these measurements is shown in Fig. 42. Under steady-state conditions, a tracer gas (such as xenon) is mixed with the simulated fuel just prior to injection into the chamber. The mass spectrometer is used to continuously measure the concentration of tracer gas exhausting from the system after the tracer gas supply is shut off. A typical output curve from the mass spectrometer is also shown in Fig. 42. The tracer gas concentration is easily converted to simulated-fuel flow rate since both are injected in a known ratio. By integrating the output of the mass spectrometer and subtracting the known amount of simulated fuel in the inlet and exhaust lines, the amount of simulated fuel in the vortex chamber at the instant the tracer gas supply is shut off can be determined. Calculations show that this method appears feasible if the volume of the inlet and exhaust lines can be maintained very small, namely, on the order of 1 percent of the chamber volume. For the rf plasma tests reported herein, the volume of the 7/8-scale IRG configuration is approximately  $400 \text{ cm}^3$ .

Preliminary analyses were conducted to determine whether a radioisotope tracer or gamma-ray absorption could be employed to measure the density or mass of simulated fuel contained in the rf plasmas. In investigating the feasibility of these measurement techniques, two test configurations were considered: (1) the 40-atm test configuration with a fused silica tube as a pressure vessel, shown in Fig. 34; and (2) the 500-atm test configuration with a filament-wound tube as a pressure vessel, similar to the lower-power version shown in Fig. 20. In both cases, absorption of gamma- or x-rays by the gases in the plasma chamber, by the coolant materials, and by the pressure vessel materials were included in calculating the transmitted radiation fluxes. The radiation flux transmitted through these materials would be used to determine the contained simulated-fuel mass.

Preliminary results of the radioisotope tracer analysis indicate that a gaseous tracer with gamma-ray energies greater than 100 keV could be employed to determine the contained mass in the vortex chamber by measuring the radiation intensity at the outer surface of the pressure vessel at the axial midplane in either the 40-atm or 500-atm tests. The specific activity of such a tracer should be on the order of  $10^5 \text{ Ci/g}$  (approximately 10-day half-life). Further investigations would be necessary to determine the most desirable tracer element to be employed. Considerations such as cost, safety and handling difficulties also remain to be thoroughly evaluated; however, this method does not appear to be as technically advantageous as the gamma-ray absorption method in any case.

The use of gamma-ray absorption to determine the density of simulated fuel in the vortex chamber was also investigated. Methods for measuring absorption across

both chordal and axial paths through the chamber were evaluated. Due to gamma-ray absorption by the pressure vessel walls and the annular coolant layer, it was determined that chordal absorption measurements would not have the sensitivity required to accurately determine the density of simulated fuel in the plasma. However, gamma-ray beams passing axially through the chamber at different radial stations could be employed to detect the presence of simulated fuel. In particular, when the simulated fuel is uranium, the presence of K and L absorption edges results in photoelectric absorption cross sections, in the energy range from 10 to 150 keV, which are much greater than those for the argon buffer gas. The results of the analyses indicate that it might be possible to detect concentrations of uranium in argon gas at a level of one uranium atom for every one thousand atoms of argon.

Necessary model modifications which would permit gamma-ray absorption measurements to be made are included in the 40-atm test configuration sketch shown in Fig. 43. Gamma-ray absorption measurements could be obtained at approximately ten radii by modifying the end walls to include view ports. After modification, each view port in the left end wall in Fig. 43 (only one is shown for simplicity) would consist of an evacuated stainless-steel tube with a thin (0.025 to 0.05 cm) beryllium window in the end-wall face. A partially collimated beam of gamma-rays would be transmitted across the vortex chamber from each of these view ports. The opposing view ports in the right end wall would consist of a similar beryllium window and a short stainless-steel tube. The tube would contain an inorganic phosphor such as sodium iodide (NaI) activated with thallium which fluoresces, emitting visible light, when irradiated by gamma-rays. This light would be transmitted by fiber optics to a previously calibrated radiometer. The density of the material traversed by the gamma-ray beam could be determined from the radiometer measurements. The data from all view ports would be integrated to obtain the total amount of simulated fuel contained in the vortex chamber. Thus, with this method both the distribution and total amount of contained simulated fuel could be determined.

In using any absorption technique it is desirable to obtain the maximum sensitivity to the material being measured. For a given material at a fixed density, the total gamma- or x-ray absorption coefficient is dependent only on the photon energy level. The sensitivity of the photons to the presence of fuel can be indicated by the product of the path length times the difference of the absorption coefficients with fuel and without fuel. This product is designated a sensitivity parameter and is plotted versus beam energy level in Fig. 44. Four cases are shown: a radial path and an axial path, each calculated for 40-atm and 500-atm total chamber pressures. The radial path is much shorter than the axial path and traverses through the pressure vessel walls, the annular coolant, and the inner transparent wall. This makes the radial path much less sensitive than the axial path (as shown in Fig. 44). The calculations for these curves are based on the test chamber configuration and dimensions shown in Fig. 43 and assume that the fuel is uranium with a density ratio (relative to argon buffer gas at the edge of fuel) of 0.7 and that the radius ratio,  $r_6/r_1$ , is 0.5. Because the absorption coefficients are proportional

to density, the values of the sensitivity parameter shown on Fig. 44 for a pressure of 40 atm are increased by a factor of 12.5 ( $500 \text{ atm}/40 \text{ atm} = 12.5$ ) for a pressure of 500 atm.

As might be expected, the gamma-beam sensitivity to the fuel is highest at low energy levels and generally decreases with increasing energy level except at the K- and L-shell electron edges (Fig. 44). However, it is not necessarily advantageous to operate at the lowest energy level since this results in greater absolute attenuation of the beam energy by the argon buffer gas and pressure vessel walls. A minimum beam energy level is required which depends on obtaining an adequate "signal-to-noise" ratio after absorption by the beryllium windows and by the argon buffer gas. A beam energy level which results in the beam path through the test region being equal to approximately 0.1 to 1.0 absorption mean-free-path lengths is desired.

If the sensitivity parameter shown in Fig. 44 is multiplied by the gamma-beam intensity ratio with no fuel ( $I/I_0|_{\text{no fuel}}$ ), an indication of the best operating point can be obtained; i.e., this procedure can indicate the gamma energy level at which the product of sensitivity and beam intensity is maximized. The result is shown in Fig. 45. At 40-atm chamber pressure, the sensitivity-intensity peaks at 21 and 22 keV; at 500-atm chamber pressure, the sensitivity-intensity peaks at 30 keV. Because of the proximity of these energy levels, it seems likely that one source could be utilized for tests at all chamber pressures between 40 and 500 atm. It should be noted that the sensitivity data used in Figs. 44 and 45 were calculated for a region near the centerline of the vortex chamber where a large amount of argon buffer gas was assumed to have been displaced by the uranium fuel. At greater radii from the centerline there will be less argon displaced; therefore, the sensitivity may be reduced. Further investigation is required to determine the exact change in sensitivity that would result.

There are several gamma sources having energy levels in the region of interest (Ref. 26). Two such sources are: (1) cadmium-109 (half life = 453 d) which emits primary gammas at 22 keV (also at 88 keV) and (2) iodine-125 (half life = 60 d) which emits primary gammas at 27 keV (also at 35 keV). A Bremsstrahlung source such as promethium-147/silicon (half life = 2.6 yr) with a useful energy region of 12-45 keV might also be used, although calibration of the system would be more difficult.

Because of the large distance ( $\approx 18 \text{ cm}$ ) from source to detector when this technique is utilized for the IRG configuration (Fig. 43), a relatively high activity source is required. For accuracy of plus or minus 1 percent, a total of  $10^4$  counts is needed (percent accuracy =  $\sqrt{N/N} \times 100$ ). In order to obtain  $10^4$  counts in a reasonably short length of time in the IRG configuration, a source output into  $2\pi \text{ sr}$  of approximately  $5 \times 10^8$  counts/sec (approximately 14 mCi) would be



necessary. A review of standard gamma sources listed by Amersham/Searle Corp. indicates that the three gamma sources mentioned above are available in this activity range at reasonable cost.

The above results indicate that the mass spectrometer method and the axial gamma-ray absorption method are the most promising for simulated-fuel containment measurements. All other things being equal, the gamma-ray absorption method would be favored due to the additional information on distribution of simulated fuel which would be obtained. Further investigation, including preliminary experiments, should be undertaken to establish a workable measurement system.

## TRANSPARENT-WALL MODEL RESEARCH

## RF Plasma Tests with Axial-Coolant-Tube Transparent-Wall Models

Background

The nuclear light bulb engine requires a transparent wall to separate the propellant region from the fuel region and to contain the fuel region vortex flow. This transparent wall must have structural integrity, provision for internal cooling, and provision for tangential injection of a buffer gas. Absorption of thermal radiation from the fuel region by the wall must be minimized.

The transparent-wall structure for each unit cavity of the reference engine (Fig. 1(b)) is 48.9 cm in diameter by 182.9-cm long. The size of the structure and the above constraints make simple transparent-wall designs unsuitable. The bursting stress due to coolant pressure drop in a 182.9-cm length precludes use of two large-diameter concentric tubes or a continuous coiled structure. The most suitable structure would consist of a large number of short, small diameter, thin-walled tubes formed in a circumferential arrangement with provision for neon buffer-gas injection, such as the arrangement shown in Fig. 1 of Ref. 27. Some pertinent dimensions, heat loads and coolant flow rates for the reference engine wall are listed in the first column of Table II.

Internal cooling of the transparent wall is required to remove heat deposited by radiation, conduction and convection. Hydrogen will be employed as the wall coolant due to its high heat capacity and high radiation transmission at low temperatures. The walls must be thin (approximately 0.125 mm) to conduct the heat to the coolant with a suitable wall temperature drop. The inner wall temperature must be high enough (about 800°C) to allow thermal annealing to reduce coloration (which causes increased opacity) due to irradiation from the fuel, yet low enough to maintain high wall strength and minimize devitrification (which normally occurs in fused silica at temperatures of about 1100°C). Therefore, the temperature of the wall must be maintained between relatively narrow limits. Favorable results of irradiation experiments (e.g., Ref. 12) indicate that the net effects of ionizing radiation and optical bleaching of the fused silica may enable a greater temperature difference across the wall to be used ( $\Delta T$  of approximately 500°C). In the engine calculations (Ref. 28), the allowable temperature difference across the wall was assumed to be 111°C. The total heat deposited in the wall is about equally divided between heating from the propellant region side and heating from the fuel region side.

As presently conceived, the engine transparent wall will be made from high purity fused silica. High purity (consequently, high transmission) is necessary to minimize thermal radiation deposition in the walls. The opacity of the wall material in the ultraviolet portion of the spectrum is the primary factor governing radiant heat deposition in the transparent wall. Substitution of single-crystal beryllium oxide for fused silica as the transparent-wall material would result in a significant reduction in the ultraviolet cutoff wavelength (Ref. 12) and a corresponding increase in permissible fuel radiating temperature (Ref. 28). Also, synthetic quartz crystals have been successfully grown with ultraviolet cutoffs as low as  $0.147\mu$  (Ref. 29). However, the difficulty of growing single-crystal beryllium oxide or quartz, as well as the necessary handling and forming operations, preclude their use in tests at the present time. The method most likely to be successful in reducing the wall heat deposition is to seed the fuel and buffer gas with a material which absorbs in the ultraviolet portion of the spectrum where the wall has high absorption characteristics. Further discussion of this approach is available in Ref. 10.

The region outside of the transparent wall in the reference engine will contain hydrogen propellant seeded with tungsten particles to increase its opacity. An unseeded buffer layer of hydrogen will be maintained along the transparent wall to keep the seeds off the wall.

Previous work in this program resulted in improved transparent-wall fabrication techniques (Ref. 27) and a model configuration with improved thermal and pressure capabilities (Ref. 16). This model configuration was used in rf plasma tests during FY 1971 which resulted in a maximum pressure of 21 atm, a maximum power in the plasma of 116 kW, and a maximum radiant heat flux on the transparent wall of about  $0.77\text{ kW/cm}^2$ .

### Objective

The ultimate purpose of the transparent-wall model program is to simulate, as much as possible, the thermal environments of the nuclear light bulb engine transparent wall, and of a transparent wall that might be used in in-reactor test models, using the 1.2-MW rf induction heater. The primary objective in the present program was to continuously increase the pressure, the discharge power and the radiant energy flux at the model wall to levels greater than achieved previously. It was desired that this increased performance be achieved using axial coolant tubes having wall thicknesses down to 0.125 mm.

Description of Equipment and ProceduresTransparent-Wall Model Configurations

Several model configurations utilizing both 0.125- and 0.25-mm wall-thickness axial coolant tubes were tested. A sketch of the basic model configuration is shown in Fig. 46. The model consists of two wall segments, each having 30 axial coolant tubes; two fused silica tubes used as pressure vessels; two internally-cooled copper end walls; and two diametrically opposed peripheral-wall argon injectors which span the vortex chamber. A complete description of the model and injector configuration is available in Ref. 16. Except for a few differences discussed below, this basic model was used in the present program.

A major modification to the transparent-wall model in this program was the replacement of the 4.0-mm-wall outer fused silica pressure vessel with one having a 9.0-mm wall. This approximately doubled the allowable chamber pressure (up to about 42 atm). All other components of the model were re-evaluated and it was determined that, with slight modifications, they could also operate at this pressure.

The model transparent walls were again fabricated as wall segments in a jig using a liquid version of the normal silicone rubber potting compound (RTV). This assures that the RTV will flow into the narrow gaps between the tubes where most leaks occurred in past models. However, in this program, the wall segments were fabricated curved instead of flat, resulting in easier installation. Two of these wall segments were then easily potted into the slots in the model end walls.

During this program, axial coolant tubes with nominal wall thicknesses of 0.125 mm were obtained which have substantially more uniform dimensions than any previous tubes of this size. The reason for this is a new process wherein the vendor forms the tubes on a tungsten wire. This results in better control of the tube dimensions. Wall thickness can now be held within approximately plus or minus 20 percent, instead of plus or minus 80 percent.

The same injectors used in the FY 1971 program were used in this test program (see Fig. 31 of Ref. 16). In addition, a new peripheral-wall argon injector, which was similar but would be easier to fabricate, was designed in case a replacement was needed. The new injector design (Fig. 47) has the same overall size (0.64-cm wide x 0.96-cm high x 10.2-cm long) and the same injection area (0.146 cm<sup>2</sup> each injector). Also, the cooling effectiveness is approximately equal to that of the FY 1971 injectors (1.8 kW/cm<sup>2</sup> minimum with 20-atm cooling water inlet pressure, and assuming zero reflectivity at the inner surface). The advantage of this improved design is in the cost of fabrication which is about half that of the previous design. This results from the fact that all cooling passages and the argon slot would be electric-discharge machined. The fifty injection holes would be drilled. All

parts would be either gold-nickel brazed or e-beam welded to assure a high-temperature capability. Quotes on fabrication were obtained from vendors; however, the injectors were not fabricated since the FY 1971 injectors performed satisfactorily, and new ones were not needed.

The complete installation of the transparent-wall model in the 1.2-MW rf induction heater test tank is shown in Fig. 48. The axial coolant tubes and injectors are located concentrically within the rf work coils. Four 0.97-cm-diam steel compression rods (see Fig. 46), arranged symmetrically at each end of the model, transmit the axial load due to the pressure in the model to flanges on the test tank. Axial movement of the flanges is restrained by two 1.27-cm-diam steel tie-rods connecting the flanges. These tie-rods, surrounded by water-cooled copper jackets, are visible in the photograph in Fig. 48. Also visible in Fig. 48 are the disconnect points (unions) which allow the model to be easily installed and removed as a unit from under the rf heater work coils.

#### Test Procedures

In general, the operating procedures employed with the transparent-wall model in the 1.2-MW rf induction heater were the same as those employed with the other models described previously in this report. One major difference in operating technique is the requirement to maintain the model coolant pressure within plus-or-minus 1 to 3 atm of the chamber pressure to prevent rupture of the axial coolant tubes or their sealant.

Diagnostic equipment and data analysis methods were also the same as those described previously in this report. Complete calorimetric measurements were made of the heat input to all cooling water and gas flows, and of the radiant energy escaping the model. The diameter of the plasma was estimated approximately using data from the gas-cooled model tests of Ref. 16 and correcting approximately for the differences in test conditions such as argon flow rate and chamber pressure. This was necessary since a representative plasma diameter determination for the water-cooled model tests was not possible due to the multiple reflections occurring within the model test section which gave a large, diffuse appearance to the discharge, with no defined boundaries. An approximate radiant energy flux was then calculated by assuming an ellipsoidal shape for the discharge.

It was intended to conduct gas-cooled model tests during this program. However, it was obvious from the results of gas-cooled model tests in Ref. 16 that the maximum discharge power obtained of 116 kW could not be exceeded unless a higher temperature potting material were used. In the previous tests, the RTV tube sealant was completely vaporized by the hot model tube coolant at a discharge power of 116 kW.

Several different potting materials were investigated, including polyimide resins (useful up to about 370°C) and ceramics (useful at 650°C and up). It was concluded that it might be possible to obtain sufficient sealing using one of these materials so that meaningful data could be obtained. However, there was not sufficient time to conduct these experiments due to several premature failures during testing of the water-cooled model.

One failure of the water-cooled model involved blackening of the transparent wall during plasma initiation. The auxiliary dc arc starter, operating in the combination mode, was used to start the plasma (see DESCRIPTION OF PRINCIPAL EQUIPMENT). The problem was caused by vaporization, due to rf heating, of teflon tape which was wrapped on the starter electrodes. This problem was eliminated by utilizing electrodes having ceramic sleeve insulators on the ends. Other model failures resulted from arcs between injectors during starting, and from an rf power shutdown (not related to these tests) at a discharge power of 94 kW and a chamber pressure of 16.6 atm. Both incidents resulted in substantial leakage of coolant from the axial tubes, preventing further testing at that time.

During an initial test series, a calibration of the radiometer used for the radiant energy measurements was obtained. At a constant total discharge power, the radiant energy escaping the model was virtually eliminated by increasing the amount of dye in the annular cooling water. The resulting increase in the power deposited in the annular cooling water was compared with the decrease in the radiometer output. The calibration constant for the radiometer determined in this manner compared very well (within 5 percent) with that obtained previously using a standard lamp.

## Discussion of Test Results

### Tests at High Power and High Pressure Operating Conditions

The highest total discharge power attained was 193 kW; the highest model chamber pressure attained was 35 atm; and the highest radiant heat flux on the transparent wall was about 1.4 kW/cm<sup>2</sup>. These maximum test conditions occurred simultaneously, and they are all about a factor of two greater than the levels in previous tests with a transparent-wall model.

Figure 49 shows the energy balance for the highest-power/highest-pressure operating condition. The total dc input power was approximately 590 kW and, since the total discharge power was 193 kW, the coupling efficiency was 0.33. Table II presents detailed information for the highest-power/highest-pressure test condition; it also lists the corresponding values for the reference engine, and for an in-reactor test cell in the Nuclear Furnace.

An attempt to increase the total discharge power and chamber pressure above 193 kW and 35 atm resulted in an arc inside the 1.2-MW test tank, causing plasma extinguishment and cracking of some of the axial tubes. The allowable hoop and thermal stresses in the fused silica concentric tubes used as pressure vessels in the model would have limited chamber pressure to approximately 42 atm if arcing had not occurred. The power would have been well over 200 kW at 42 atm with this model. This level might be reached in future tests by judicious adjustment of the flow parameters to increase the rf coupling efficiency, and by increasing the amount of SF<sub>6</sub> in the test tank to reduce the possibility of arcing at high resonator voltages.

#### Breakdown of Power Radiated and Power Deposited in Model Components

Figures 50 through 53 provide additional information on the power radiated and deposited in various model components over the complete range of test conditions. In all the plots, a dashed line indicates a constant fraction of the total discharge power which was radiated or deposited. The solid data points are from FY 1971 (Ref. 16) and are shown for comparison.

In Fig. 50, the variation of power radiated through the transparent wall with total discharge power is shown. These data are conservative since the data are not corrected for the radiated power absorbed directly by the cooling water in the model tubes, by the peripheral-wall injectors, or by the end walls. The power radiated was significantly greater in the present tests than in the previous tests reported in Ref. 16. However, the fraction of power radiated through the model walls appears to be slightly less than in previous tests --- about 0.4, compared with 0.5. This was a general characteristic of most tests in this program. There was a noticeable decrease in the transparency of the model walls due to deposits which accumulated during the longer run times in the present program. Most of this loss in transparency was probably caused by leakage of axial tube coolant water at the end sealant; the water then vaporized on the hot tubes, leaving a semi-transparent residue.

The amount of power deposited in the model coolant tubes, shown by the open symbols in Fig. 51, was generally greater than that in previous tests (about 35 percent vs 20 percent). This would be expected if there indeed was a loss in transparency as discussed above. Although the fraction of power deposited is considerably greater than desirable for a reference engine design, the present data indicate that a transparent wall can be adequately cooled, even when the heat load is relatively high (1.5 kW/cm<sup>2</sup>). As noted in Ref. 16, approximately 10 percent of the total discharge power is deposited in the water coolant by direct absorption of radiation.

Figure 52 shows the power deposited in the injectors. In the present tests, as in the past tests, the power deposited was consistently about 10 percent of the total discharge power. From the data of Table II, and using the procedure described in Ref. 16, it was estimated that the peripheral-wall injectors again reflected 15 to 25 percent of the incident radiation.

Figure 53 shows the variation of power deposited in the end walls and thru-flow exhausts with total discharge power. These data are also consistent with those from previous tests. It is desirable to reduce the fraction of power deposited to as low a value as possible. The data at high total power levels show a favorable trend --- decreasing to about 20 percent. This indicates that the fraction of radiated power was increasing, as expected, due to the increase in chamber pressure that accompanied the increase in total power.

Figure 54 shows the variation with chamber pressure of the fraction of total discharge power radiated through the transparent wall. These data are low compared with the total radiation from the plasma because they do not include the radiant energy absorbed directly by the model cooling water, by the peripheral-wall injectors, or by the end walls. The fraction of the power radiated through the wall reached a maximum of about 50 percent.

If it is assumed that the energy deposited in the transparent wall and injectors is all radiant energy and can be added to the energy radiated through the transparent wall, the values of the fraction of total discharge power that is radiated for pressures above 19 atm are as shown by the data points in the box in Fig. 54. These values show the trend expected; i.e., the values increase slightly with increasing pressure, and they correspond very well with data from tests with models that did not have a transparent wall (see Figs. 17 and 25). This assumption is reasonable in that the amount of energy radiated to the end walls (which is not included) compensates somewhat for the amount of energy deposited in the transparent wall and injectors by convection (which is included). These values of the fraction of total power radiated are independent of any decrease in wall transparency, which was discussed previously.

#### Summary of Key Results and Comparison with Reference Engine and In-Reactor Unit Cell Conditions

The primary objectives in the present program were to test transparent-wall models to the highest possible discharge power at pressures greater than 20 atm using axial coolant tubes with wall thicknesses down to approximately 0.125 mm. In obtaining high discharge powers it is important to maximize the radiant energy flux from the fuel region and to minimize the total heat deposited in the transparent wall. The direct-on spectral measurements of an argon plasma discussed in Ref. 15 have shown that there is very little radiation in the uv portion of the spectrum



below the lower cutoff of fused silica. Thus, with a completely clean transparent wall (and a gas coolant), virtually all of the heat deposited in the wall would be due to conduction and convection.

Values of several key parameters pertinent to the transparent wall are listed in Table II for the reference engine, for the in-reactor test configuration, for the present program, and for previous tests. In the present program, the highest total discharge power obtained was 193 kW and the maximum chamber pressure was 35 atm. For the highest power test, the radiant heat flux incident on the transparent wall was about 1.4 kW/cm<sup>2</sup>. This compares with 23.4 kW/cm<sup>2</sup> for the reference engine. It is presently estimated that the in-reactor unit cell will have a radiant heat flux of 0.40 to 0.76 kW/cm<sup>2</sup> at the reflective aluminum wall. The radiant heat flux in these tests is difficult to determine since the radiant energy absorbed by the transparent wall cannot be precisely separated from the convected energy. For the present tests, the energy convected to the wall was estimated using the same method used in Ref. 16. In general, about 10 percent of the power deposited in the transparent-wall model was due to convection.

The maximum chamber pressure in these tests was limited by the allowable hoop and thermal stresses in the fused-silica tubes used as the model pressure vessel. To make substantial model operating pressure increases would require the use of a stronger pressure vessel which would require extensive modifications to the model. These modifications might include the use of a filament-wound pressure vessel in future tests. The maximum total discharge power was limited by the available time for repair and testing of the model after arcing in the resonator section caused extinguishment of the plasma and axial coolant tube failure at the 193 kW power level. It is recommended that future work with transparent-wall models be directed toward improvement in the fabrication and installation of transparent walls such that gas cooling could be utilized at high power and pressure.

## REFERENCES

1. McLafferty, G. H. and H. E. Bauer: Studies of Specific Nuclear Light Bulb and Open-Cycle Vortex-Stabilized Gaseous Nuclear Rocket Engines. United Aircraft Research Laboratories Report F-910093-37, prepared under Contract NASw-847, September 1967. Also issued as NASA CR-1030.
2. Clark, J. W., B. V. Johnson, J. S. Kendall, A. E. Mensing and A. Travers: Summary of Gaseous Nuclear Rocket Fluid Mechanics Research Conducted Under Contract NASw-847. United Aircraft Research Laboratories Report F-910091-13, May 1967. Also J. Spacecraft Rockets, vol. 5, no. 8, August 1968.
3. McLafferty, G. H.: Survey of Advanced Concepts in Nuclear Propulsion. J. Spacecraft Rockets, vol. 5, no. 10, October 1968.
4. McLafferty, G. H.: Investigation of Gaseous Nuclear Rocket Technology -- Summary Technical Report. United Aircraft Research Laboratories Report H-910093-46, prepared under Contract NASw-847, November 1969.
5. Bauer, H. E., R. J. Rodgers and T. S. Latham: Analytical Studies of Start-Up and Dynamic Response Characteristics of the Nuclear Light Bulb Engine. United Aircraft Research Laboratories Report J-910900-5, prepared under Contract SNPC-70, September 1970. Also issued as NASA CR-111097.
6. Latham, T. S. and R. J. Rodgers: Analytical Design and Performance Studies of Nuclear Furnace Tests of Small Nuclear Light Bulb Models. United Aircraft Research Laboratories Report L-910900-17, prepared under Contract SNPC-70, September 1972.
7. Latham, T. S.: Summary of the Performance Characteristics of the Nuclear Light Bulb Engine. AIAA Paper No. 71-642, presented at the AIAA Seventh Propulsion Joint Specialist Conference, Salt Lake City, Utah, June 14-18, 1971.
8. Kendall, J. S. and R. C. Stoeffler: Conceptual Design Studies and Experiments Related to Cavity Exhaust Systems for Nuclear Light Bulb Configurations. United Aircraft Research Laboratories Report L-910900-15, prepared under Contract SNPC-70, September 1972.
9. Klein, J. F.: Nuclear Light Bulb Propellant Heating Simulation Using a Tungsten-Particle/Argon Aerosol and Radiation from a DC Arc Surrounded by a Segmented Mirror Cavity. United Aircraft Research Laboratories Report L-910900-13, prepared under Contract SNPC-70, September 1972.

## REFERENCES (Continued)

10. Rodgers, R. J. and T. S. Latham: Analytical Design and Performance Studies of the Nuclear Light Bulb Engine. United Aircraft Research Laboratories Report L-910900-16, prepared under Contract SNPC-70, September 1972.
11. Jaminet, J. F.: Development of a Model and Test Equipment for Cold-Flow Tests at 500 Atm of Small Nuclear Light Bulb Configurations. United Aircraft Research Laboratories Report L-910900-14, prepared under Contract SNPC-70, September 1972.
12. Palma, G. E.: Measurements of the UV and VUV Transmission of Optical Materials During High-Energy Electron Irradiation. United Aircraft Research Laboratories Report L-990929-3, prepared under Contract SNPC-70, September 1972.
13. Krascella, N. L.: Spectral Absorption Coefficients of Argon and Silicon and Spectral Reflectivity of Aluminum. United Aircraft Research Laboratories Report L-910904-3, prepared under Contract SNPC-70, September 1972.
14. Roman, W. C., J. F. Klein and P. G. Vogt: Experimental Investigations to Simulate the Thermal Environment, Transparent Walls, and Propellant Heating in a Nuclear Light Bulb Engine. United Aircraft Research Laboratories Report H-910091-19, prepared under Contract NASw-847, September 1969.
15. Roman, W. C.: Experimental Investigation of a High-Intensity R-F Radiant Energy Source to Simulate the Thermal Environment in a Nuclear Light Bulb Engine. United Aircraft Research Laboratories Report J-910900-4, prepared under Contract SNPC-70, September 1970. Also issued as NASA CR-110909.
16. Roman, W. C. and J. F. Jaminet: Experimental Investigations to Simulate the Thermal Environment and Fuel Region in Nuclear Light Bulb Reactors using an R-F Radiant Energy Source. United Aircraft Research Laboratories Report K-910900-7, prepared under Contract SNPC-70, September 1971.
17. Latham, T. S. and H. E. Bauer: Analytical Design Studies of In-Reactor Tests of a Nuclear Light Bulb Unit Cell. United Aircraft Research Laboratories Report K-910900-11, prepared under Contract SNPC-70, September 1971.
18. Anon.: International Critical Tables, vol. V. McGraw-Hill Book Co., Inc., New York, 1930.

## REFERENCES (Continued)

19. Goldfarb, V. M. and S. V. Dresvin: Optical Investigation of the Distribution of Temperature and Electron Density in an Argon Plasma. Soviet Physics, High Temperature Physics (Translation), vol. 3, 1965, p. 303.
20. Scholz, P. D. and T. P. Anderson: Local Thermodynamic Equilibrium in an RF Argon Plasma. J. Quant. Spect. and Rad. Tran., vol. 8, 1968, p. 1411.
21. Mensing, A. E. and J. F. Jaminet: Experimental Investigation of Heavy-Gas Containment in R-F Heated and Unheated Two-Component Vortexes. United Aircraft Research Laboratories Report H-910091-20, prepared under Contract NASw-847, September 1969.
22. Jaminet, J. F. and A. E. Mensing: Experimental Investigations of Simulated Fuel Containment in R-F Heated and Unheated Two-Component Vortexes. United Aircraft Research Laboratories Report J-910900-2, prepared under Contract SNPC-70, September 1970. Also issued as NASA CR-111101.
23. Mensing, A. E. and L. R. Boedeker: Theoretical Investigation of R-F Induction Heated Plasmas. United Aircraft Research Laboratories Report G-910091-18, prepared under Contract NASw-847, September 1968. Also issued as NASA CR-1312.
24. Mensing, A. E. and J. S. Kendall: Experimental Investigation of Containment of a Heavy Gas in a Jet-Driven Light-Gas Vortex. United Aircraft Research Laboratories Report D-910091-4, prepared under Contract NASw-847, March 1965.
25. Kendall, J. S., A. E. Mensing and B. V. Johnson: Containment Experiments in Vortex Tubes with Radial Outflow and Large Superimposed Axial Flows. United Aircraft Research Laboratories Report F-910091-12, prepared under Contract NASw-847, May 1967. Also issued as NASA CR-993.
26. Kinsman, S.: Radiological Health Handbook. U. S. Department of Health, Education and Welfare Publication PB 121784, January 1957.
27. Vogt, P. G.: Development and Tests of Small Fused Silica Models of Transparent Walls for the Nuclear Light Bulb Engine. United Aircraft Research Laboratories Report J-910900-3, prepared under Contract SNPC-70, September 1970.
28. McLafferty, G. H.: Studies of Coolant Requirements for the Transparent Walls of a Nuclear Light Bulb Engine. United Aircraft Research Laboratories Report F-110224-6, March 1967.

REFERENCES (Continued)

29. Ballman, A. A., et al.: Synthetic Quartz with High Ultraviolet Transmission. Appl. Opt., vol. 7, no. 7, July 1968.
30. Katz, J. J. and E. Rabinowitch: The Chemistry of Uranium, Part 4 - Uranium Halides and Related Compounds. McGraw-Hill Book Co., Inc., New York, 1951.

## LIST OF SYMBOLS

$A_M$	Wall surface area of transparent-wall model, $\text{cm}^2$
$A_S$	Plasma discharge surface area, $\text{cm}^2$
$C$	Concentration, ppm
$d$	Plasma discharge diameter at axial midplane, cm
$D$	Diameter of unit cavity, test section or transparent-wall model, cm or m
$E_\gamma$	Gamma-ray energy, keV
$f$	Frequency, MHz
$I_\lambda$	Monochromatic intensity, $\text{kW}/\text{cm}^2\text{-sr}$
$I_{0,\lambda}$	Incident monochromatic intensity, $\text{kW}/\text{cm}^2\text{-sr}$
$(I/I_0)$	Fraction of gamma photons transmitted to detector from source, dimensionless
$I_\lambda/I_{0,\lambda}$	Internal transmittance, dimensionless
$(I/I_0)_{\Delta\lambda}$	Fraction of total radiation transmitted in wavelength band $\Delta\lambda$ , dimensionless
$L$	Length of unit cavity, test section or transparent-wall model, cm or m
$P$	Total pressure, atm
$P_D$	Chamber pressure, atm
$Q_C$	Power deposited into model tubes and coolant, kW
$Q_E$	Power deposited in end-wall cooling water, kW
$Q_I$	Total dc input power to rf induction heater, kW
$Q_J$	Power deposited in model peripheral-wall vortex injectors, kW

## LIST OF SYMBOLS (Continued)

$Q_L$	Power deposited in thru-flow heat exchangers, kW
$Q_L'$	Power convected out the exhaust ducts downstream of heat exchangers, kW
$Q_P$	Power deposited in simulated-fuel injection probes, kW
$Q_R$	Radiated power escaping test chamber as measured by radiometer, kW
$Q_T$	Total discharge power, kW
$Q_W$	Power deposited in peripheral-wall coolant by combined conduction, convection and radiation, kW
$Q_{R,T}$	Total radiated power transmitted through the inner peripheral wall, $Q_R + Q_W - Q_C$ , kW
$Re_{t,j}$	Injection Reynolds number based on average inlet jet velocity, dimensionless
$r$	Local radius from center of chamber or discharge radius, cm
$r_1$	Radius of peripheral wall (cavity wall), cm
$r_0$	Radius of edge of plasma discharge or fuel cloud, cm
$T$	Temperature, $^{\circ}K$
$T^*$	Equivalent black-body radiating temperature, $^{\circ}K$
$t$	Time, sec
$V$	Volume, $cm^3$ or velocity, m/sec
$V_1$	Buffer-gas velocity at the peripheral wall, m/sec
$V_j$	Average buffer-gas injection velocity, m/sec
$V_F$	Simulated-fuel injection velocity, m/sec
$\mathcal{W}$	Amount of simulated fuel, g

## LIST OF SYMBOLS (Continued)

$W_A$	Argon weight flow rate, g/sec
$W_F$	Simulated-fuel injection weight flow rate, g/sec
$W_W$	Tungsten weight flow rate, g/sec
$Z_P$	Reflected plasma impedance, ohm
$\Delta\lambda$	Wavelength band, microns
$\Delta l$	Path length for gamma photons from source to detector, cm
$\eta$	RF system coupling efficiency, $Q_T/Q_I$ , dimensionless
$\lambda$	Wavelength, microns or angstroms
$\mu$	Total gamma photon absorption coefficient, $\text{cm}^{-1}$
$\rho_{B_0}$	Density of buffer gas at edge of fuel, $\text{g}/\text{cm}^3$
$\bar{\rho}_F$	Average density of simulated fuel, $\text{g}/\text{cm}^3$



## APPENDIX A

## SUPPORTING RESEARCH WITH TUNGSTEN PARTICLES AND PARTICLE FEEDER SYSTEMS

This appendix describes development and supporting tests related to tungsten particle simulated-fuel injection technology. Future tests using the 1.2-MW rf induction heater with filament-wound pressure vessels will require a particle feeder system capable of injecting micron-sized simulated-fuel (uranium) particles into a high-pressure (500 atm) environment. The prime requirements are to inject the particles in a steady, controlled, and reproducible manner through simulated-fuel injection probes located in the test chamber. The particles must be injected in sufficiently high concentrations to provide the required fuel containment conditions.

The worm-screw feed technique, used in the FY 1971 preliminary particulate simulated-fuel injection tests, did not meet the requirement of providing a steady, reproducible flow of seed material. Random pulsations occurred throughout the cold- and hot-flow tests which adversely affected the plasma behavior. Follow-on tests with this feeder system resulted in no significant improvement in its performance.

The new and improved particle feeder system developed and tested in the present program was evolved after a series of exploratory tests were conducted using several types of particle feeder systems. The following discussion relates the pertinent results of these supporting exploratory tests.

The first system tested employed a modified "Wright" dust feed aerosol type generator. In this device, a scraper head principle is employed which permits a gradual scraping off of a prepacked seed material from within a cylindrical canister. The seed material is then entrained and carried away by the carrier gas flowing over the scraper head. The distinct advantage of this type of aerosol generator is in the positive entrainment of seed material into the carrier gas at relatively low flow rates. Results of tests using this feeder system indicated unsteady flow and intermittent clogging. Much of the tungsten powder was discharged in the form of large agglomerates. It was concluded that this device would be unsuitable for providing uniformly dispersed micron-sized tungsten particles at the pressures and flow rates required in the simulated-fuel injection tests without an extensive development program.

The second particle feeder system employed a horizontal, rotating drum device containing a series of small diameter (ranging from 0.16 to 0.64-cm diam) radial metering holes equally spaced on the circumference of a 7.5-cm-i.d. cylinder. This device utilized a carrier gas to provide a positive purge of the tungsten particles (non-prepacked form) from the metering holes, i.e., small quantities of tungsten powder fill the holes in the cylinder and are then carried around to an outlet port

where the argon carrier gas positively expels the tungsten out of the device into a surrounding manifold. Lucite windows at the ends of the cylinder permitted observation of the tumbling action of the tungsten powder as the cylinder rotated. With a smooth polished surface on the inside of the steel cylinder, and no predrying of the tungsten powder, rotational speeds of approximately 2 rad/sec permitted even the smallest holes to fill with the tungsten powder and reproducibly expel the small slug of tungsten powder. Based on these exploratory tests, a preliminary design of a high-pressure tungsten powder rotating cylinder feed device was completed. The feeder system was designed to fit within an existing 200-atm, high-pressure, stainless-steel canister. The design of this system also has the capability of being extended in operation to 500 atm. Considerable fabrication, development and testing would be required to bring this system to an acceptable operating status. Thus, in view of the favorable results of the third particle feeder system discussed in the following paragraph, no additional development or fabrication of the rotating drum concept occurred in the present program.

The third particle feeder system investigated was a commercially available Roto-Feed hopper system (Model 1000 A) manufactured by Geotel, Inc. This feeder operates on a volumetric feed principle; the capacity is proportional to the specific gravity of the seed material used. For reference, the density of tungsten is  $19 \text{ g/cm}^3$  compared with carbon at  $2.3 \text{ g/cm}^3$ ; carbon was also successfully dispersed in earlier tests. The feeder was originally developed for plasma spray work to provide a positive feed at repeatable rates for powders ranging in size from about 10 to  $100 \mu$  in diameter.

A schematic diagram of the basic particle feeder system is shown in Fig. 27. The particles are loaded into a cylindrical canister having a volume of approximately  $2500 \text{ cm}^3$ . A variable-speed motor drives a perforated wheel located at the base of the canister. The particles enter the perforations and are carried by the wheel to an azimuthal exit port where they are discharged. A cam-driven tamper assembly (not shown in Fig. 27) was also tried to aid in loading the powder into the rotary wheel. The tamper assembly adversely affected the behavior of the particle loading process when using tungsten seeds and consequently was not employed in any of the tests reported herein. In some tests, various types of deagglomerators were located downstream of the canister to prevent the seed material leaving the canister from reagglomerating and also to act as a pulsation damper. A deagglomerator incorporating a tangential inlet and a conical annulus provided the best results and was used in all the follow-on tests.

Figure 27 shows the basic test setup used in the cold-flow exploratory tests. A ball valve located downstream of the deagglomerator allows the seeded stream to be directed into either the simulated-fuel injection probes or the seed collection system. With this arrangement, the seeds can be passed through the simulated-fuel injection probes to determine the steadiness and controllability by directing the

stream of seeds onto a rapidly moving sheet of recorder paper. Alternately, the seed flow can be directed into the seed collector to permit measurement of the time-averaged seed mass flow rate. The seed collector consists of a foam collector and balance system.

Preliminary cold-flow tests were conducted using the as-received particle feeder system. The configuration was similar to that shown in Fig. 27, except no deagglomerator was employed. Initial results indicated an unsteady flow of the seeded stream. Changing the gear ratio in the motor drive unit, thereby increasing the rotational speed of the rotary wheel by a factor of three, helped in smoothing out the very distinct periodic pulsations originally observed. At the same time, additional modifications and improvements were incorporated into the system in an attempt to provide the steady and controlled flow required for the rf plasma tests. These included modifications to the lines, fittings, couplings, and valves to permit a smooth transition and flow path for the particle-gas mixture. Various types of material were also used for the connecting transfer lines between the feeder system and the simulated-fuel injection probes; included was copper, stainless steel, nyloflow tubing, and surgical rubber tubing. Various size transfer lines were tried in an attempt to find the size which permitted the best seed flow over the test conditions of interest. Throughout most of the tests, approximately 100 g of tungsten powder was loaded into the canister. However, in several tests as little as 20 g and as much as 300 g were also tried. The test results indicated 100 g was the most acceptable quantity to use. Copper transfer lines also appeared to be as good as any of the alternate line materials tried. Inclusion of a deagglomerator significantly improved the steadiness of the flow.

Switching to a different source for tungsten particles also showed improvement in the steadiness of the seed flow. The original batch of tungsten particles was obtained from Shield Alloy Corporation and had a nominal diameter of 1 to 10  $\mu$ . The new batch of tungsten particles was obtained from Union Carbide Corporation and was designated submicron in size. Visual observation and handling of this new tungsten powder seemed to indicate a more homogeneous powder than that from the previous source. No apparent clumping was noted in the pressure canister during the loading procedure. Figures 55 and 56 are electron photomicrographs of these tungsten particles as collected on a small grid after discharge from the particle feeder system. The circular collector grid was 3 mm in diameter. The reference 1- $\mu$  dimension is shown in the lower right-hand corner of the figure. The magnification for Fig. 55 was  $9.6 \times 10^2$ . To better illustrate the chain-like structure of several of the agglomerates, Fig. 56 is an enlargement of the dashed area shown in Fig. 55; the magnification was increased to  $6.3 \times 10^3$ . Analysis of several samples indicated the Union Carbide tungsten powder had a nominal diameter of approximately 0.1  $\mu$ .

In summary, it is believed the use of the deagglomerator together with the 0.1- $\mu$  nominal diameter tungsten powder were the two primary contributors to significantly improving the behavior and operation of the feeder system. In addition, carefully selecting the line sizes compatible with the desired flow conditions and streamlining all the valves, fittings, junctions, etc., also aid in providing a steady and reproducible stream of seeds.

## APPENDIX B

## RADIATION CHARACTERISTICS AND PROPERTIES OF NIGROSINE DYE

This appendix describes supporting tests related to the nigrosine dye used in the test chamber annular water coolant during the rf plasma tests. Prior tests (Ref. 14) were conducted with different dyes and pigments to determine the type with the most desirable spectral absorption characteristics. Nigrosine dye (an organic, water-soluble dye with a color index of 50420) was selected over several other candidates. In addition to possessing good radiation attenuation characteristics, the dye was easy to handle, readily dissolved into the annular cooling water, and left no residue on the fused silica tubes after flushing. Many of the other dyes and pigments tested left a residue on the tubes after use which was not easily removed by back-flushing.

Figure 57 summarizes the water-nigrosine dye coolant radiation attenuation characteristics. Figure 57(a) shows a direct comparison of the relative radiated power transmitted through the dye in several wavelength bands. A standard lamp was used as the source in these comparison tests. The bar graph on the left in Fig. 57(a) shows the spectral absorption characteristics of the standard lamp over four wavelength bands between 0.25 and 1.3  $\mu$  as measured by the radiometer. The bar graph on the right presents the results obtained when 740 ppm of nigrosine dye was dissolved in the water coolant. The path length for this case was 2 mm. (Note the difference in ordinate scales.) The majority of the absorption occurred in the 0.25-to-0.72- $\mu$  wavelength band. Separate tests were conducted to verify that the absorption characteristics of the water coolant with a range of concentrations of nigrosine dye added (up to  $10^4$ ) were not influenced by the radiation from the plasma source or by the bulk temperature of the annular coolant for the range of test conditions reported. The majority of these tests were conducted using the test configuration shown in Fig. 11. The rf plasma source was operated at moderately high power and pressure levels, but no simulated fuel was injected in any of the tests. Other tests were conducted to determine that the water-nigrosine dye mixture did not absorb significant amounts of rf energy; this would lead to errors in the energy balance calculations (primarily in the filament-wound pressure vessel tests where all the radiation was absorbed by the water-dye coolant). All these tests were conducted using the 1.2-MW rf induction heater.

Figure 57(b) shows experimental results of the effect of the nigrosine dye concentration on the radiation attenuation in the water-dye coolant. The data for this curve were obtained using the configuration shown in Fig. 10(b). The path length was 2 mm (annular gap between the fused silica tube peripheral walls) and the radiometer measured the total radiation over the 0.25-to-1.3- $\mu$  wavelength band. The annular water was maintained at approximately 32°C. The solubility of

nigrosine dye in tap water is approximately 1 g/g at about 80°C. At dye concentrations of 10<sup>4</sup> ppm (on a weight basis), less than 1 percent of the total incident radiation was transmitted through the water-dye coolant. These tests verified the ability to attenuate greater than 99 percent of the incident radiation. This was an important requirement in the high-pressure/high-power rf plasma IRG configuration tests employing a filament-wound pressure vessel as the outer peripheral wall.

Additional supporting tests using nigrosine dye were not anticipated until the dye coating phenomena reported in the SIMULATED-FUEL INJECTION RESEARCH section of this report was first observed. After completion of several of the high-power, high-pressure simulated-fuel injection tests, inspection of the disassembled configuration revealed a dark coating on the outside wall of the 57-mm fused silica tube (see Fig. 41). The coating was generally heaviest near the axial midplane of the tube. At no time was any coating observed on the inside surface of the outermost fused silica tube (also in contact with the water-dye mixture). The coating could not be removed by back-flushing the cooling system, but required scrubbing with a detergent. Analysis of the coating material using an infrared spectrophotometer revealed the deposit contained some dye, but not as the major constituent. The deposit was carbon-like with some absorbed dye. One possible explanation is uv deterioration of the dye.

In general, during the tungsten simulated-fuel injection tests, a decrease in the amount of radiation (mostly from argon) in the infrared portion of the spectrum was noted. However, an increase was also noted in the fraction of the total power deposited into the plasma that was radiated through the inner peripheral wall. A significant part of this was the increase in the power deposited into the annular water-dye coolant. Part of this increase in power deposited in the water-dye coolant occurs because the spectral absorbance of the nigrosine dye is such that strong absorption bands occur at 0.203, 0.297, and 0.580 $\mu$ . Figure 58 illustrates the spectral absorbance measured using the nigrosine dye crystals (concentration 16 mg/l) dissolved in water. For this test, the path length was 1 cm.

It appears that uv deterioration of the dye is one possible explanation for the observed coating. Another possibility is that there may be traces of highly dispersed impurities present in the water-soluble nigrosine dye which could be initiating deposits on the tube surface due to electric field effects. Alternate sources of nigrosine dye were investigated and several samples received; however, the time schedule did not permit additional tests to be completed. Because of the importance of this aspect relative to future simulated-fuel injection tests, further investigation, including experiments with various types of dye and/or doped dye mixtures exposed to calibrated strong uv sources, should be conducted to determine the best dye to use within the operating conditions expected in future tests.

TABLE I  
SUMMARY OF TEST CONFIGURATIONS, TYPE OF TESTS, AND LOCATION  
OF DATA DISCUSSED IN TEXT

Numbers Refer to Figure Numbers

Type of Test	Type of Pressure Vessel	Configuration	Photograph of Configuration	Type of Simulated-Fuel Injection Probes Used	Power Breakdown	Data					
						Variation In Radiated Power and Flux	Radiation Efficiency	Spectral Emission	Operating Conditions	Test Photographs	
Radiant Energy Source Research	Fused Silica Tube	3, 10, 34	11	3 - Concentric Tube	9, 13	15, 16, 19	17	18	12, 26 Table II	14	
				4 - Concentric Tube							
Simulated-Fuel Injection Research	Filament-Wound Tube	3, 20	21	None Present	23	24	27		26 Table II	22	
Tungsten (W)	Fused Silica Tube	10	31	3 - Concentric Tube			Table V	32, 33	Table V	31	
				4 - Concentric Tube							
Uranium Hexafluoride (UF <sub>6</sub> )	Fused Silica Tube	34	39	4 - Concentric Tube		38	Table VI	38	Table VI	39	
High-Pressure Particle Feeder System Research	Fused Silica Tube	27	28	3 - Concentric Tube					Table III Table IV	29, 30	
				4 - Concentric Tube							
Transparent-Wall Model Research	Fused Silica Tube	3, 46, 47	48	None Present	49	50	54		Table II		

TABLE II

COMPARISON OF OPERATING CONDITIONS IN FULL-SCALE ENGINE AND IN-REACTOR GEOMETRY WITH RF PLASMA SOURCE AND MODEL TESTS AT HIGHEST-POWER/HIGHEST-PRESSURE LEVEL

	Unit Cavity Of Full-Scale Reference Engine <sup>a</sup>	Reference In-React Test Configuration <sup>b</sup>	Transparent-Wall Model		7/8-Scale IRG RF Plasma Configuration	
			Present Program	Previous Program (Ref. 16)	Fused Silica Tube Pressure Vessel	Filament-Wound Tube Pressure Vessel
			Highest-Power/Highest-Pressure Case	Highest-Power Case	Highest-Power/Highest-Pressure Case	Highest-Power/Highest-Pressure Case
Transparent-Wall-Configuration						
Inside Diameter, cm	Circumferential	Axial	Axial	Axial	Axial	Axial
Length Between Containing End Walls, cm	48.9	6.6	3.25	5.7	5.7	5.7
Length/Diameter Ratio	182.9	17.78	10.2	15.5	15.5	15.5
Number of Coolant Tubes	3.75	2.7	3.1	2.7	2.7	2.7
Tube Inside Diameter, cm	3000	1e	60	1	1	1
Tube Outside Diameter, cm	0.127	6.60	0.127	5.7	5.7	5.7
Tube Wall Thickness, cm	0.152	6.85	0.152	6.1	6.1	6.1
Total Tube Surface Area, cm <sup>2</sup>	0.013	0.125	0.013	0.2	0.2	0.2
Cylindrical Surface Area, cm <sup>2</sup>	88500	368.0	291.0	278.0	278.0	278.0
Coolant Fluid	28100	368.0 <sup>c</sup>	90.8	278.0	278.0	278.0
Buffer Fluid	Hydrogen	Argon	Air	Water	Water	Water
Buffer Injection Velocity, m/sec	Neon	Argon	Argon	Argon	Argon	Argon
Buffer Weight Flow, g/sec	7.6d	9.8	33.0	1.7	2.4	2.4
Chamber Pressure, atm abs	1340	39.7	16.4	8.6	11.8	11.8
Equiv. Black-Body Radiating Temp., °K	500	500	10.2	42	40	40
Radiant Heat Flux at Edge of Fuel, kW/cm <sup>2</sup>	8333	3333-3910	4250	4320	4400	4400
Heat Flux Incident on Transparent Wall, kW/cm <sup>2</sup>	27.6	0.67-1.27	1.75	1.9	2.1 Est.	2.1 Est.
Total	23.4	--	0.87	0.49	0.55	0.55
Due to Radiation	23.4	0.40-0.76 <sup>e</sup>	0.77	0.47 Est.	0.53 Est.	0.53 Est.
Heat From Fuel Region Deposited in Transparent Wall (Per Unit Area), kW/cm <sup>2</sup> c						
Total	0.528	--	0.076	--	--	--
Due to Radiation	0.234	0.40-0.76 <sup>e</sup>	0.042	--	--	--
Total Power in Fuel Region, kW	4.6 x 10 <sup>6</sup>	190-342	116	180	203	203

a Data obtained from Refs. 1 and 28.

b Data obtained from Ref. 6.

c Includes heat deposited directly in coolant fluid.

d Assumed value of  $V_1/V_j = 0.4$ .

e Reflective aluminum liner; no transparent wall.

f Plasma diameter estimated using gas-cooled model data from Ref. 16.



**TABLE III**  
**SUMMARY OF INITIAL COLD-FLOW TEST RESULTS USING MODIFIED TUNGSTEN PARTICLE FEEDER SYSTEM**  
**OPERATING AT 1 ATM WITH THREE DIFFERENT INJECTION PROBES**

ALL TESTS CONDUCTED USING SINGLE INJECTION PROBE

AVERAGE SIZE OF TUNGSTEN PARTICLES  $\approx$  0.1  $\mu$  DIAM

$$\text{MASS FRACTION} = \frac{\text{TUNGSTEN FLOW RATE}}{\text{ARGON FLOW RATE} + \text{TUNGSTEN FLOW RATE}}$$

PROBE I.D. - CM	0.08	0.168	0.232
ARGON FLOW RATE, (g/sec)	0.091 TO 0.345	0.313 TO 0.554	0.122 TO 0.681
ARGON INJECTION VELOCITY, (m/sec)	99 TO 324	77 TO 137	15.7 TO 87.3
TUNGSTEN FLOW RATE, (g/sec)	0.0575 TO 0.134	0.0575 TO 0.134	0.0575 TO 0.134
MOMENTUM, (kg-m/sec)	0.015 TO 0.155	0.028 TO 0.094	0.003 TO 0.071
DYNAMIC HEAD, (kg/m <sup>2</sup> )	1448 TO 13,700	636 TO 2111	33 TO 826
MASS FRACTION	0.28 TO 0.381	0.092 TO 0.299	0.076 TO 0.522

**TABLE IV**  
**SUMMARY OF COLD-FLOW TEST RESULTS USING HIGH-PRESSURE PARTICLE FEEDER SYSTEM UP TO 40 ATM WITH 0.1- $\mu$ -DIAM TUNGSTEN PARTICLES**

SIMULATED-FUEL INJECTION PROBE I.D. = 0.168 CM

$$\text{MASS FRACTION} = \frac{\text{TUNGSTEN FLOW RATE}}{\text{ARGON FLOW RATE} + \text{TUNGSTEN FLOW RATE}}$$

PRESSURE AT EXIT OF SIMULATED-FUEL INJECTION PROBE, ATM	1	10	20	30	40
ARGON FLOW RATE, (g/SEC)	0.313 TO 0.554	0.318 TO 0.794	0.431 TO 1.0215	1.090 TO 2.906	0.999 TO 3.021
ARGON INJECTION VELOCITY, m/sec	77 TO 137	3.9 TO 9.9	2.7 TO 6.4	4.7 TO 12.5	3.1 TO 9.4
TUNGSTEN FLOW RATE, (g/sec)	0.575 TO 0.134	0.0248 TO 0.134	0.0248 TO 0.134	0.0248 TO 0.134	0.0385 TO 0.134
MOMENTUM, (kg-m/sec)	0.028 TO 0.094	0.00014 TO 0.0088	0.0013 TO 0.0074	0.0052 TO 0.0370	0.0032 TO 0.0296
DYNAMIC HEAD, (kg/m <sup>2</sup> )	636 TO 2111	15 TO 100	15 TO 82	59 TO 417	34 TO 40
MASS FRACTION	0.094 TO 0.299	0.030 TO 0.297	0.036 TO 0.215	0.019 TO 0.109	0.012 TO 0.118

TABLE V  
TYPICAL RESULTS AND OPERATING CONDITIONS FOR RF PLASMA TESTS WITH TUNGSTEN SIMULATED-FUEL INJECTION

	Case I		Case II		Case III		Case IV		Case V	
	Without Fuel	With Fuel	Without Fuel	With Fuel	Without Fuel	With Fuel	Without Fuel	With Fuel	Without Fuel	With Fuel
<u>RF Plasma Operating Conditions</u>										
Operating Frequency, f-MHz	5.4005	5.4005	5.3992	5.3992	5.4053	5.4053	5.4048	5.4048	5.3998	5.3998
Power Deposited in Plasma, $Q_T$ -kW	32	47	44	53	96	111	77	91	115	73
Reflected Plasma Impedance, $Z_p$ -ohm	571	511	607	539	521	547	528	459	710	590
Fraction of Total Power Radiated Through Inner Peripheral Wall, $Q_R$ , $T/Q_T$	0.60	0.68	0.61	0.70	0.64	0.71	0.67	0.72	0.73	0.58
Equivalent Black-Body Radiating Temperature, $T^*$ -°K	2670	3000	2840	3020	3330	3580	3240	3410	3650	3100
<u>Buffer-Gas Vortex Flow Conditions</u>										
Argon Weight Flow, $W_A$ -g/sec	5.5	5.5	3.7	3.7	10.2	10.2	10.5	10.5	8.6	8.6
Buffer-Gas Vortex Injection Velocity, $V_j$ -m/sec	4.5	4.5	2.1	2.1	4.2	4.2	3.0	3.0	1.8	1.8
Injection Reynolds Number, $Re_{t,j}$ x $10^{-3}$	101.6	101.6	70.9	70.9	189.4	189.4	199.3	199.3	162.2	162.2
Chamber Pressure, $P_D$ -atm	10	10	15	15	20	20	30	30	40	40
<u>Simulated-Fuel Flow Conditions</u>										
Type of Probe	---	3-Concentric Tube	---	3-Concentric Tube	---	4-Concentric Tube	---	4-Concentric Tube	---	3-Concentric Tube
Simulated-Fuel Mass Fraction	---	0.02	---	0.02	---	0.04	---	0.06	---	0.04
Tungsten Injection Flow Rate, $W_W$ -g/sec	---	0.04	---	0.04	---	0.06	---	0.06	---	0.13
Simulated-Fuel Injection Velocity, $V_f$ -m/sec	---	25.0	---	16.6	---	31.0	---	14.0	---	11.0
Simulated-Fuel (Tungsten plus Carrier)-to-Buffer-Gas Weight Flow Ratio, $W_f/W_A$	---	0.36	---	0.55	---	0.14	---	0.10	---	0.39
Simulated-Fuel-to-Buffer-Gas Injection Velocity Ratio, $V_f/V_j$	---	5.6	---	7.9	---	7.4	---	4.7	---	6.1

TABLE VI

TYPICAL RESULTS AND OPERATING CONDITIONS FOR RF PLASMA TESTS WITH UF<sub>6</sub> SIMULATED-FUEL INJECTION

	Case I		Case II		Case III		Case IV		Case V	
	Without Fuel	With Fuel	Without Fuel	With Fuel	Without Fuel	With Fuel	Without Fuel	With Fuel	Without Fuel	With Fuel
<u>RF Plasma Operating Conditions</u>										
Operating Frequency, f-MHz	5.4042	5.4042	5.4038	5.4038	5.4047	5.4047	5.4063	5.4063	5.4052	5.4052
Power Deposited in Plasma, $Q_T$ -kW	45	67	79	127	46	84	101	153	123	161
Reflected Plasma Impedance, $Z_p$ -ohm	316	288	516	427	365	408	466	510	391	440
Fraction of Total Power Radiated Through Inner Peripheral Wall, $Q_R/T/Q_T$	0.43	0.67	0.57	0.73	0.62	0.77	0.66	0.79	0.72	0.78
Equivalent Black-Body Radiating Temperature, $T_w$ -°K	2510	3050	3200	3720	2800	3380	3450	3920	3680	3970
<u>Buffer-Gas Vortex Flow Conditions</u>										
Argon Weight Flow, $W_A$ -g/sec	2.7	2.7	7.7	7.7	6.5	6.5	9.1	9.1	7.0	7.0
Buffer-Gas Vortex Injection Velocity, $V_j$ -m/sec	5.7	4.6	6.4	6.4	2.6	2.6	2.5	2.5	1.5	1.5
Injection Reynolds Number, $Re_{t,j} \times 10^{-3}$	51.2	41.3	144.1	144.1	118.8	118.8	168.8	168.8	130.6	130.6
Chamber Pressure, $P_D$ -atm	4	5	10	10	20	20	30	30	40	40
<u>Simulated-Fuel Flow Conditions</u>										
Simulated-Fuel Concentration, Percent (By Partial Pressure)	---	1.0	---	0.5	---	1.0	---	1.0	---	1.0
Simulated-Fuel Injection Flow Rate, $W_F$ -g/sec	---	0.5 <sup>a</sup>	---	1.2	---	1.5	b	1.6	c	2.1
Simulated-Fuel Injection Velocity, $V_F$ -m/sec	---	13	---	52	---	32	---	23	---	23
Simulated-Fuel-to-Buffer-Gas Weight Flow Ratio, $W_F/W_A$	---	0.19	---	0.16	---	0.23	---	0.18	---	0.3
Simulated-Fuel-to-Buffer-Gas Injection Velocity Ratio, $V_F/V_j$	---	2.8	---	8.1	---	13.8	---	10.3	---	15.3

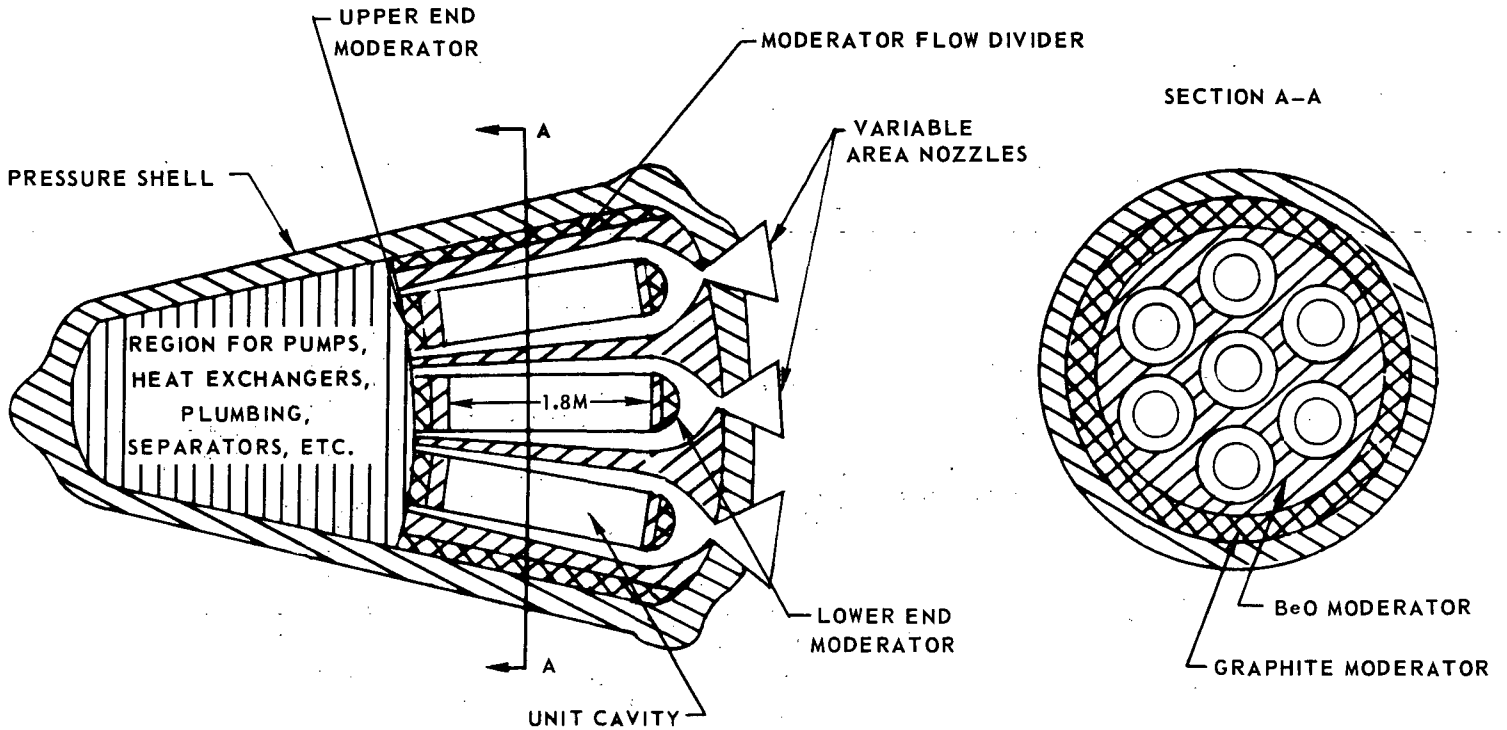
a 3-concentric-tube type simulated-fuel injection probes used.

b 0.2 g/sec argon carrier through probes.

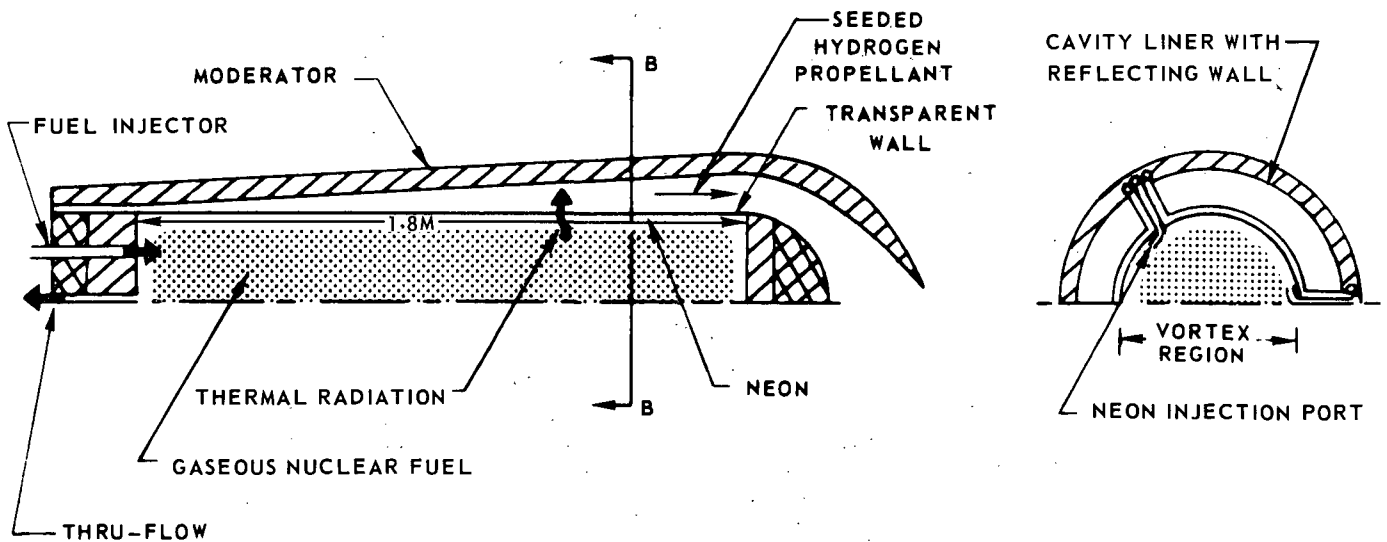
c 0.7 g/sec argon carrier through probes.

### SKETCHES ILLUSTRATING PRINCIPLE OF OPERATION OF NUCLEAR LIGHT BULB ENGINE

(a) OVERALL CONFIGURATION



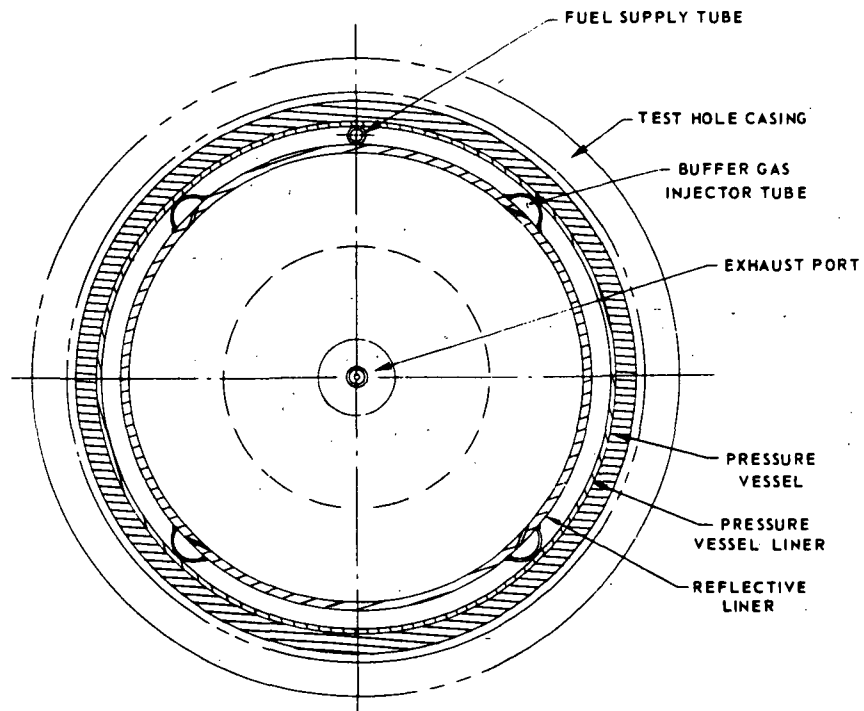
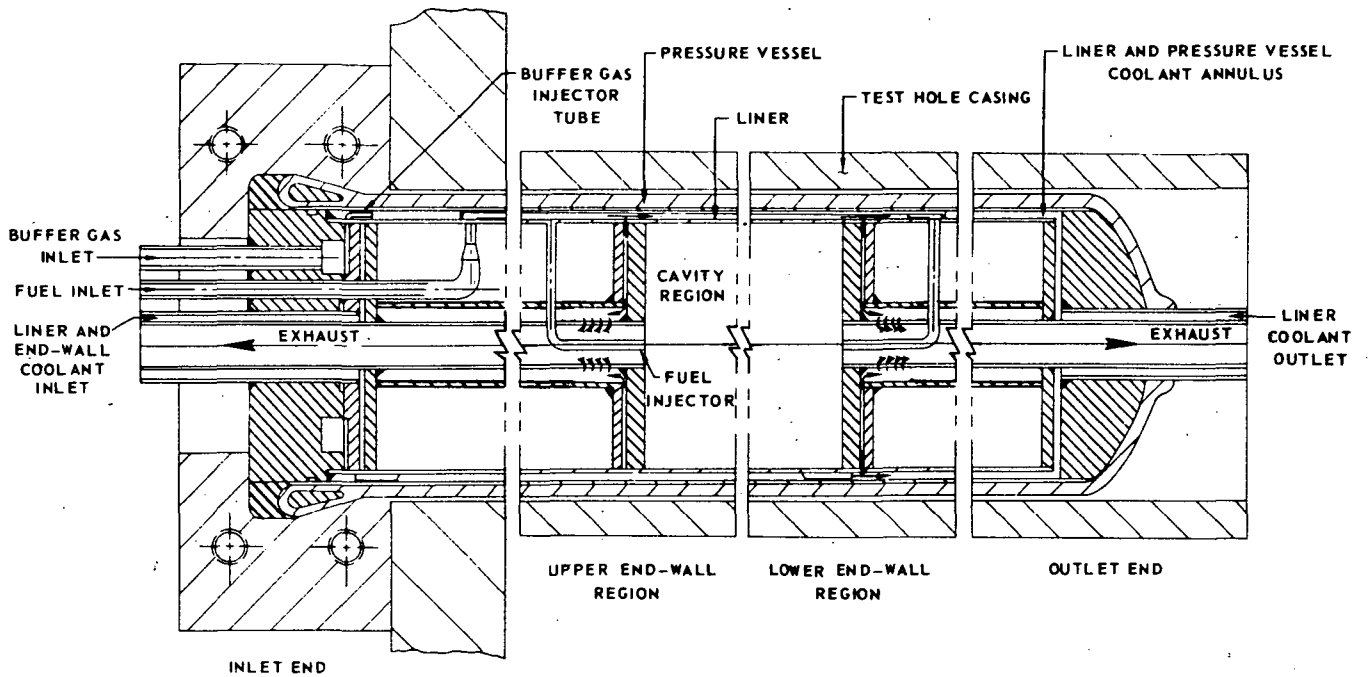
(b) CONFIGURATION OF UNIT CAVITY



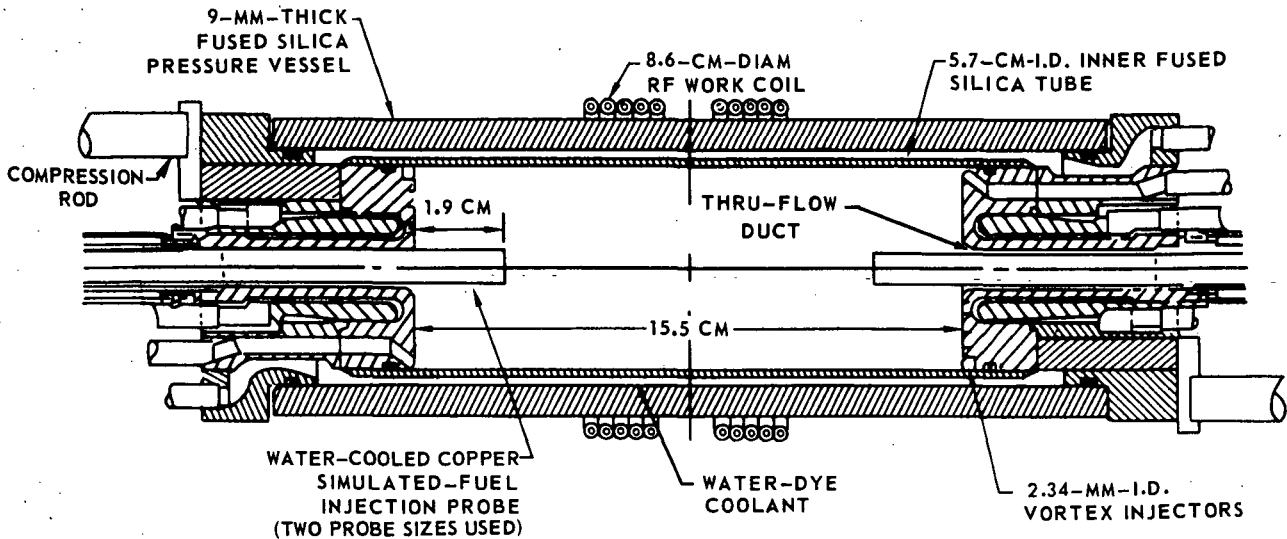
# PRELIMINARY LAYOUT OF TEST CELL FOR NUCLEAR FURNACE IN-REACTOR TEST

ID OF TEST HOLE CASING = 8.4 CM

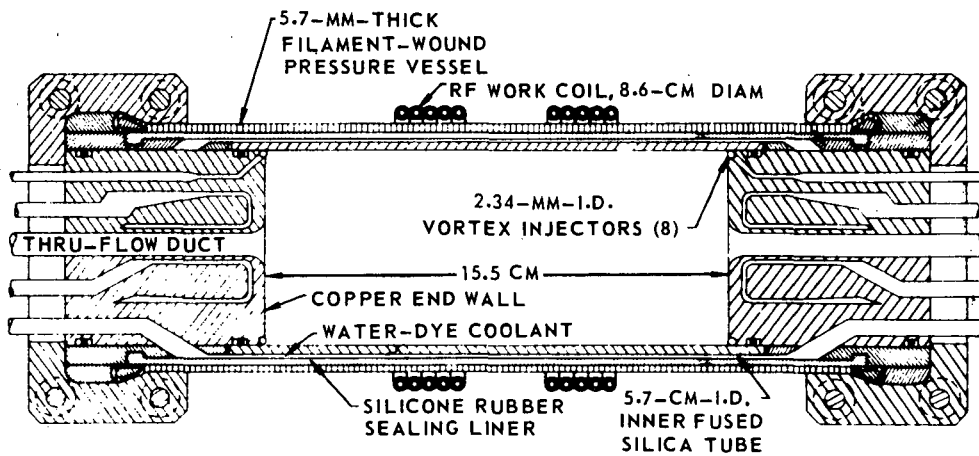
DIMENSIONS OF CYLINDRICAL CAVITY REGION: 6.6-CM I.D. X 17.8-CM LONG



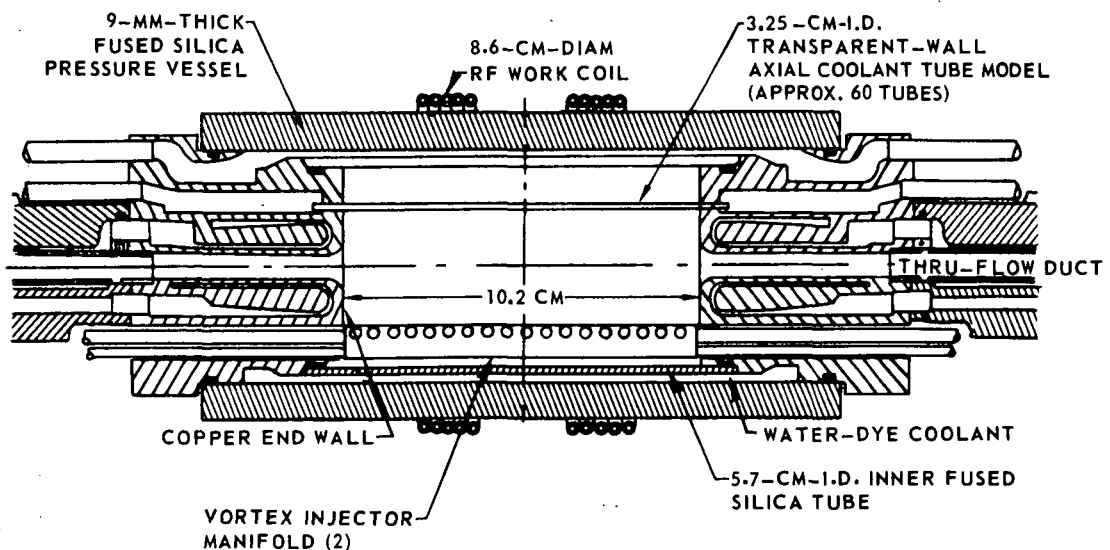
(a) CONFIGURATION FOR TESTS WITH FUSED SILICA TUBE PRESSURE VESSEL AND SIMULATED -FUEL INJECTION



(b) CONFIGURATION FOR TESTS WITH FILAMENT-WOUND PRESSURE VESSEL

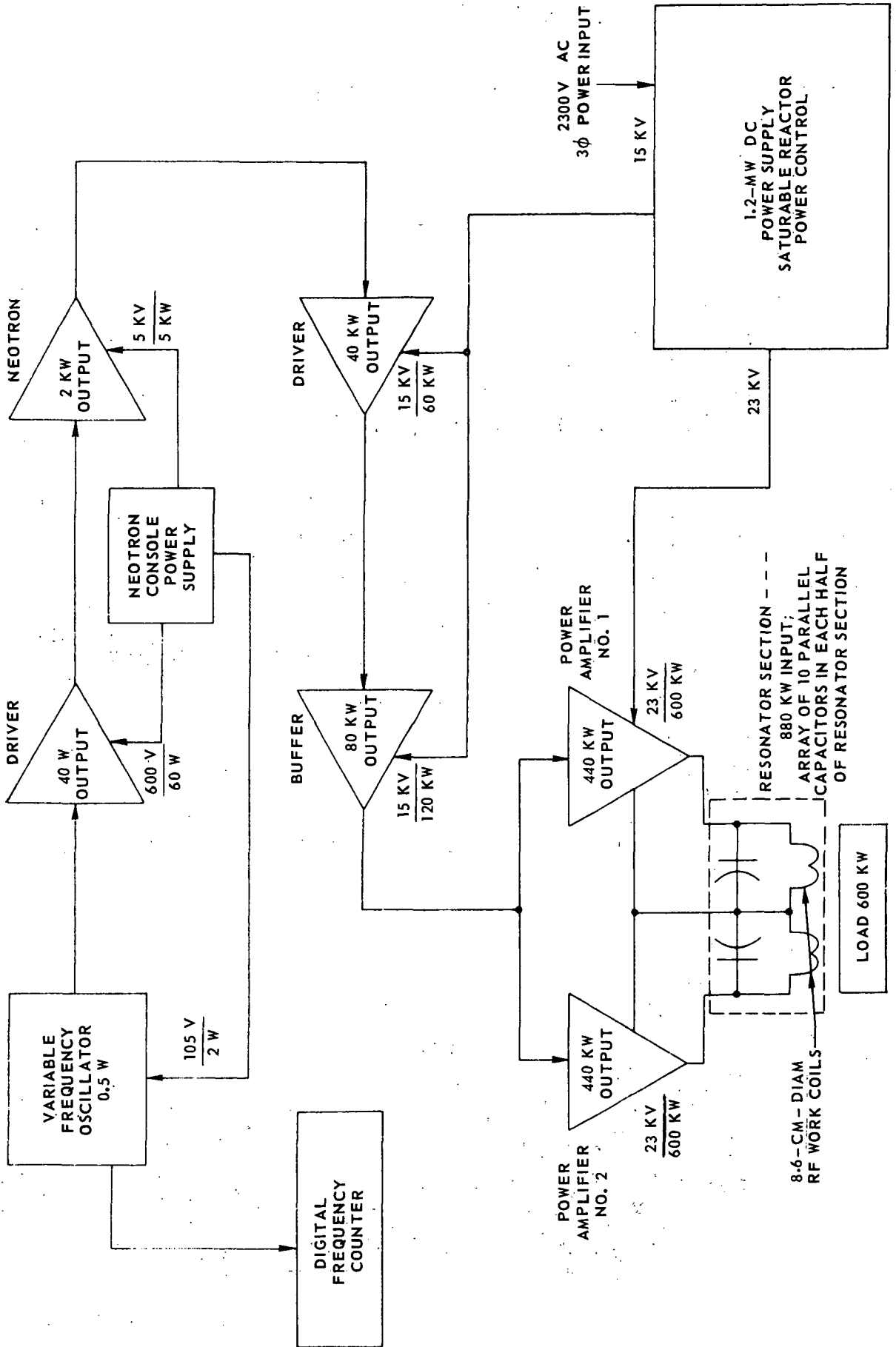


(c) CONFIGURATION FOR TESTS WITH TRANSPARENT-WALL MODEL



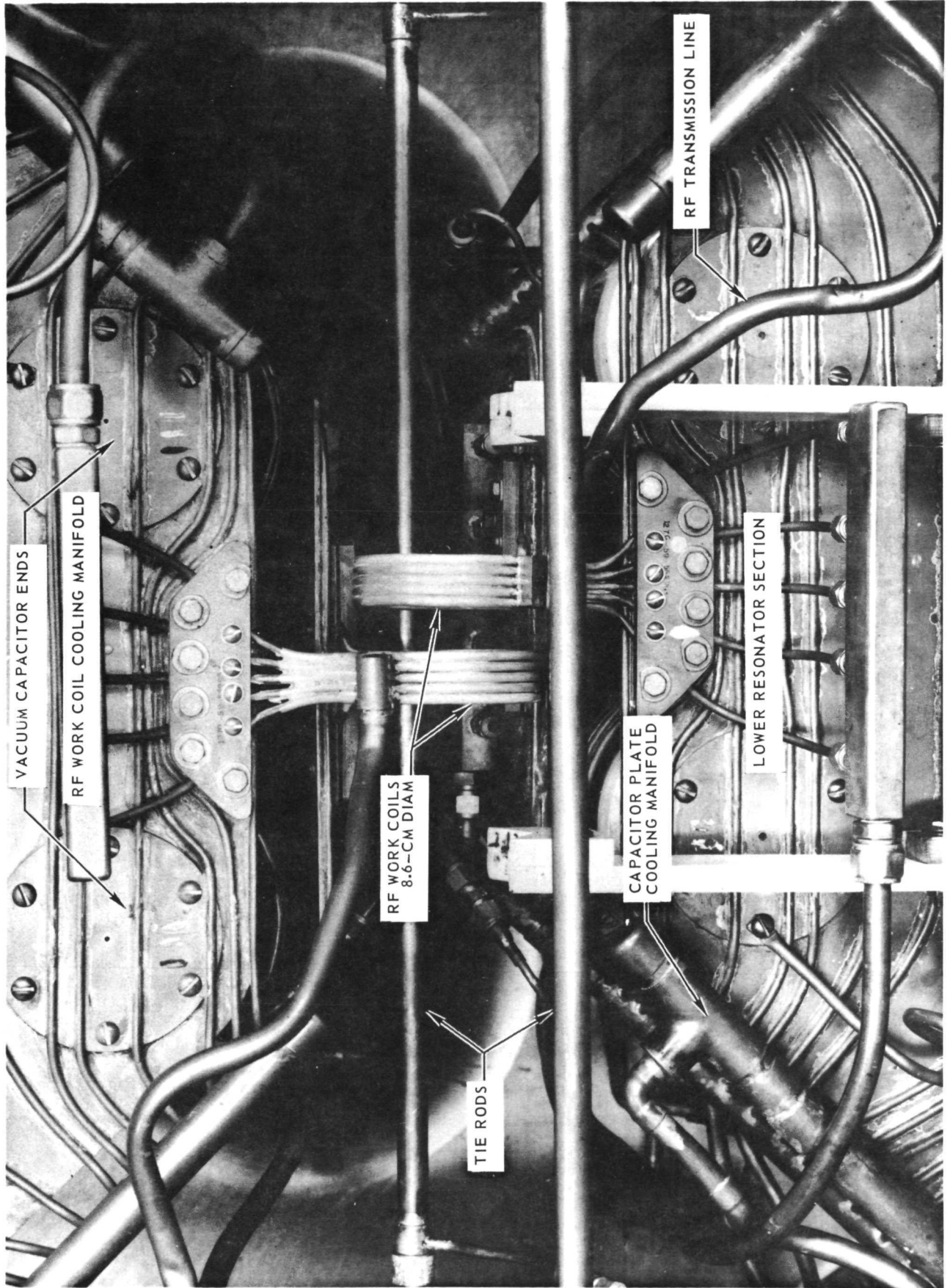
# BLOCK DIAGRAM OF UARL 1.2-MW RF INDUCTION HEATER

OPERATING FREQUENCY  $\approx 5.4 \text{ MHz}$   
 POWER LEVELS SHOWN ARE MAXIMUM DESIGN VALUES  
 MAXIMUM TOTAL DC INPUT POWER DURING THIS PROGRAM FOR POWER  
 AMPLIFIERS 1 AND 2 WAS APPROXIMATELY 600 KW

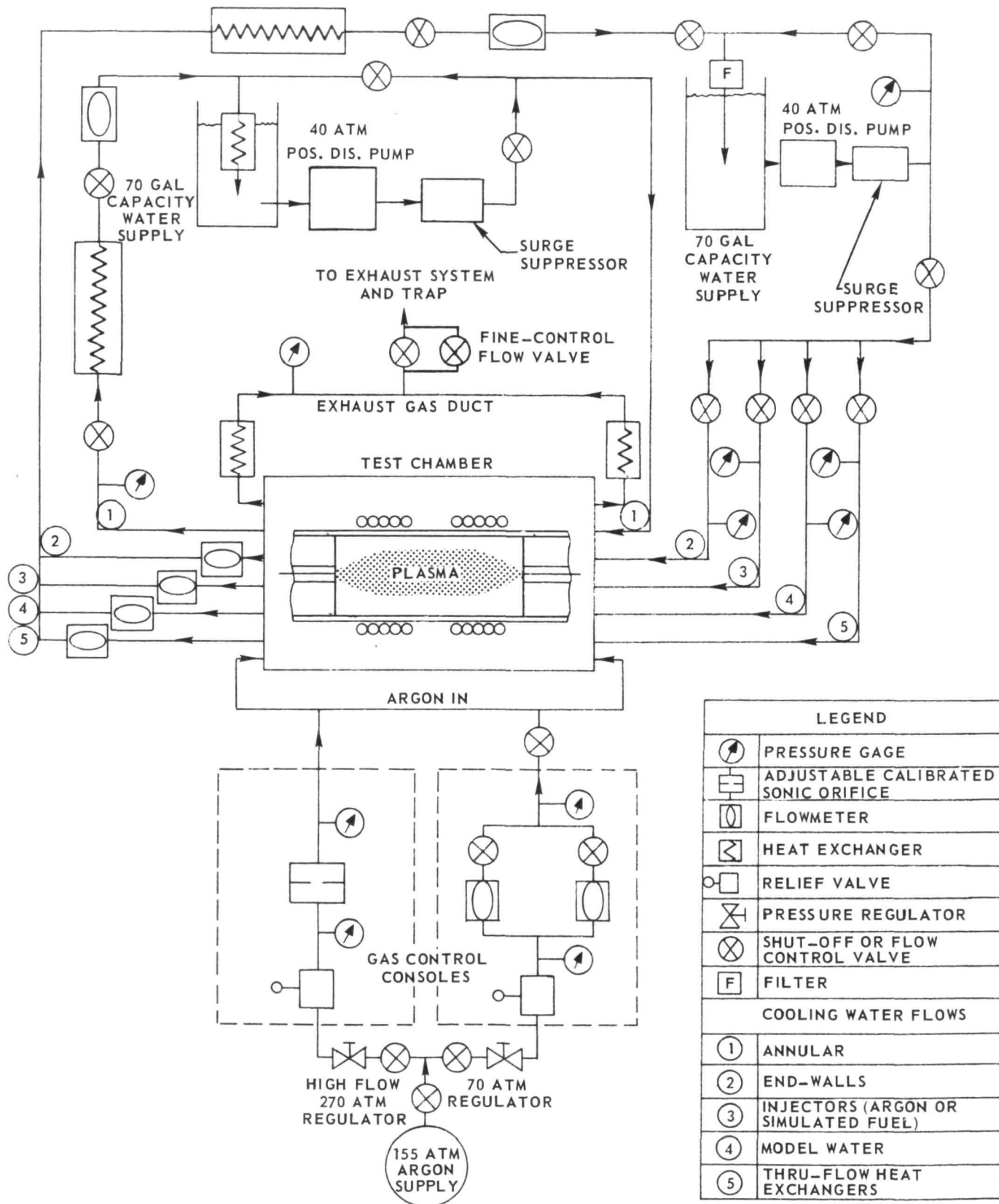




PHOTOGRAPH OF 1.2-MW RF INDUCTION HEATER RESONATOR SECTION

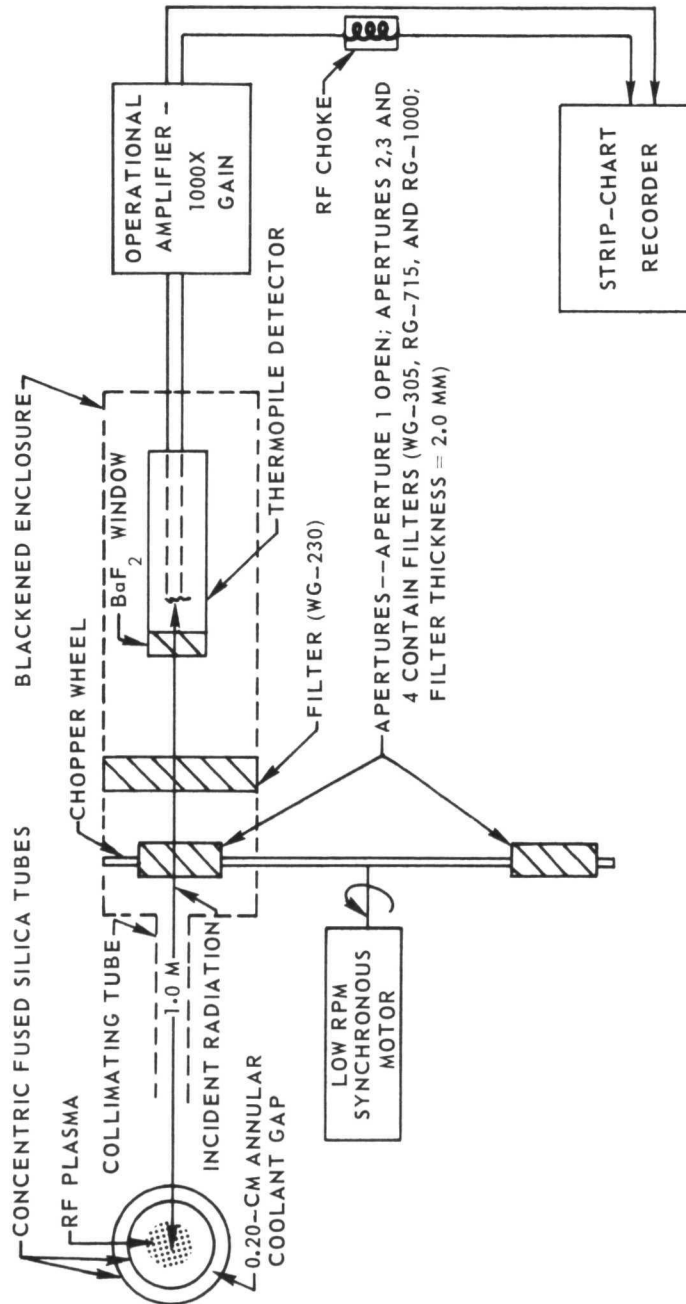


**SCHEMATIC OF 1.2-MW RF INDUCTION HEATER GAS AND COOLING WATER FLOW SYSTEMS**



RADIOMETER OPTICAL SYSTEM

(a) BLOCK DIAGRAM



(b) TRANSMISSION CHARACTERISTICS

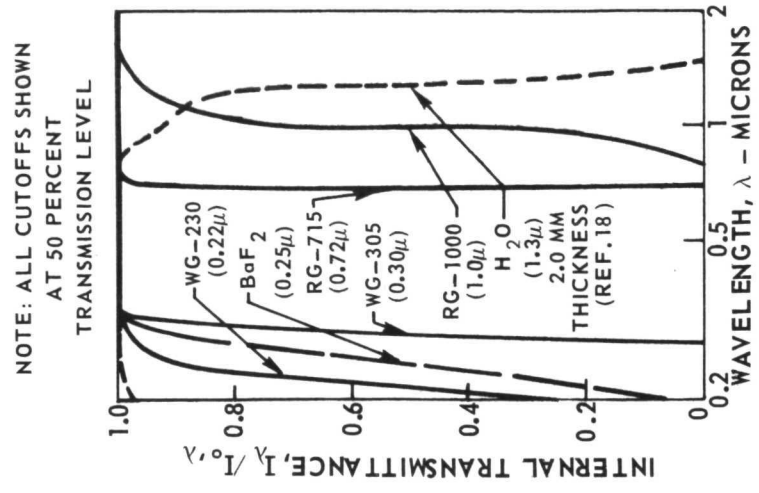


FIG. 7

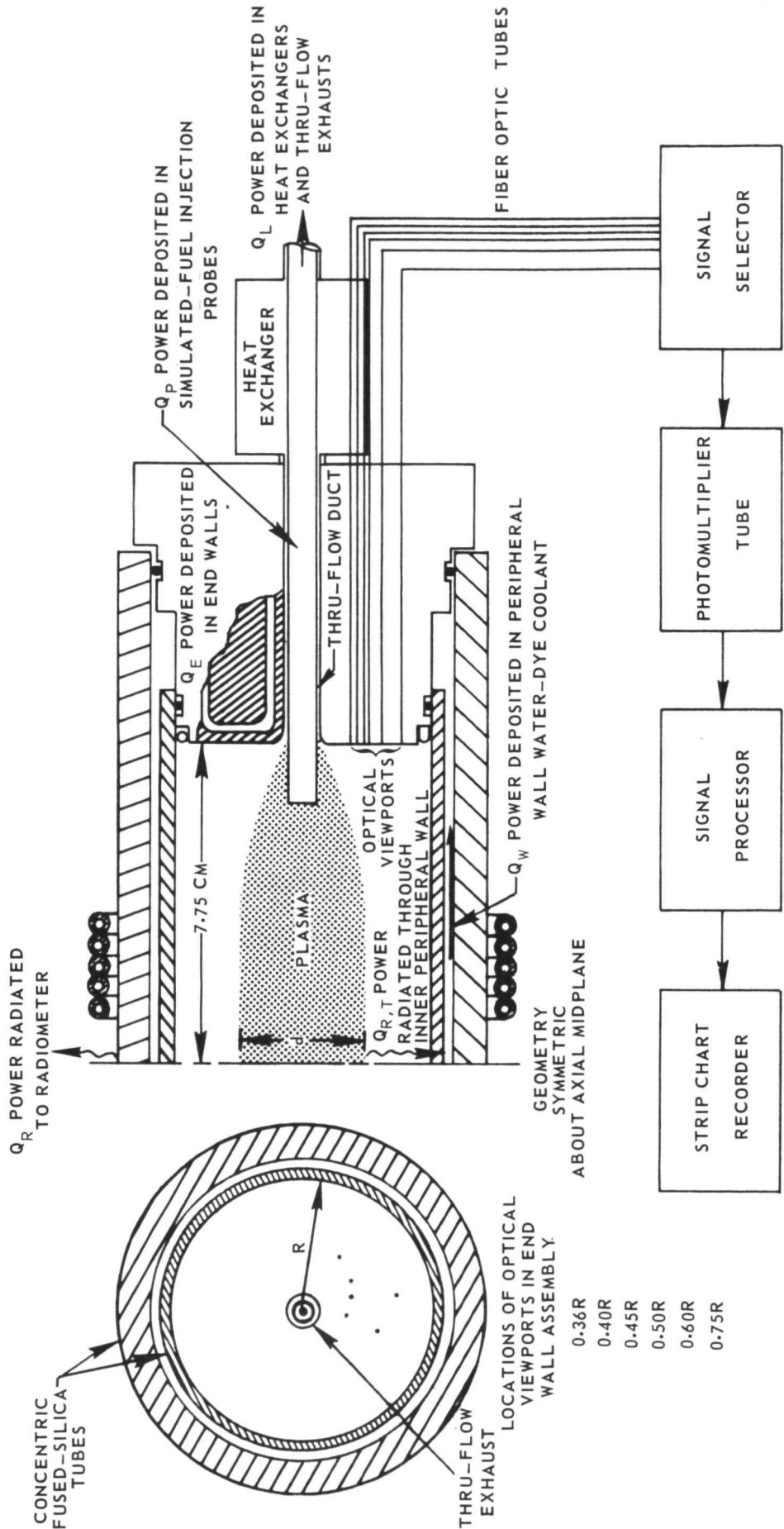


# SKETCH OF RF PLASMA SHOWING POWER BREAKDOWN AND OPTICAL TECHNIQUE FOR DETERMINING "EDGE-OF-PLASMA" LOCATION

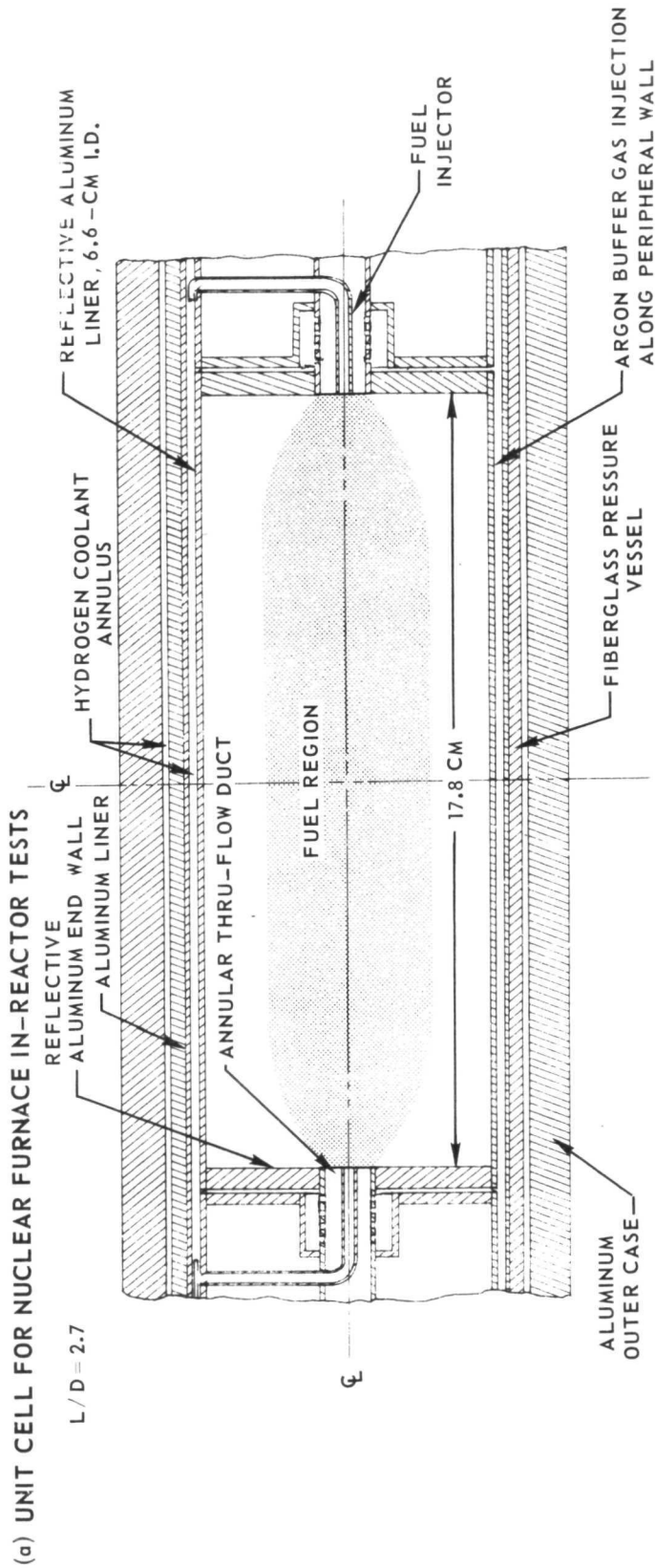
TOTAL POWER DEPOSITED IN PLASMA DISCHARGE,  $Q_T = Q_R + Q_W + Q_E + Q_L + Q_P$

POWER DEPOSITED IN END WALLS, PERIPHERAL WALL, HEAT EXCHANGERS, THRU-FLOW EXHAUSTS AND SIMULATED-FUEL INJECTION PROBES DETERMINED CALORIMETRICALLY

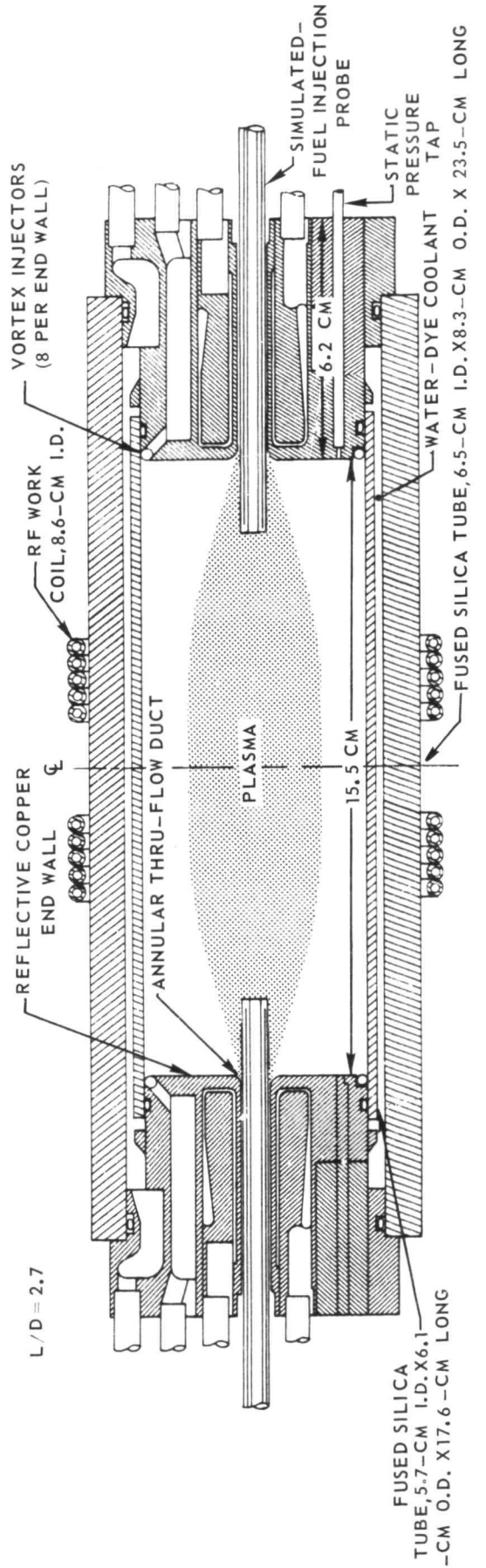
DISCHARGE DIAMETER,  $d$ , DETERMINED FROM OPTICAL SCANNING SYSTEM (SEE FIG. 8(a))



COMPARISON OF IN-REACTOR TEST UNIT CELL GEOMETRY WITH 7/8-SCALE IRG CONFIGURATION



(b) TEST CONFIGURATION FOR RF PLASMA TESTS UP TO 42 ATM PRESSURE



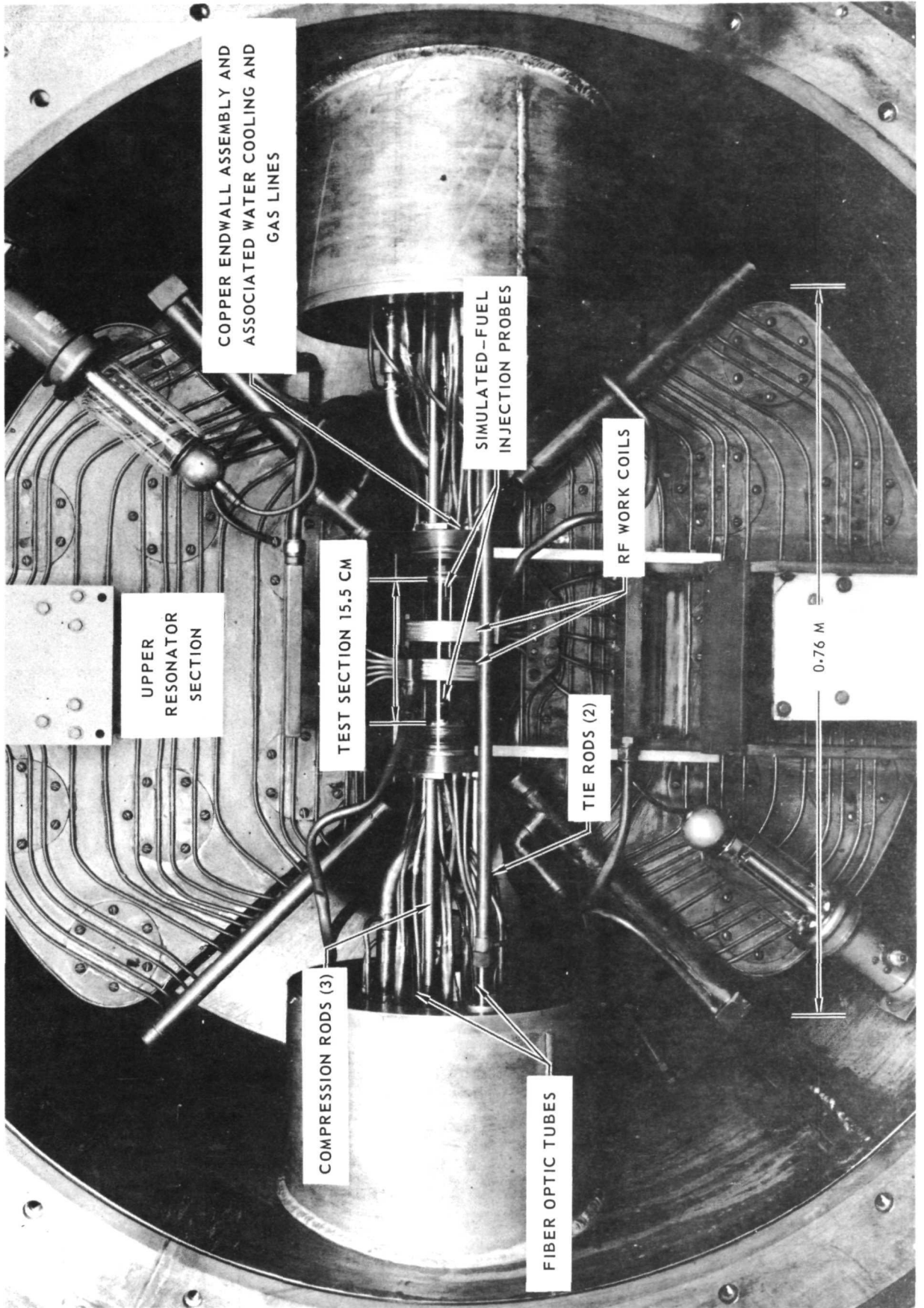
FUSED SILICA TUBE, 5.7-CM I.D. X 6.1-CM O.D. X 17.6-CM LONG



PHOTOGRAPH OF 7/8-SCALE IRG FUSED SILICA TUBE PRESSURE VESSEL CONFIGURATION  
IN 1.2-MW RF INDUCTION HEATER

FRONT DOME REMOVED

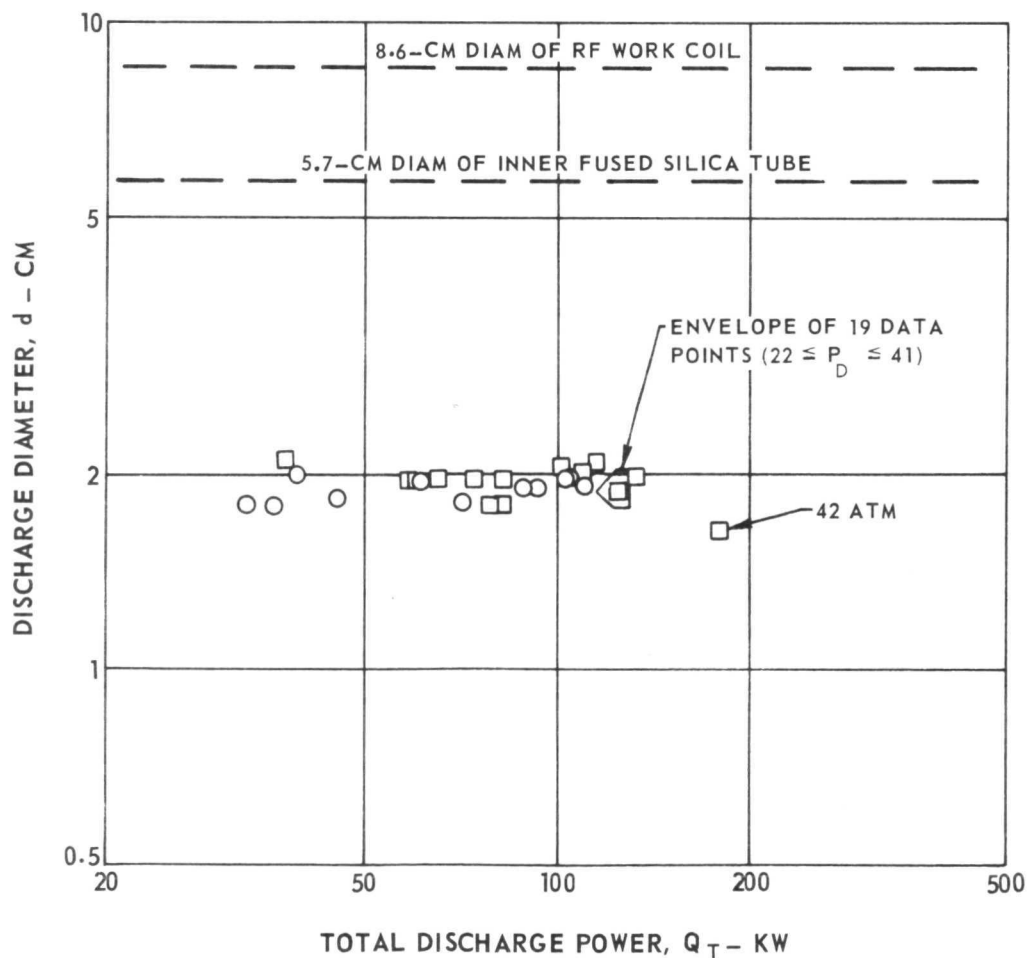
SEE FIG. 10(b) FOR DETAILS OF TEST CONFIGURATION



### MEASURED DIAMETERS OF ARGON RF PLASMAS IN TESTS OF 7/8-SCALE IRG CONFIGURATION

FUSED SILICA PRESSURE VESSEL CONFIGURATION; SEE FIG. 10(b)

SYMBOL	CHAMBER PRESSURE, $P_D$ - ATM	ARGON FLOW RATE, $W_A$ - g/SEC	RF OPERATING FREQUENCY, $f$ - MHz	SIMULATED-FUEL INJECTION PROBE AND THRU-FLOW DUCT DIAMETER
○	10-41	3.6-5.9	5.3996 - 5.4905	0.635-CM-O.D., 3 CONCENTRIC TUBE TYPE; 0.792-CM-DIAM DUCT
□	5-42	5.4-9.1	5.4001 - 5.4358	0.89-CM-O.D., 4 CONCENTRIC TUBE TYPE; 1.14-CM-DIAM DUCT





# SKETCH OF 7/8-SCALE IRG CONFIGURATION SHOWING POWER BREAKDOWN FOR HIGHEST-POWER/HIGHEST-PRESSURE OPERATING POINT

FUSED SILICA TUBE PRESSURE VESSEL CONFIGURATION

OPERATING FREQUENCY,  $f = 5.4053 \text{ MHz}$

CHAMBER PRESSURE,  $P_D = 42 \text{ ATM}$

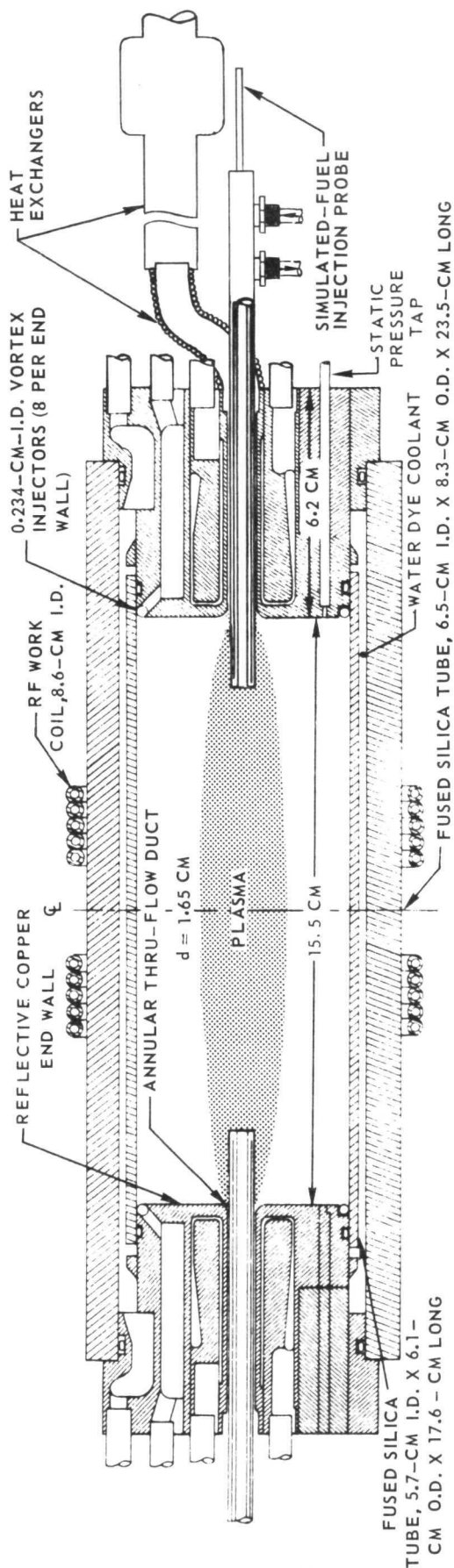
TOTAL DISCHARGE POWER,  $Q_T = 180 \text{ KW}$

PLASMA REFLECTED IMPEDANCE,  $Z_P = 444 \text{ OHMS}$

ARGON WEIGHT FLOW RATE,  $W_A = 8.6 \text{ g/SEC}$

ARGON INJECTION VELOCITY,  $V_j = 1.67 \text{ M/SEC}$

TEST CHAMBER LENGTH-TO-DIAMETER RATIO,  $L/D = 2.7$



$$Q_T = Q_R + Q_W + Q_E + Q_L + Q_P$$

POWER RADIATED TO RADIOMETER:  $Q_R = 26 \text{ KW}$   
 POWER IN ANNULAR WATER-DYE COOLANT:  $Q_W = 114 \text{ KW}$   
 POWER IN END-WALL COOLANT (BOTH ENDS):  $Q_E = 16 \text{ KW}$   
 POWER IN SIMULATED-FUEL INJECTION PROBES:  $Q_P = 13 \text{ KW}$   
 POWER IN HEAT EXCHANGER COOLANT (BOTH ENDS):  $Q_L = 11 \text{ KW}$

POWER RADIATED THROUGH INNER PERIPHERAL WALL,  $Q_{R,T} = 135 \text{ KW}$

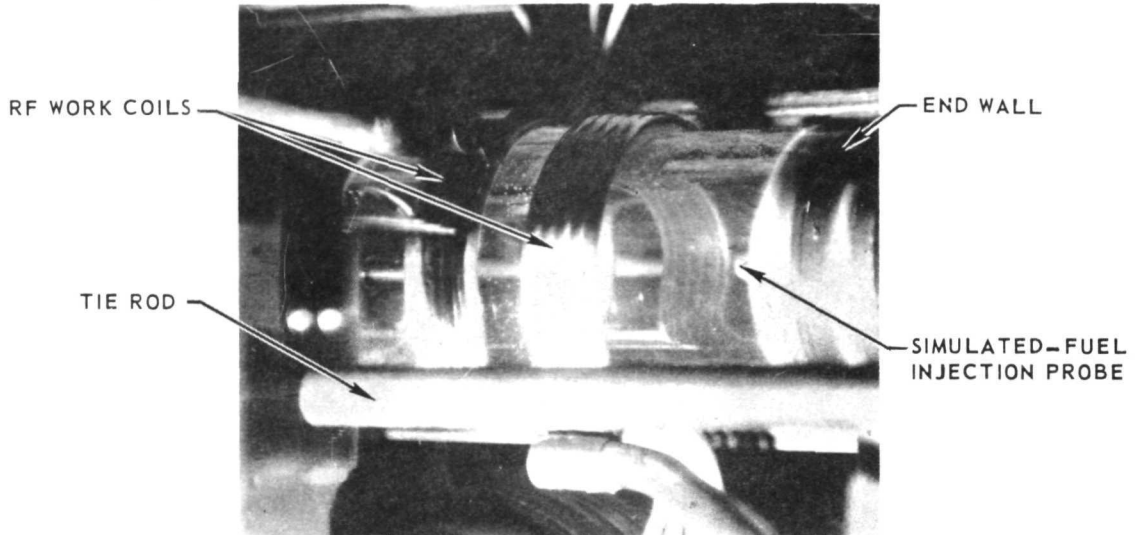
RADIATION EFFICIENCY = 0.75  
 $T^* = 4,320 \text{ }^\circ\text{K}$   
 RADIANT ENERGY FLUX,  $Q_{R,T}/A_S = 1.9 \text{ KW/CM}^2$

FIG. 13

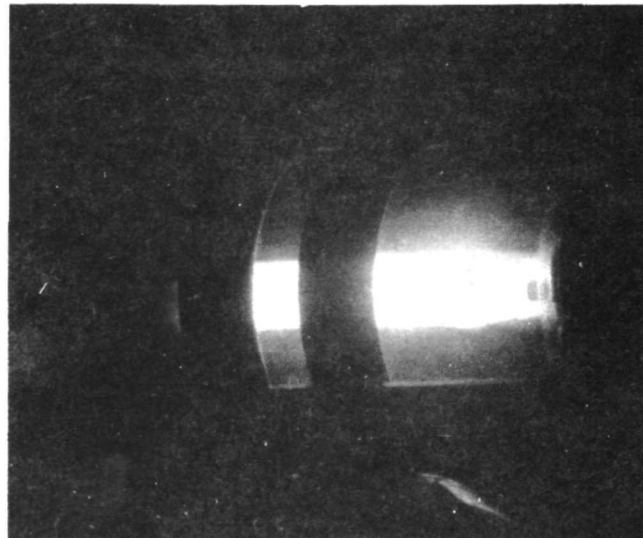
### PHOTOGRAPHS OF 7/8-SCALE IRG CONFIGURATION AND RF PLASMA AT 36 ATM

SEE FIG. 10(b) FOR DETAILS OF TEST CONFIGURATION

(a) VIEW THROUGH RIGHT VIEWPORT WITH NO PLASMA PRESENT



(b) VIEW THROUGH RIGHT VIEWPORT WITH PLASMA PRESENT



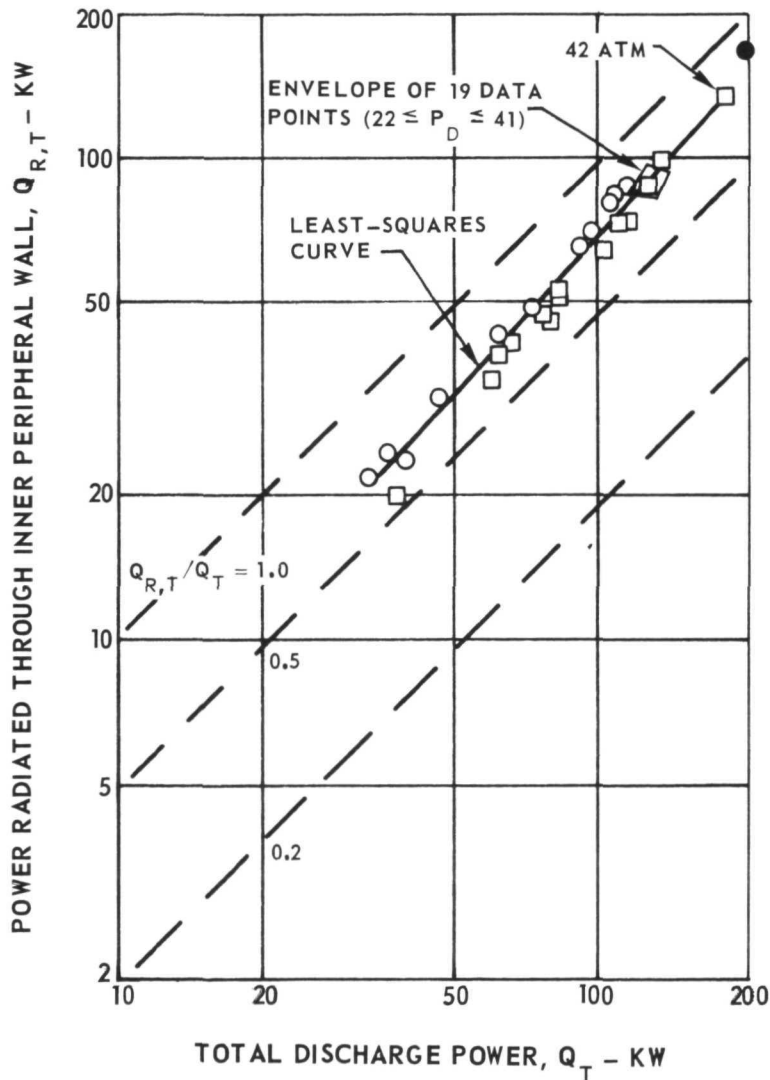
$P_D = 36 \text{ ATM}$   
 $d = 2.0 \text{ CM}$

$Q_T = 105 \text{ KW}$   
 $T^* = 3830 \text{ }^\circ\text{K}$

### VARIATION OF POWER RADIATED THROUGH INNER PERIPHERAL WALL WITH TOTAL DISCHARGE POWER

FUSED SILICA PRESSURE VESSEL CONFIGURATION; SEE FIG. 10(b)

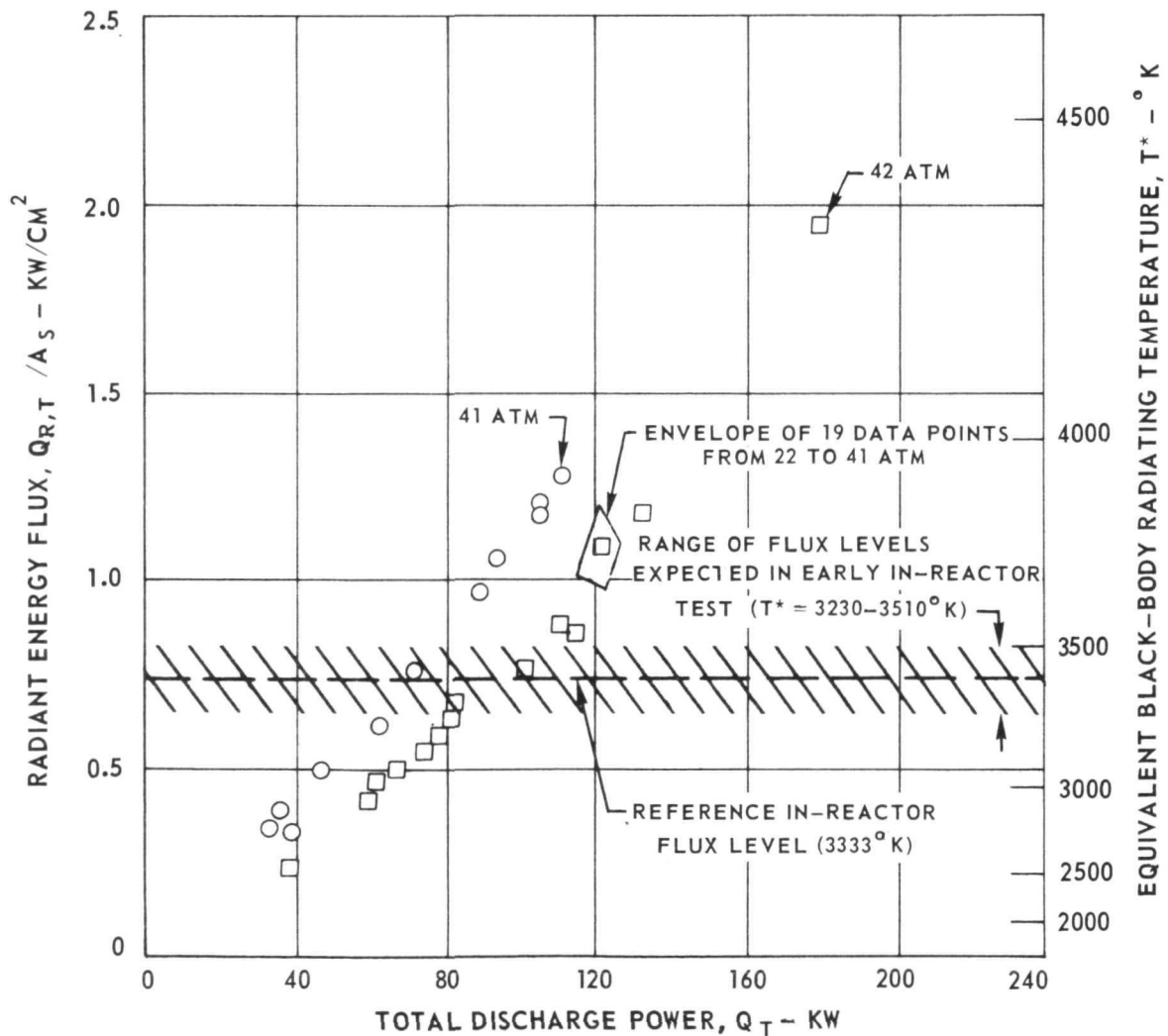
SYMBOL	CHAMBER PRESSURE, $P_D$ - ATM	ARGON FLOW RATE, $W_A$ - g/SEC	RF OPERATING FREQUENCY, $f$ - MHz	SIMULATED-FUEL INJECTION PROBE AND THRU-FLOW DUCT DIAMETER
○	10-41	3.6-5.9	5.3996- 5.4095	0.635-CM-O.D., 3 CONCENTRIC TUBE TYPE; 0.792-CM-DIAM DUCT
□	5-42	5.4-9.1	5.4001- 5.4358	0.89-CM-O.D., 4 CONCENTRIC TUBE TYPE; 1.14-CM-DIAM DUCT
●	DENOTES APPROXIMATE POWER LEVEL OF REFERENCE IN-REACTOR TEST			



### VARIATION OF RADIANT ENERGY FLUX WITH TOTAL DISCHARGE POWER

FUSED SILICA PRESSURE VESSEL CONFIGURATION; SEE FIG. 10 (b)

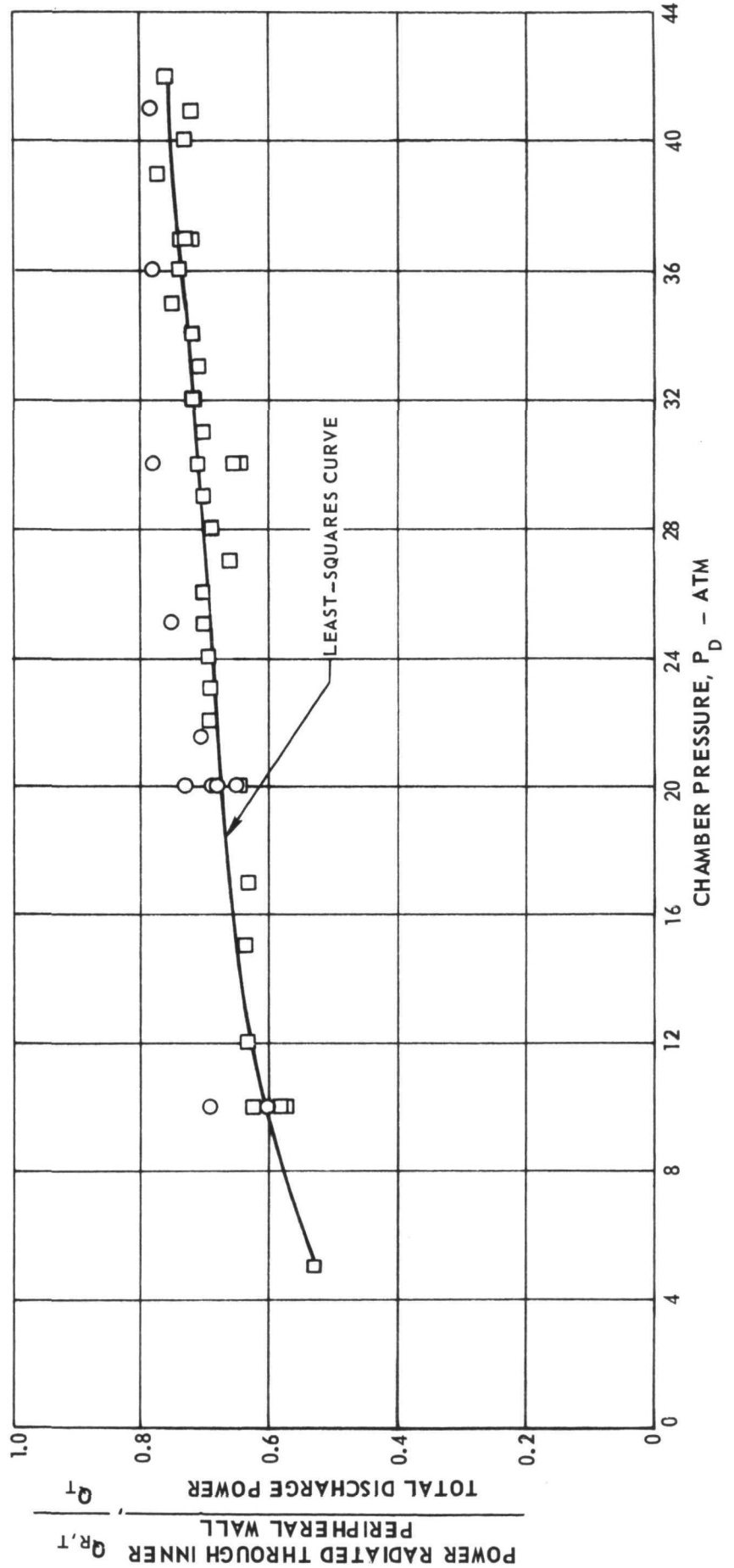
SYMBOL	CHAMBER PRESSURE, $P_D$ - ATM	ARGON FLOW RATE, $W_A$ - g /SEC	RF OPERATING FREQUENCY, $f$ - MHz	SIMULATED-FUEL INJECTION PROBE AND THRU-FLOW DUCT DIAMETER
○	10 - 41	3.6 - 5.9	5.3996 - 5.4095	0.635-CM-O.D., 3 CONCENTRIC TUBE TYPE; 0.792-CM-DIAM DUCT
□	5 - 42	5.4 - 9.1	5.4001 - 5.4358	0.89-CM-O.D., 4 CONCENTRIC TUBE TYPE; 1.14-CM-DIAM DUCT



# EFFECT OF CHAMBER PRESSURE ON THE FRACTION OF TOTAL DISCHARGE POWER RADIATED THROUGH INNER PERIPHERAL WALL

FUSED SILICA PRESSURE VESSEL CONFIGURATION; SEE FIG. 10(b)

SYMBOL	TOTAL DISCHARGE POWER, $Q_T$ -KW	ARGON FLOW RATE, $W_A$ - g/SEC	RF OPERATING FREQUENCY, $f$ - MHz	SIMULATED-FUEL INJECTION PROBE AND THRU-FLOW DUCT DIA METER
○	32.9-111.0	3.6-5.9	5.3996- 5.4095	0.635-CM-O.D., 3 CONCENTRIC TUBE TYPE; 0.792-CM-DIAM DUCT
□	37.4-180.0	5.4-9.1	5.4001- 5.4358	0.89-CM-O.D., 4 CONCENTRIC TUBE TYPE; 1.14-CM-DIAM DUCT



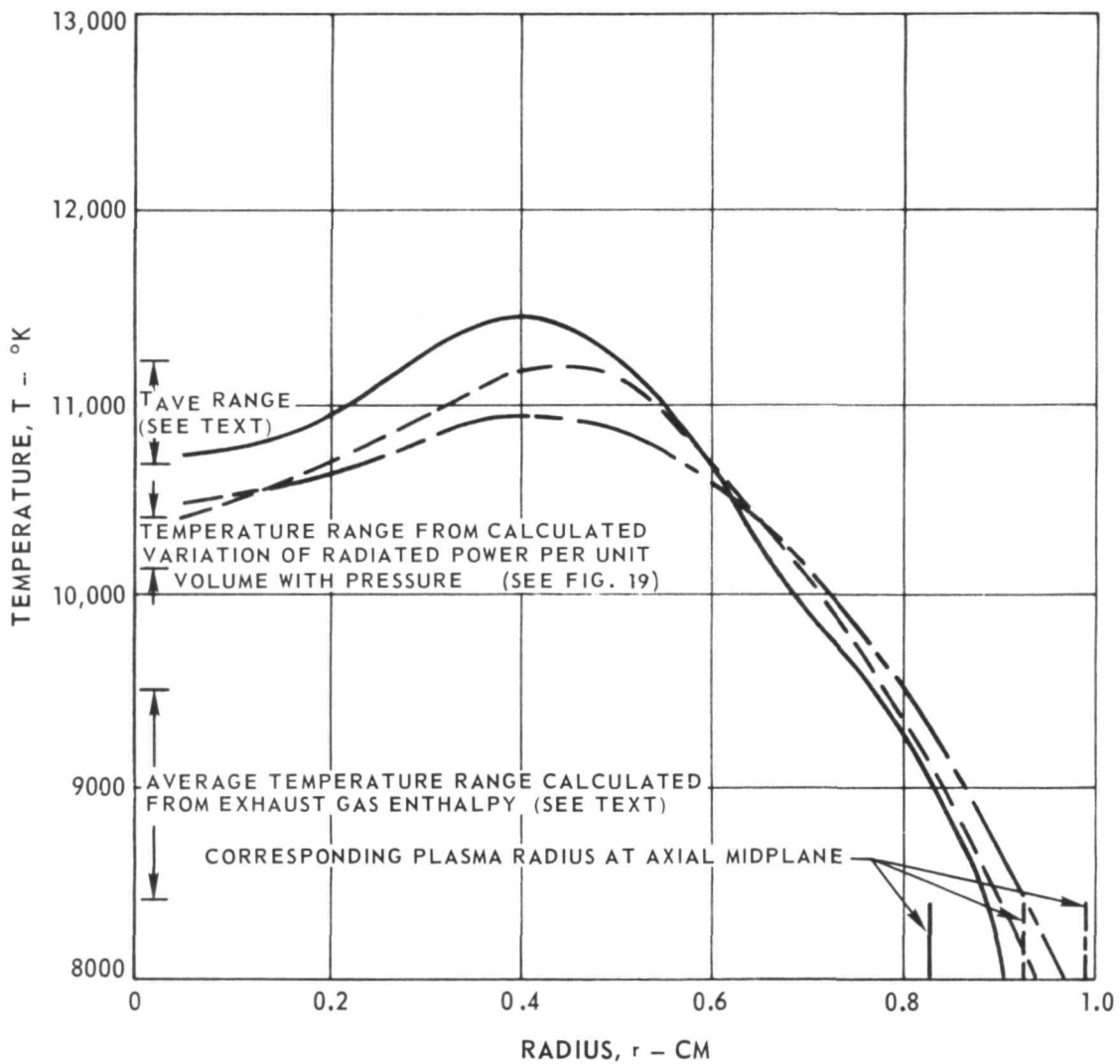
## RADIAL DISTRIBUTIONS OF TEMPERATURE OBTAINED FROM ARGON RF PLASMA IN 7/8-SCALE IRG CONFIGURATION

SEE FIG.10(b) FOR SKETCH OF CONFIGURATION

SEE FIG. 8 FOR SCHEMATIC OF OPTICAL SYSTEM USED

TEMPERATURE PROFILES DETERMINED FROM ARGON CONTINUUM AT 4320 Å  
1.2-MEGW RF INDUCTION HEATER OPERATING FREQUENCY,  $f = 5.4053 \text{ MHz}$

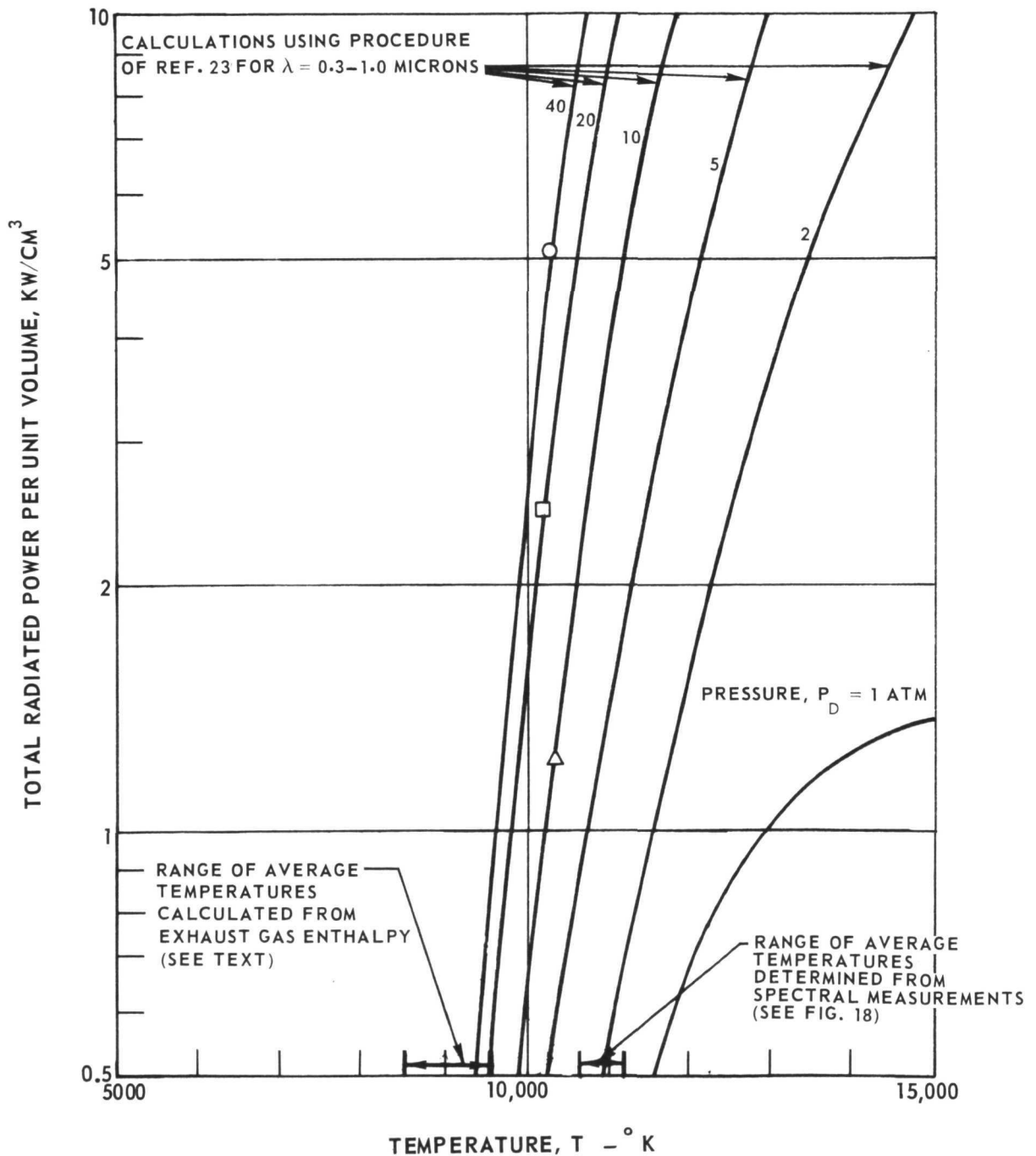
CASE	$P_D$ -ATM	$Q_T$ -KW	$W_A$ -g/SEC	$d$ -CM	$T^*$ - °K
I ———	42	180	8.63	1.65	4320
II - - - -	22	121	7.58	1.85	3730
III - - - -	10	62	5.68	1.99	3050



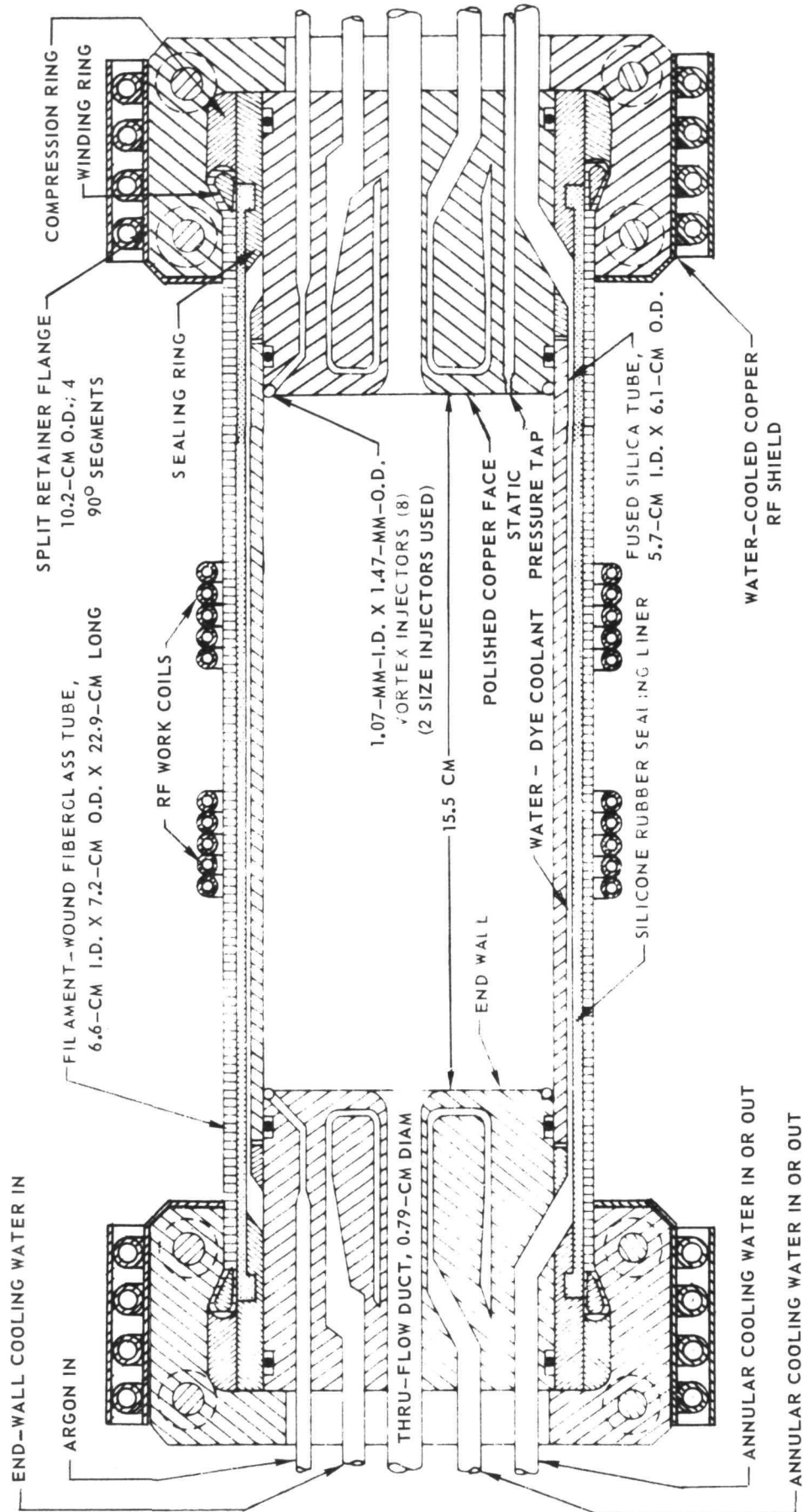
COMPARISON OF EXPERIMENTAL AND CALCULATED VARIATION OF RADIATED POWER PER UNIT VOLUME WITH TEMPERATURE IN 7/8-SCALE IRG CONFIGURATION

CASE	SYMBOL	$P_D$ - ATM	$Q_T$ - KW	$W_A$ - g/SEC	$d$ - CM	$T^*$ - °K
I	○	42	180	8.63	1.65	4320
II	□	22	121	7.58	1.85	3720
III	△	10	62	5.68	1.99	3050

FUSED SILICA PRESSURE VESSEL CONFIGURATION; SEE FIG. 10(b)



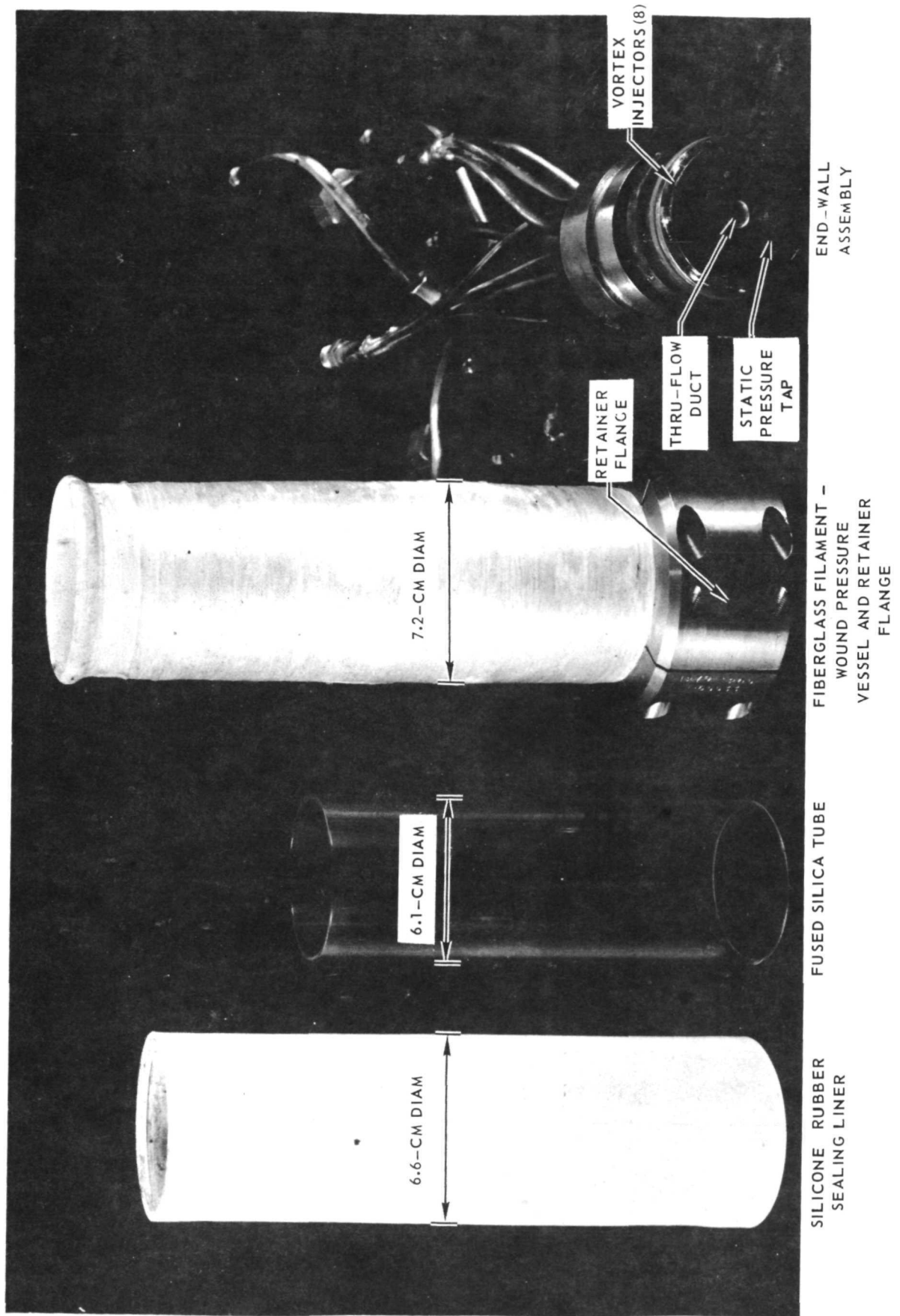
SKETCH OF 7/8-SCALE IRG FILAMENT-WOUND PRESSURE VESSEL CONFIGURATION





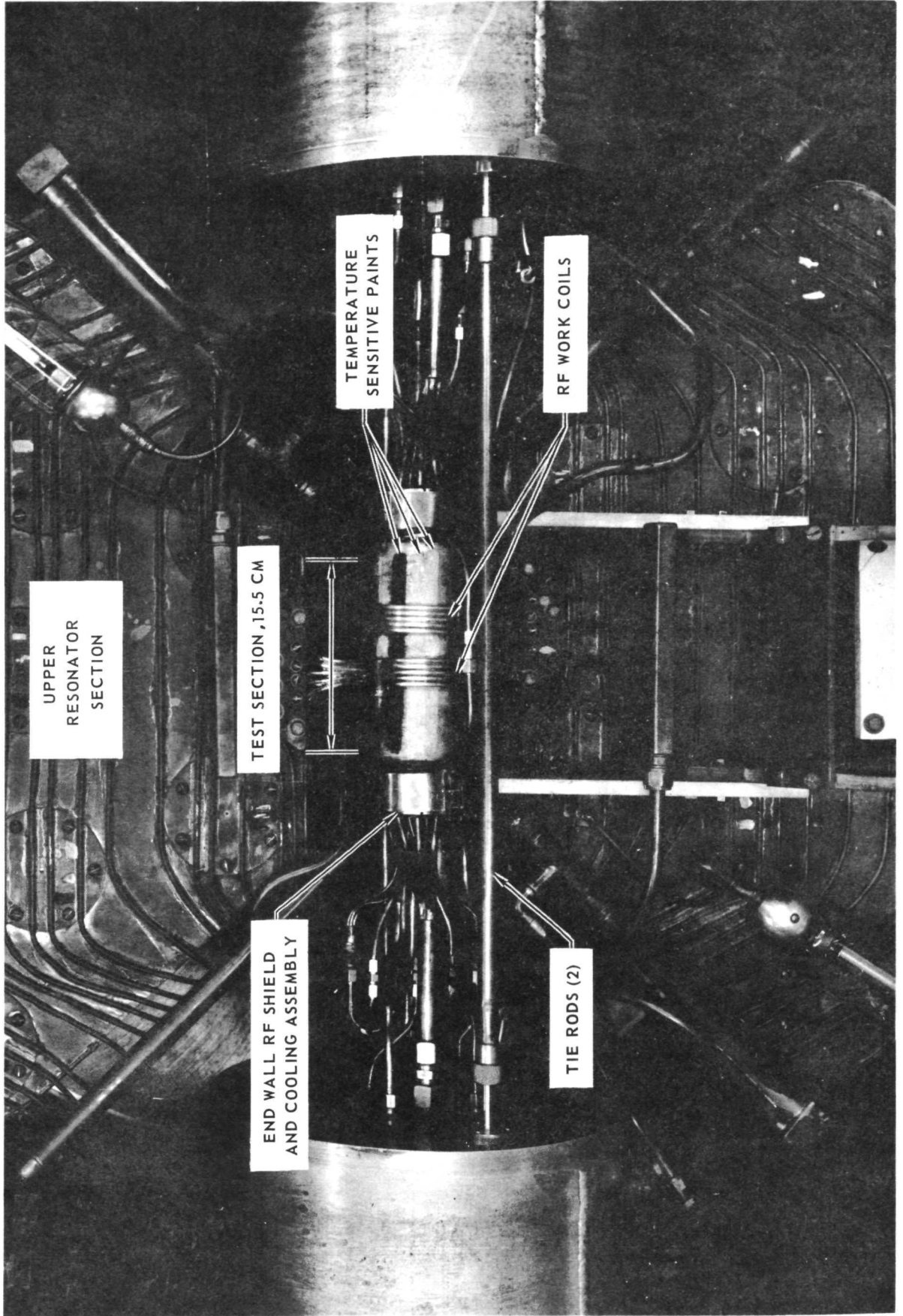
# PHOTOGRAPHS OF 7/8-SCALE IRG FILAMENT-WOUND PRESSURE VESSEL COMPONENTS

SEE FIG. 20 FOR DETAILS OF TEST CONFIGURATION



PHOTOGRAPH OF 7/8-SCALE IRG FILAMENT-WOUND PRESSURE VESSEL CONFIGURATION  
INSTALLED IN 1.2-MW RF INDUCTION HEATER

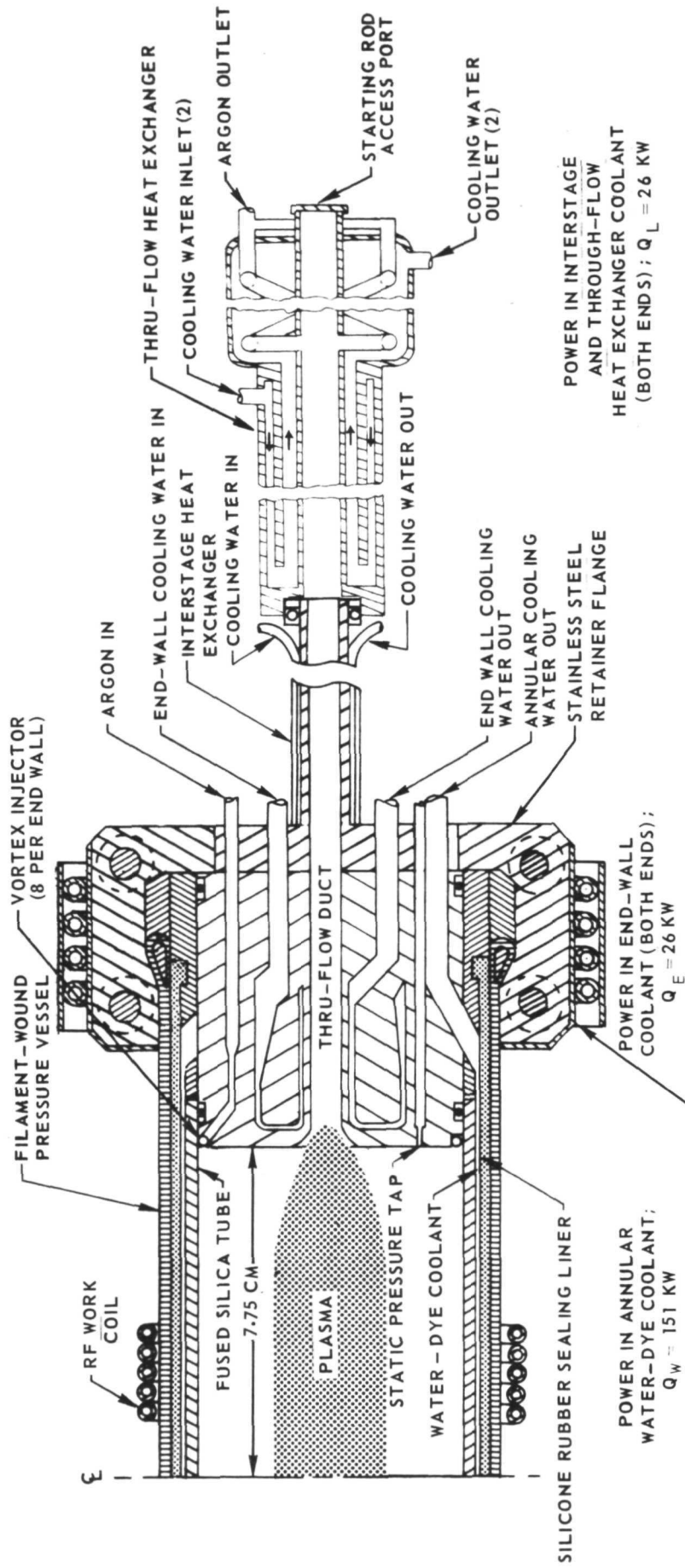
FRONT DOME REMOVED  
SEE FIG. 20 FOR DETAILS OF CONFIGURATION



# SKETCH OF 7/8 - SCALE IRG CONFIGURATION SHOWING POWER BREAKDOWN FOR HIGHEST-POWER/HIGH-PRESSURE OPERATING POINT

## FILAMENT-WOUND PRESSURE VESSEL CONFIGURATION

OPERATING FREQUENCY,  $f = 5.4093$  MHz  
 CHAMBER PRESSURE,  $P = 40$  ATM  
 TOTAL DISCHARGE POWER,  $Q_T = 203$  KW  
 PLASMA REFLECTED IMPEDANCE,  $Z_P = 662$  OHMS  
 ARGON WEIGHT FLOW RATE,  $W_A = 11.8$  g/SEC  
 ARGON INJECTION VELOCITY,  $V_j = 2.4$  M/SEC



POWER IN INTERSTAGE AND THROUGH-FLOW HEAT EXCHANGER COOLANT (BOTH ENDS);  $Q_L = 26$  KW

POWER IN ANNULAR WATER-DYE COOLANT;  $Q_W = 151$  KW

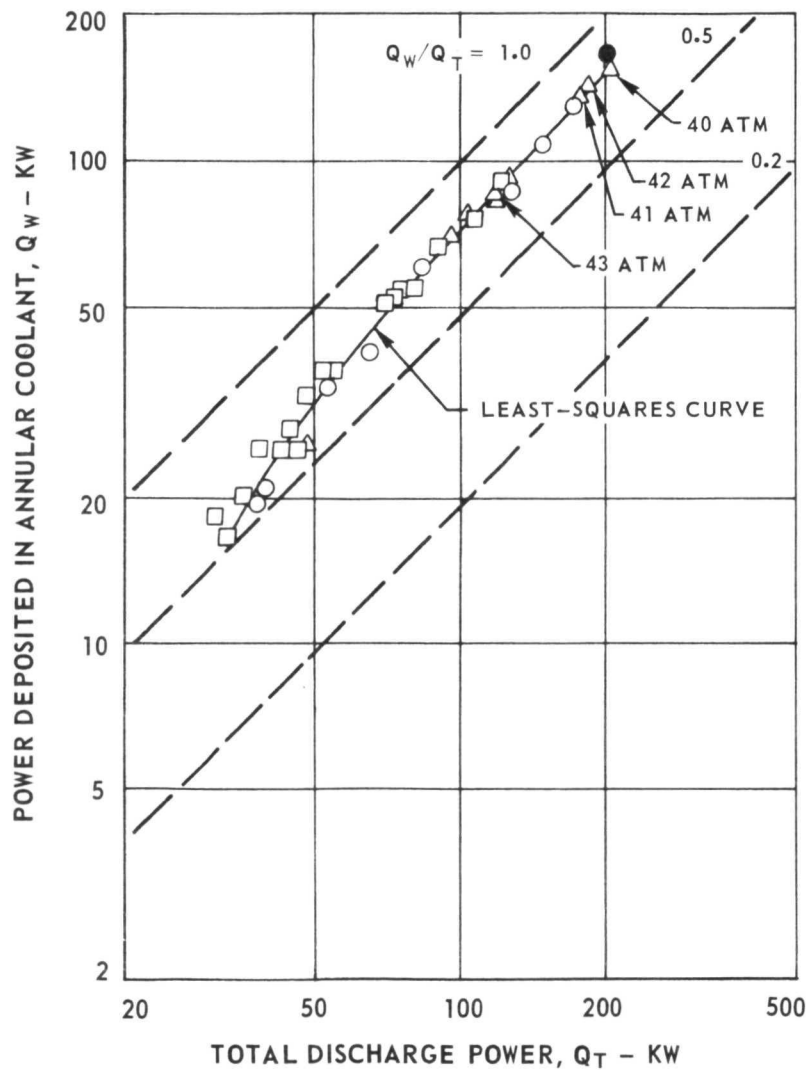
WATER-COOLED COPPER RF SHIELD  $Q_T = Q_W + Q_E + Q_L$

FRACTION OF TOTAL DISCHARGE POWER DEPOSITED INTO THE ANNULAR COOLANT =  $\frac{Q_W}{Q_T} = \frac{Q_W}{Q_W + Q_E + Q_L} = \frac{151}{151 + 26 + 26} = 0.74$

## VARIATION OF POWER DEPOSITED IN ANNULAR COOLANT WITH TOTAL DISCHARGE POWER

FILAMENT-WOUND PRESSURE VESSEL CONFIGURATION; SEE FIG. 20

SYMBOL	RESIN MATERIAL	TEST CHAMBER LENGTH, CM	BUFFER-GAS INJECTOR I.D. - MM	RF WORK COIL DIAM - CM	RF OPERATING FREQUENCY, f - MHz	CHAMBER PRESSURE, P <sub>D</sub> - ATM	ARGON FLOW RATE, W <sub>A</sub> - g/SEC
○	63	14.0	1.07	7.8	5.4510 - 5.5900	5 - 30	4.1 - 8.2
□	2256	15.5	1.07	8.6	5.3658 - 5.3968	5 - 30	4.5 - 11.4
△	2256	15.5	2.34	8.6	5.4093 - 5.4184	10 - 43	5.1 - 11.8
●	DENOTES APPROXIMATE TOTAL POWER LEVEL OF REFERENCE IN-REACTOR TEST						



EFFECT OF CHAMBER PRESSURE ON THE FRACTION OF TOTAL DISCHARGE POWER DEPOSITED IN ANNULAR COOLANT

FILAMENT-WOUND PRESSURE VESSEL CONFIGURATION; SEE FIG. 20

SYMBOL	RESIN MATERIAL	TEST CHAMBER LENGTH, CM	BUFFER-GAS INJECTOR I.D., - MM	RF WORK COIL DIAM, CM	RF OPERATING FREQUENCY, f-MHz	TOTAL DISCHARGE POWER, $Q_T$ -KW	ARGON FLOW RATE, $W_A$ -g/SEC
○	63	14.0	1.07	7.8	5.4510-5.5900	38-172	4.1-8.2
□	2256	15.5	1.07	8.6	5.3658- 5.3968	31-120	4.5-11.4
△	2256	15.5	2.34	8.6	5.4093- 5.4184	45-203	5.1-11.8

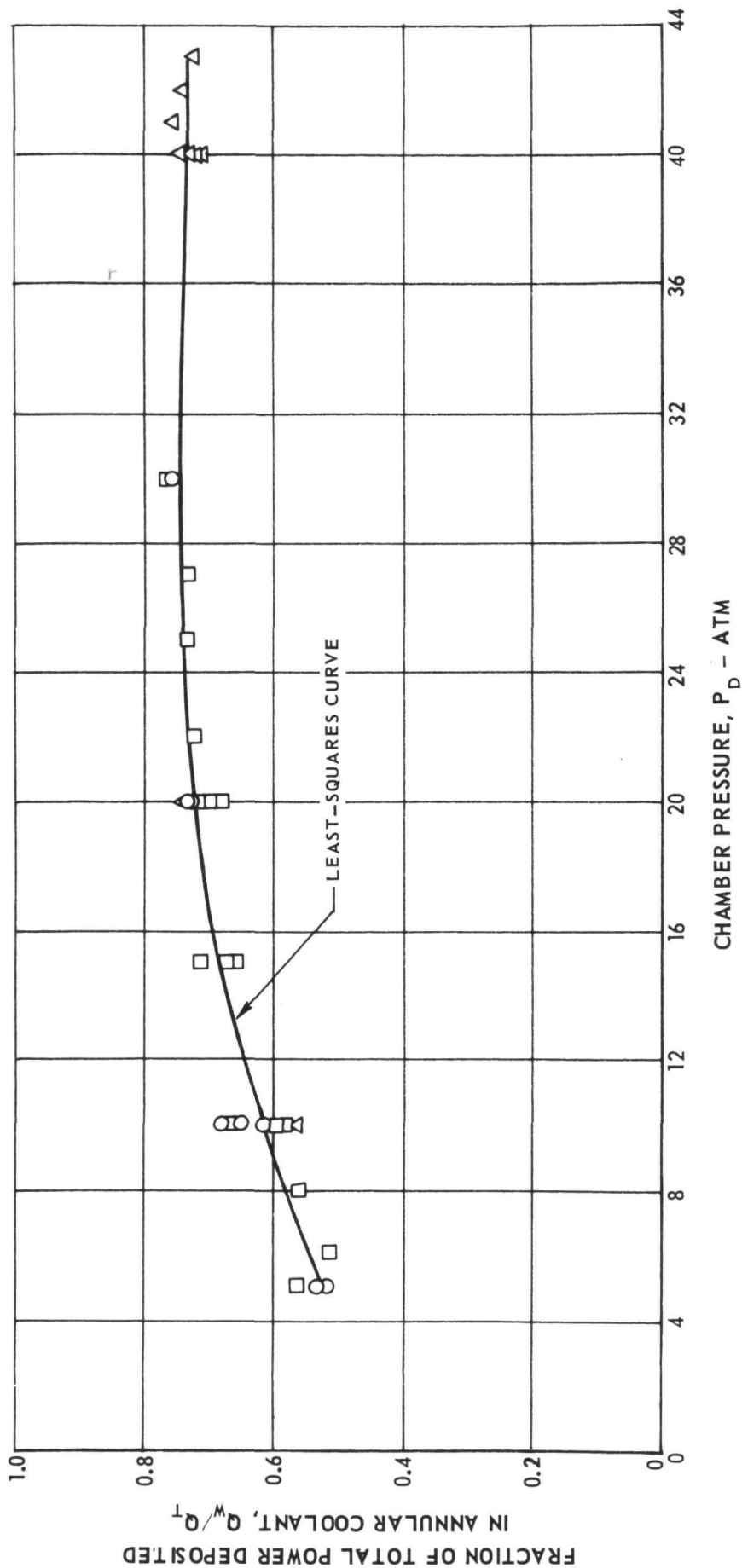


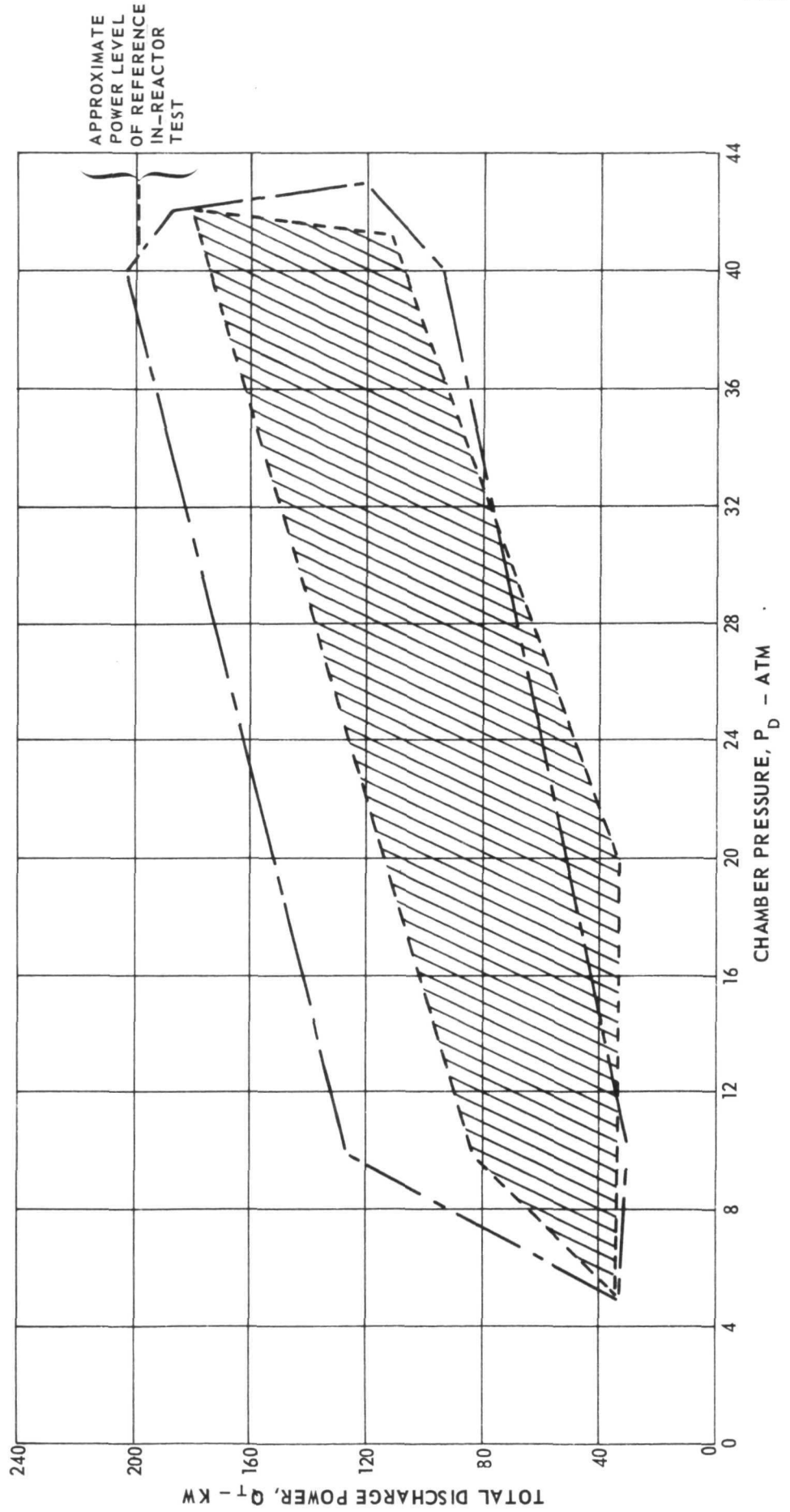
FIG. 25

# COMPARISON OF POWER-PRESSURE OPERATING ENVELOPES FOR FILAMENT-WOUND AND FUSED SILICA PRESSURE VESSELS

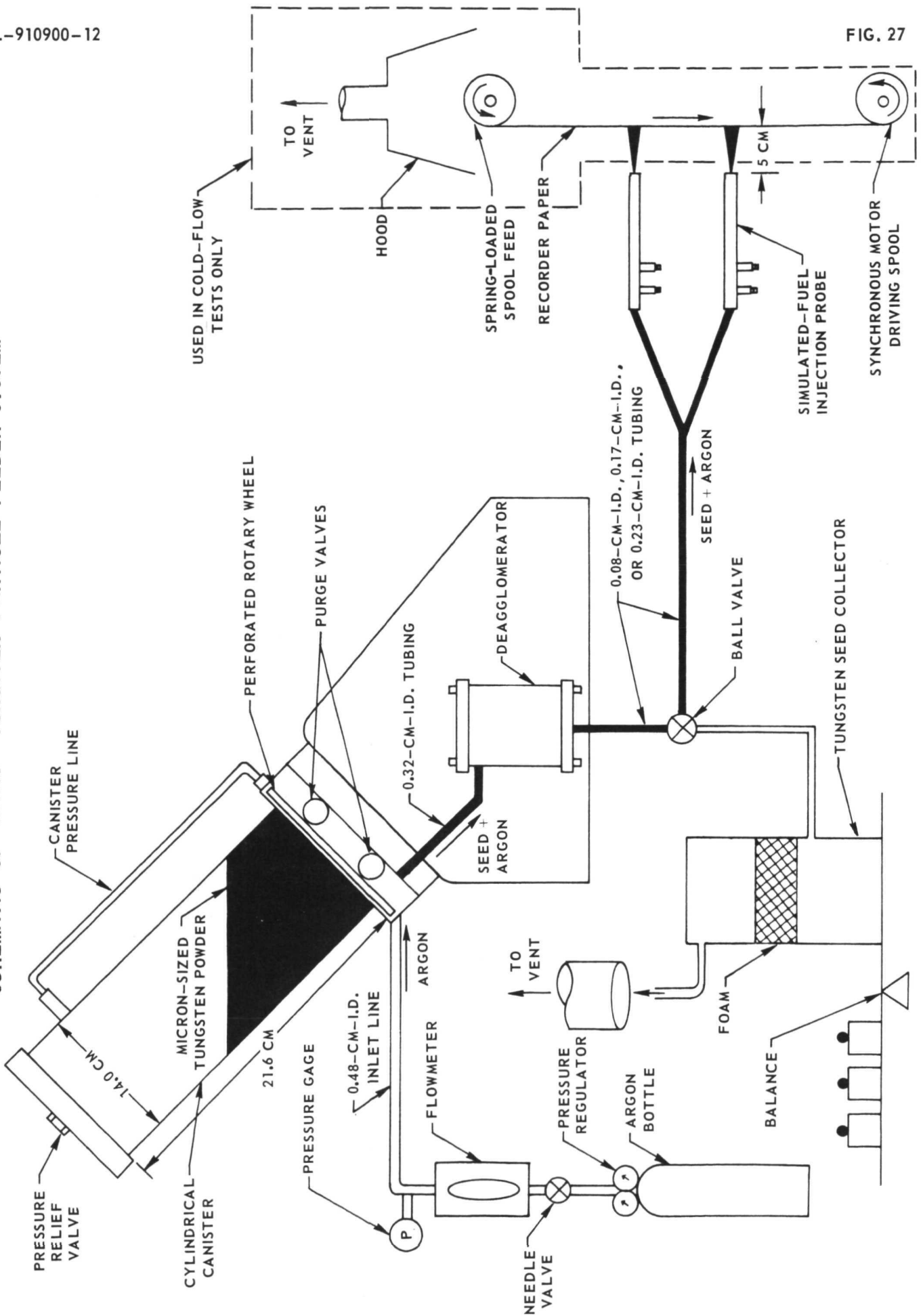
7/8-SCALE IRG CONFIGURATION

 FILAMENT-WOUND PRESSURE VESSEL CONFIGURATION; SEE FIG. 20

 FUSED SILICA PRESSURE VESSEL CONFIGURATION; SEE FIG. 10(b)

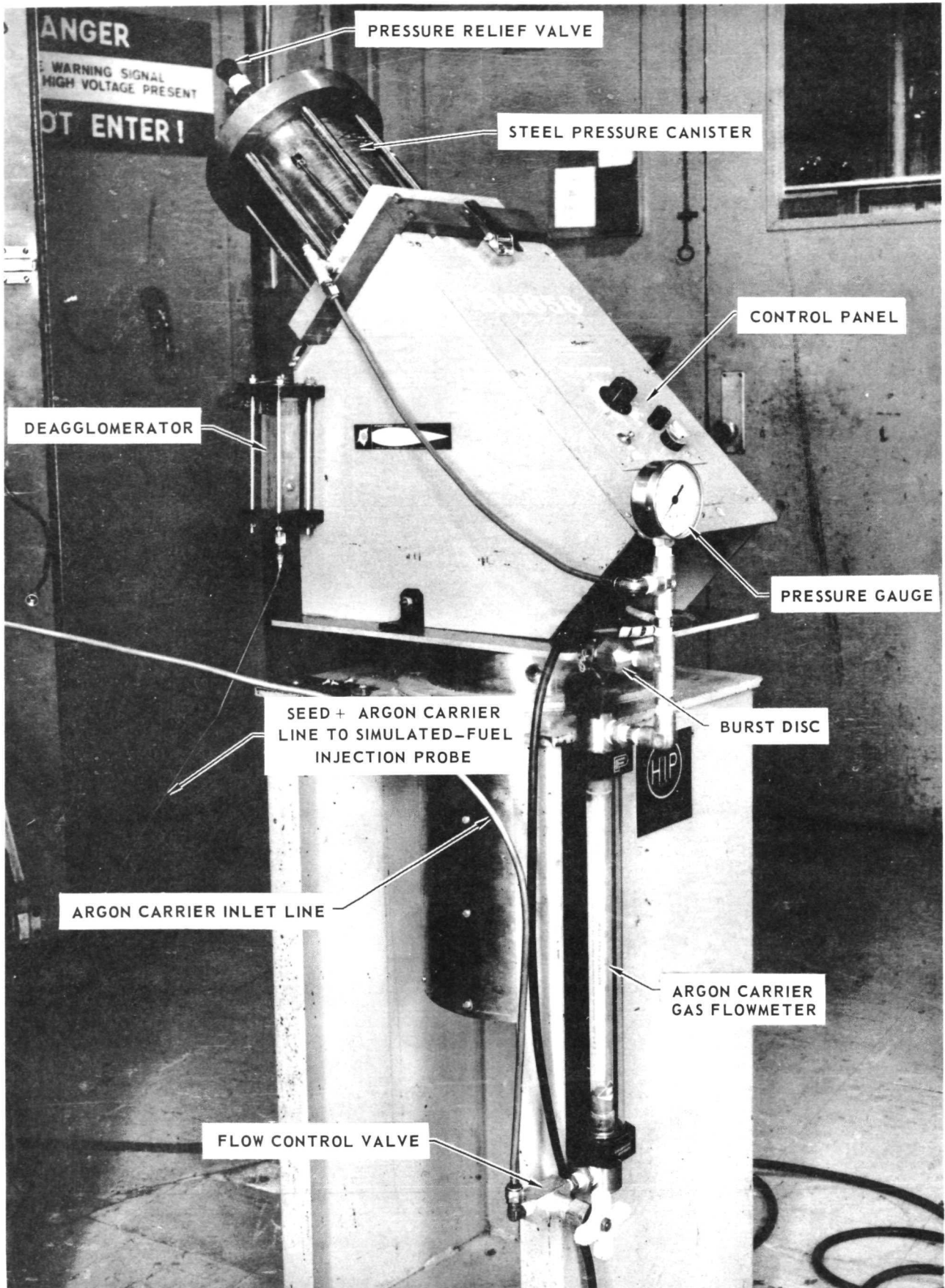


SCHEMATIC OF BASIC TUNGSTEN PARTICLE FEEDER SYSTEM





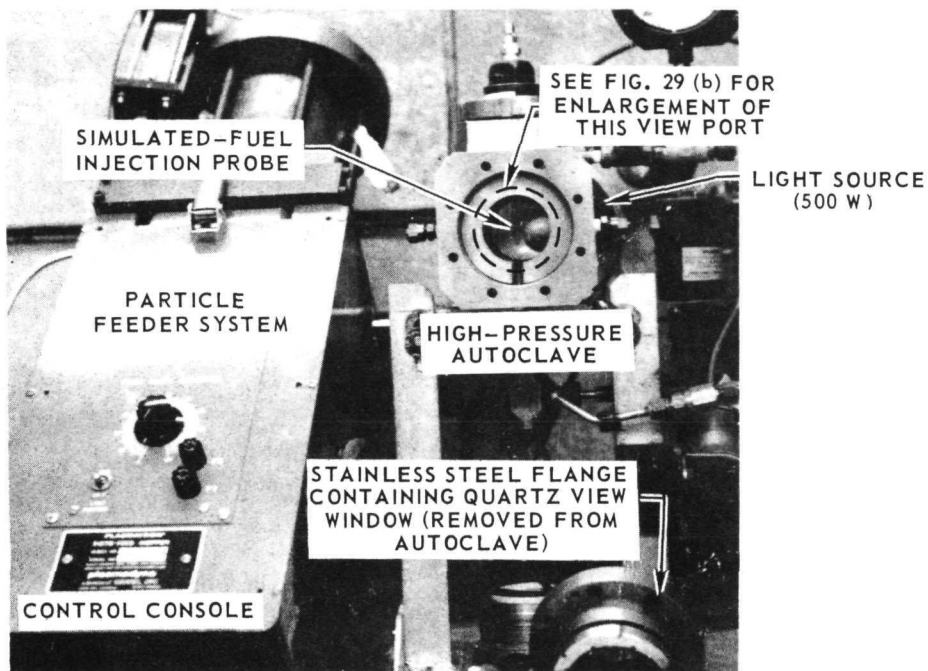
PHOTOGRAPH OF MODIFIED HIGH PRESSURE PARTICLE FEEDER SYSTEM  
USED IN RF PLASMA TESTS WITH SIMULATED-FUEL INJECTION



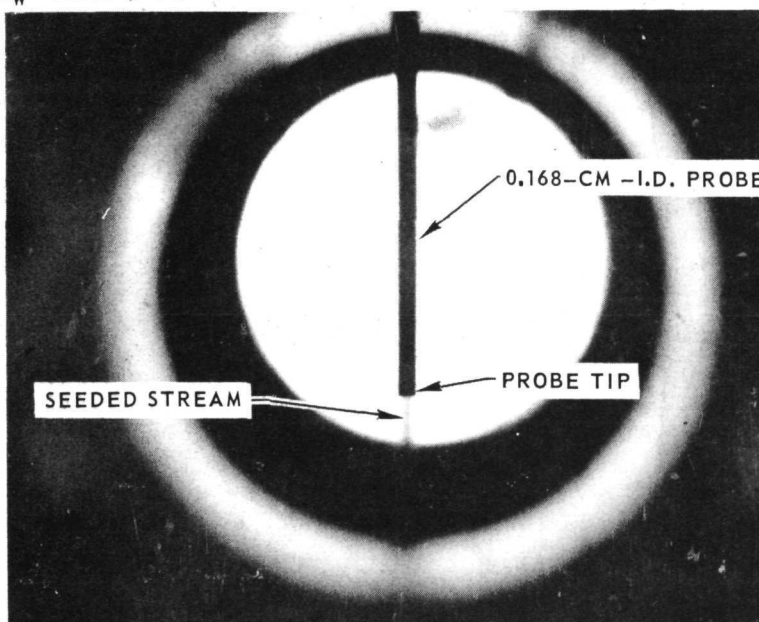


### PHOTOGRAPHS OF PARTICLE FEEDER SYSTEM USED WITH HIGH-PRESSURE AUTOCLAVE FOR TUNGSTEN SEEDING TESTS TO 40 ATM

(a) PHOTOGRAPH OF OVERALL TEST CONFIGURATION INCLUDING PARTICLE FEEDER SYSTEM AND HIGH-PRESSURE AUTOCLAVE



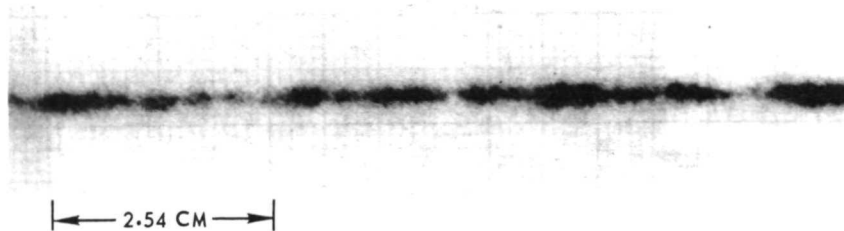
(b) PHOTOGRAPH OF TUNGSTEN SEED TEST AT 40 ATM LOOKING THROUGH VIEW PORT INTO AUTOCLAVE ; TUNGSTEN FLOW RATE,  $W_w = 0.038$  g/SEC



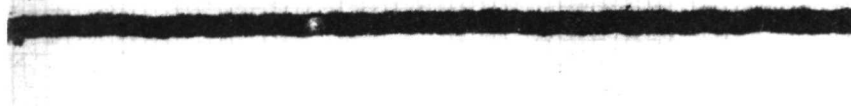
PHOTOGRAPHED TRACES OF TUNGSTEN PARTICLES AS DISCHARGED  
FROM SIMULATED-FUEL INJECTION PROBE AT 1 ATM

SEE FIG. 27 FOR SCHEMATIC OF TEST APPARATUS  
PAPER FEED SPEED 0.5 M/SEC LEFT TO RIGHT  
0.168 - CM - I.D. PROBE; ARGON FLOW RATE,  $w_A = 0.433$  g/SEC

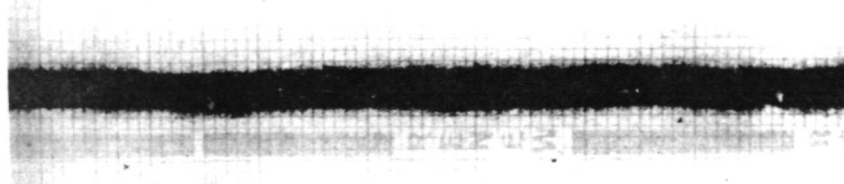
- (a) INITIAL TESTS WITH PARTICLE FEEDER SYSTEM (AS RECEIVED)  
NO DEAGGLOMERATOR; TUNGSTEN MASS FLOW  
RATE  $w_W = 0.025$  g/SEC



- (b) TESTS WITH MODIFIED PARTICLE FEEDER SYSTEM (FIG. 28)  
AND DEAGGLOMERATOR; TUNGSTEN MASS FLOW  
RATE  $w_W = 0.0575$  g/SEC

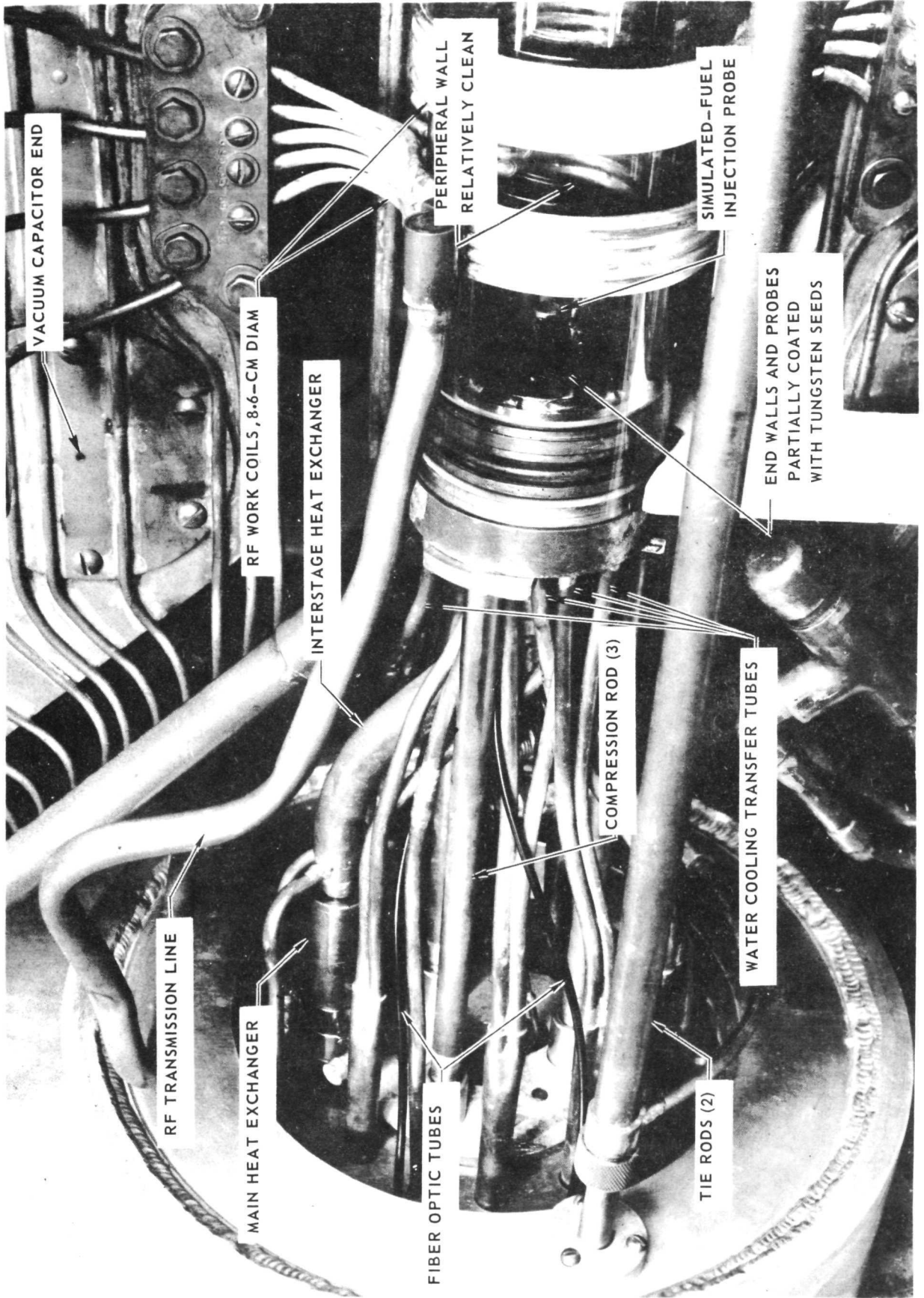


- (c) TESTS WITH MODIFIED PARTICLE FEEDER SYSTEM (FIG. 28)  
AND DEAGGLOMERATOR; TUNGSTEN MASS FLOW  
RATE  $w_W = 0.134$  g/SEC



PHOTOGRAPH OF 7/8-SCALE IRG CONFIGURATION AFTER A TUNGSTEN SIMULATED-FUEL INJECTION TEST AT 30 ATM

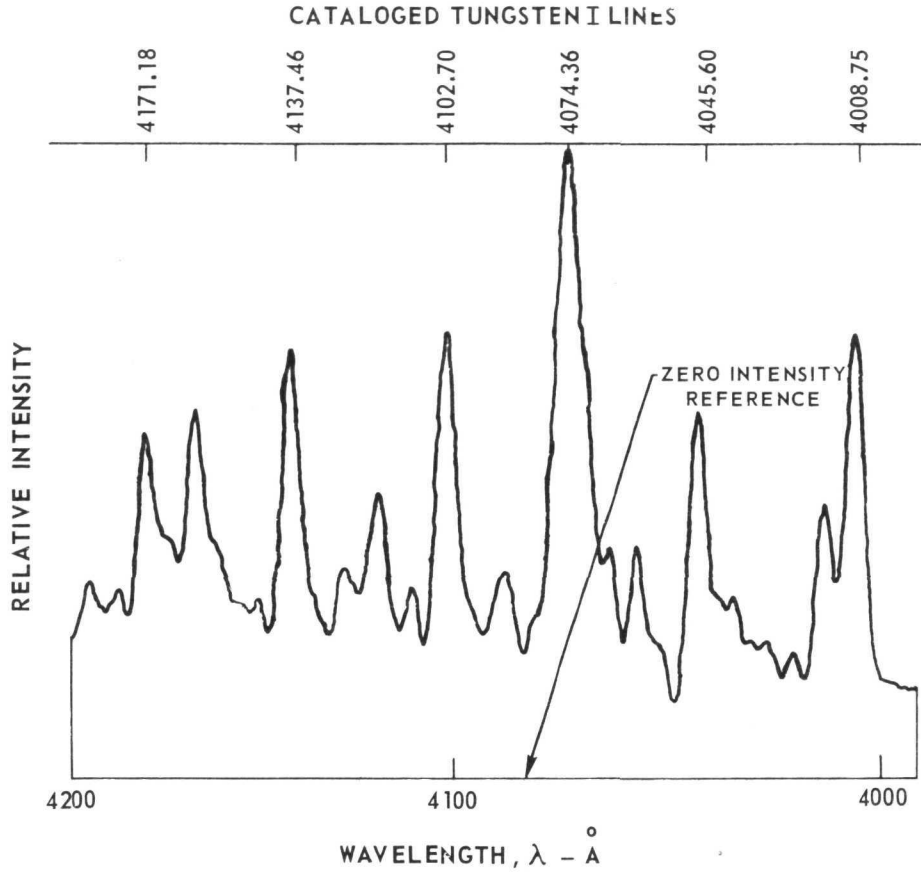
SEE TABLE V FOR TEST CONDITIONS ---- CASE IV



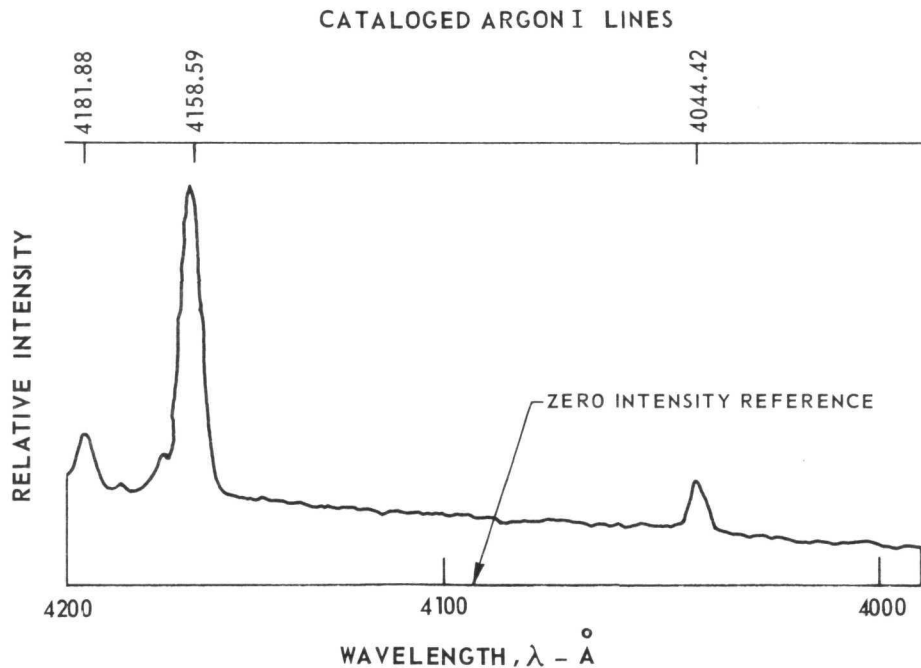
# COMPARISON OF ARGON AND ARGON - TUNGSTEN EMISSION SPECTRA BETWEEN 4000 Å AND 4182 Å OBTAINED DURING SIMULATED-FUEL INJECTION TESTS

SEE TABLE V FOR TEST CONDITIONS - - - CASE III

(a) ARGON-TUNGSTEN



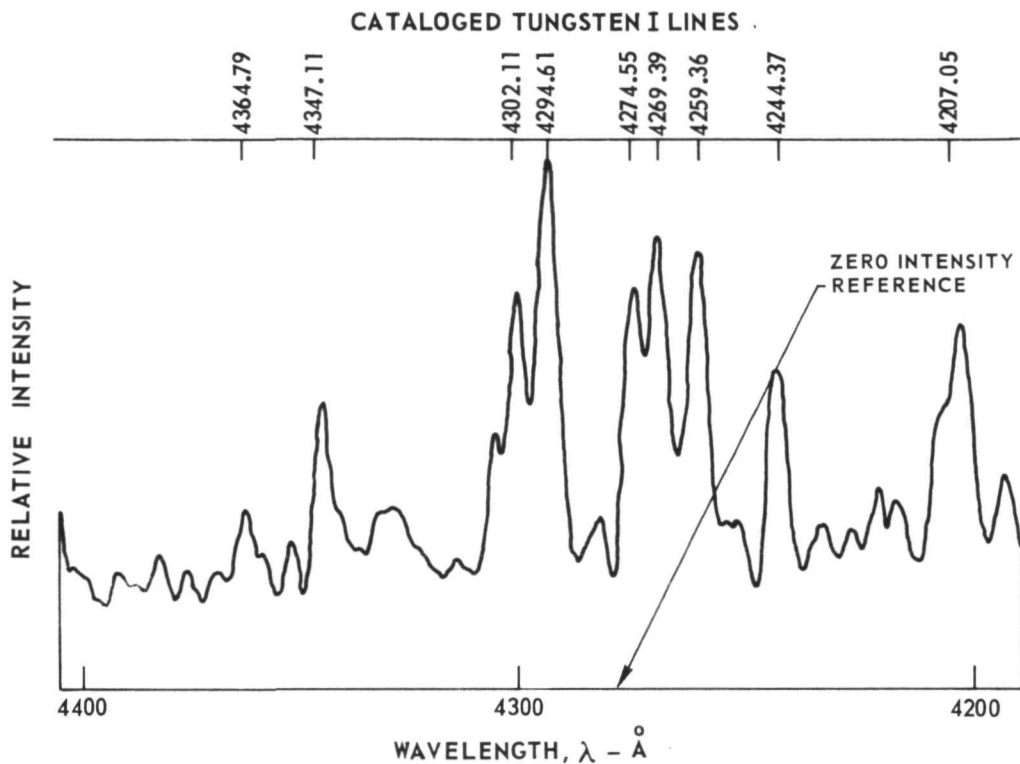
(b) ARGON ONLY



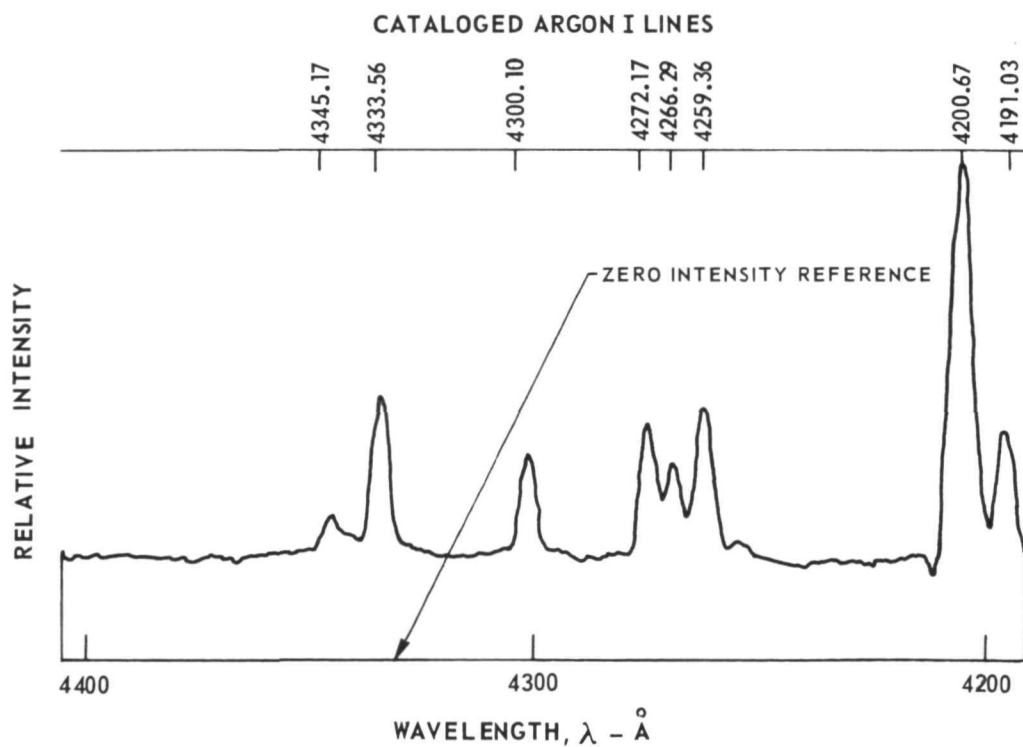
COMPARISON OF ARGON AND ARGON-TUNGSTEN EMISSION SPECTRA BETWEEN 4191 Å AND 4400 Å OBTAINED DURING SIMULATED-FUEL INJECTION TESTS

SEE TABLE V FOR TEST CONDITIONS - - - CASE III

(a) ARGON-TUNGSTEN



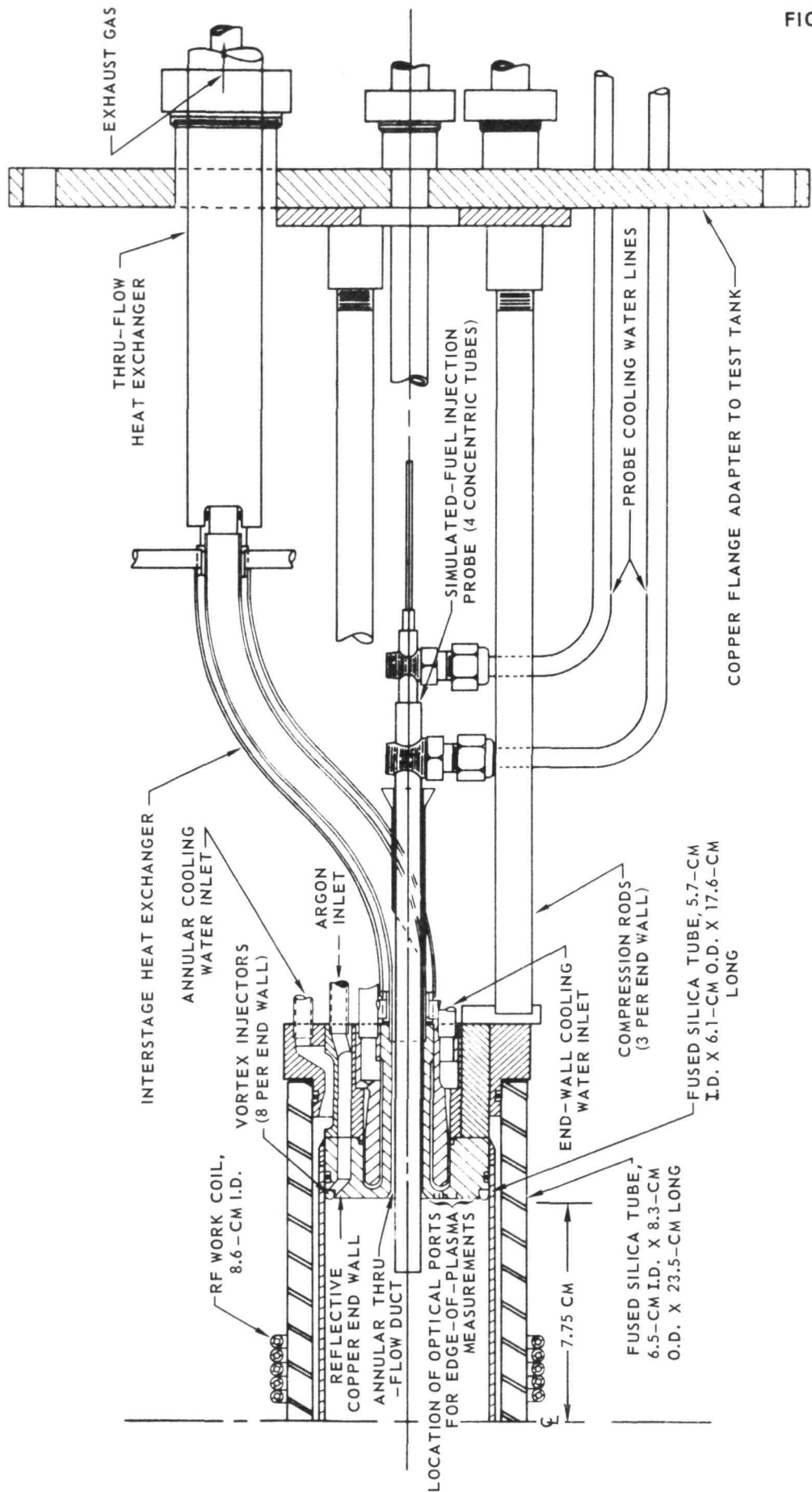
(b) ARGON ONLY



7/8 - SCALE IRG CONFIGURATION USED IN RF PLASMA TESTS WITH UF<sub>6</sub> SIMULATED FUEL

USED AT PRESSURES TO 40 ATM

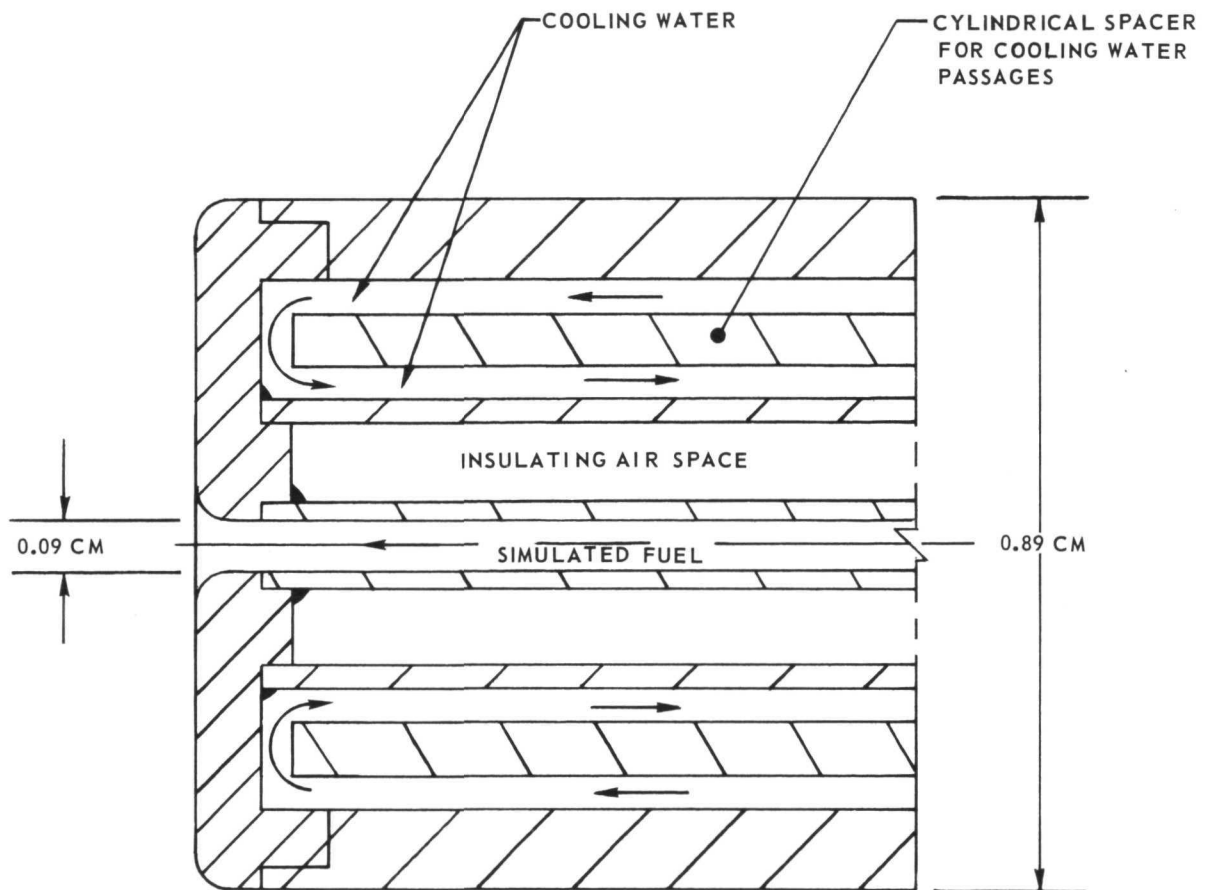
SEE FIG. 35 FOR DETAILS OF PROBE TIP



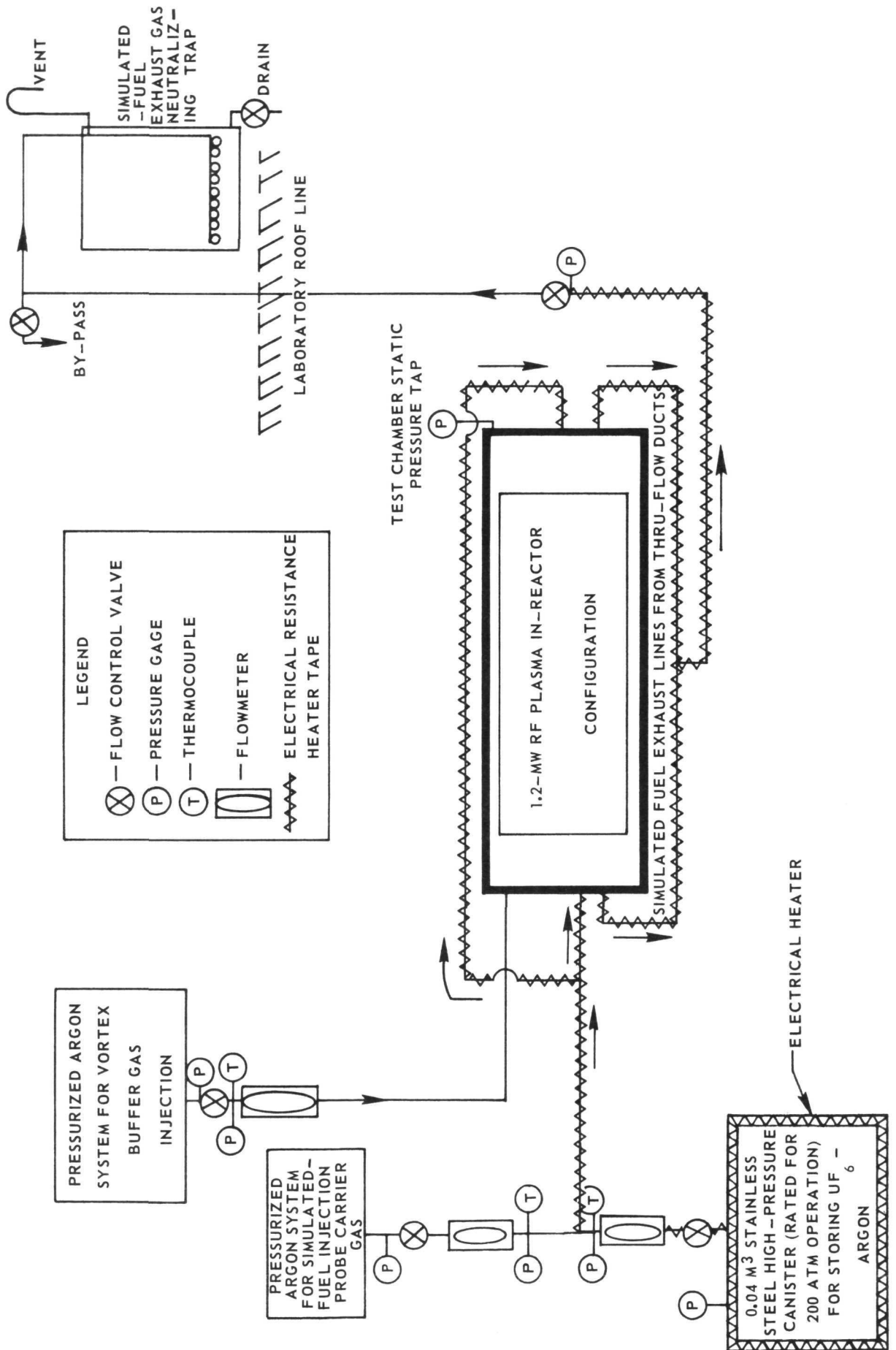
### CROSS-SECTIONAL SKETCH OF TIP OF 4-CONCENTRIC-TUBE SIMULATED-FUEL INJECTION PROBE

USED IN TESTS WITH  $UF_6$  SIMULATED FUEL

SEE FIG. 34 FOR DETAILS OF MODEL CONFIGURATION

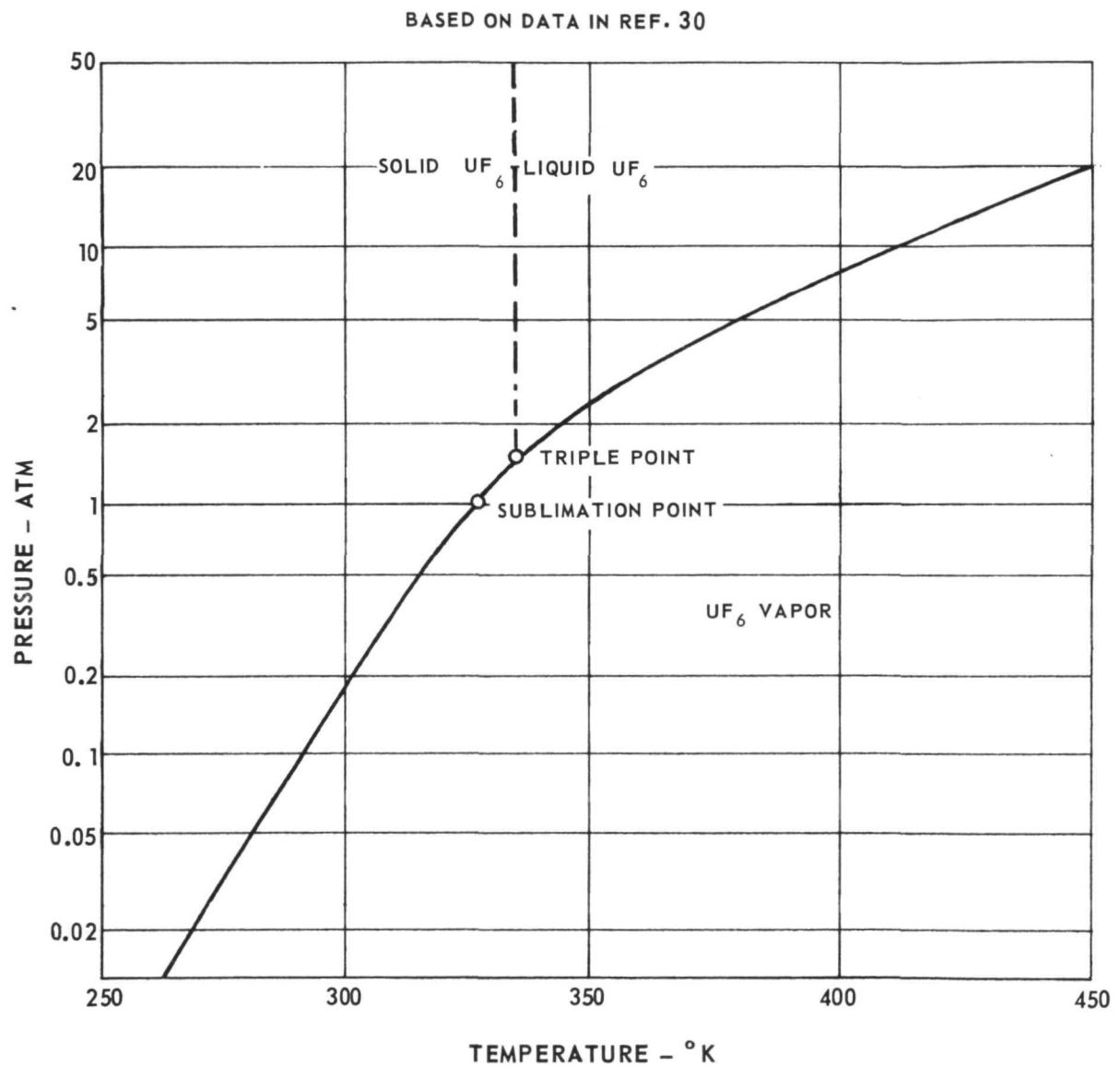


**SCHEMATIC OF FLOW SYSTEM FOR TESTS WITH URANIUM HEXAFLUORIDE  
SIMULATED-FUEL INJECTION**







## VAPOR PRESSURE CURVE FOR URANIUM HEXAFLUORIDE

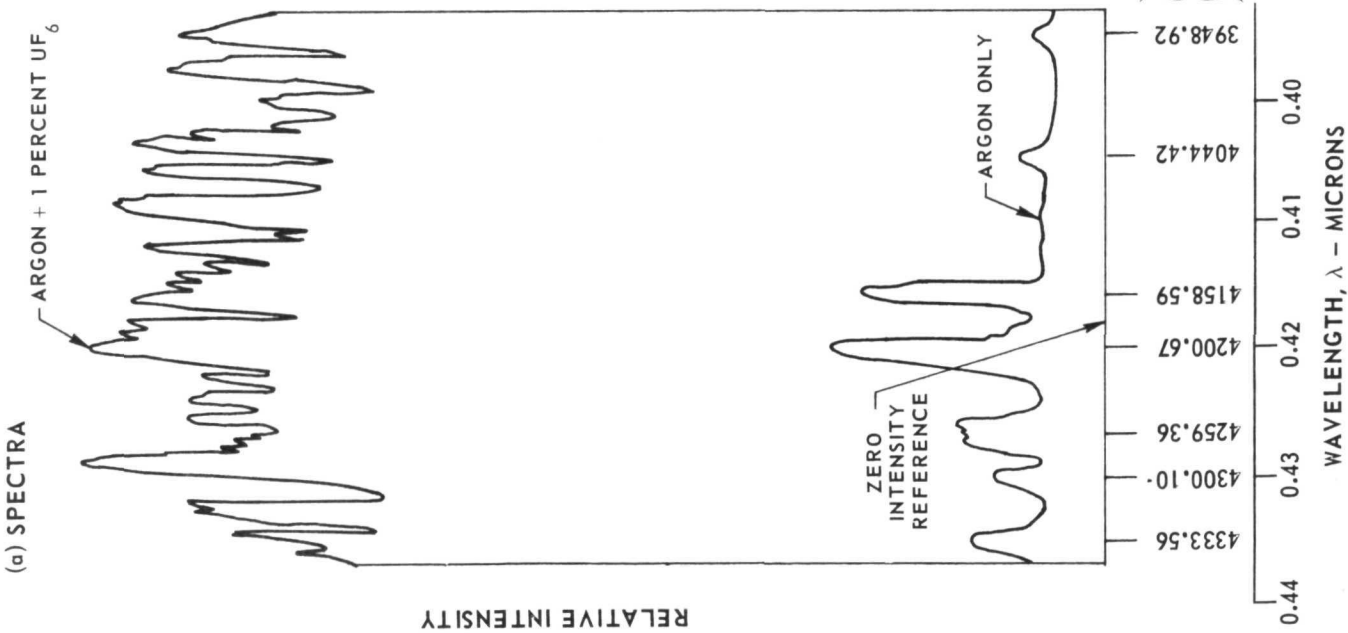
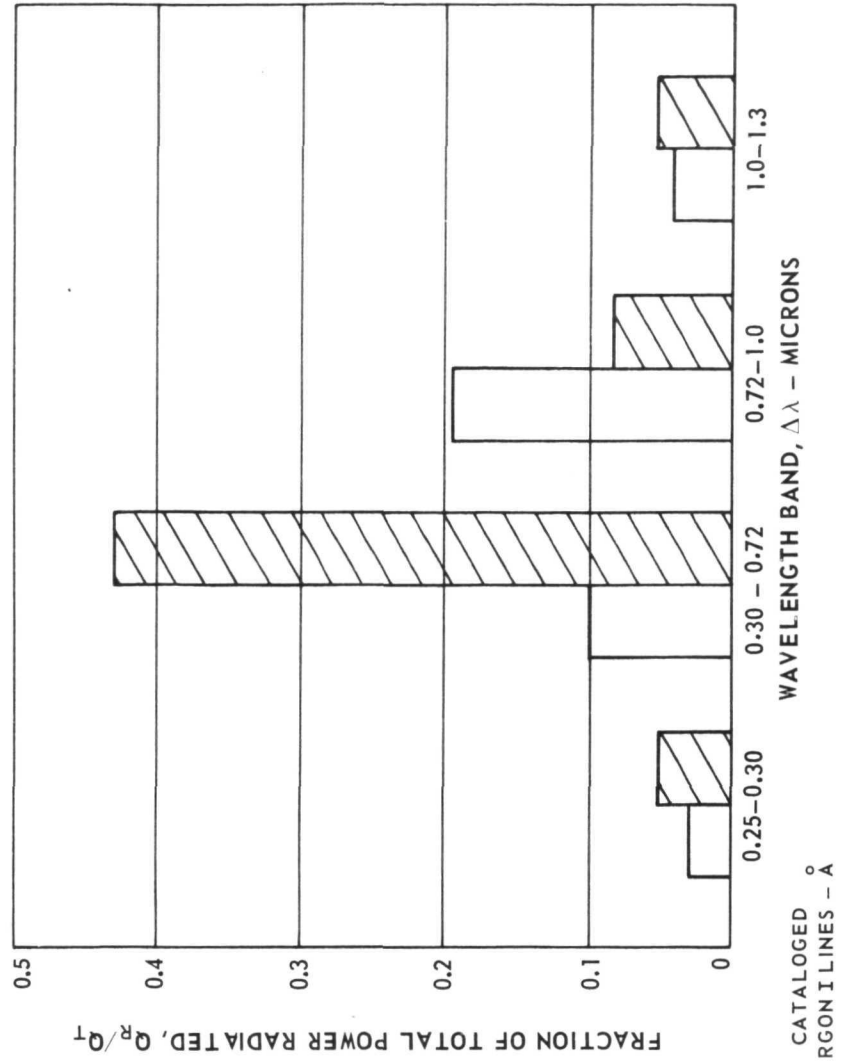


TYPICAL RESULTS OF SPECTRAL-EMISSION AND RADIATION MEASUREMENTS IN TEST WITH 1 PERCENT UF<sub>6</sub> IN ARGON CARRIER GAS AS SIMULATED FUEL

SEE TABLE VI FOR ADDITIONAL TEST CONDITIONS - - - CASE I

KEY	COMPOSITION	F <sub>D</sub> -ATM	Q <sub>T</sub> -KW	W <sub>A</sub> -g/SEC	W <sub>F</sub> -g/SEC
	ARGON PLUS UF <sub>6</sub>	5.0	67	2.7	0.5
	ARGON	4.0	45	2.7	0

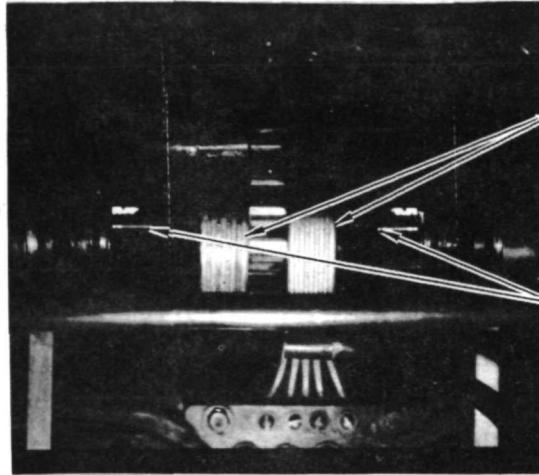
(b) FRACTION OF TOTAL POWER RADIATED IN DIFFERENT WAVELENGTH BANDS



PHOTOGRAPHS OF 7/8-SCALE IRG CONFIGURATION WITH  $UF_6$  SIMULATED-FUEL INJECTION

(a) VIEW THROUGH CENTRAL VIEW PORT WITH NO PLASMA PRESENT

SEE FIG. 34 FOR  
ADDITIONAL DETAILS  
OF TEST CONFIGURATION



RF WORK COILS

EXPOSURE DATA:  
EKTACOLOR-ASA 100  
f/8 AT 1/10 SEC

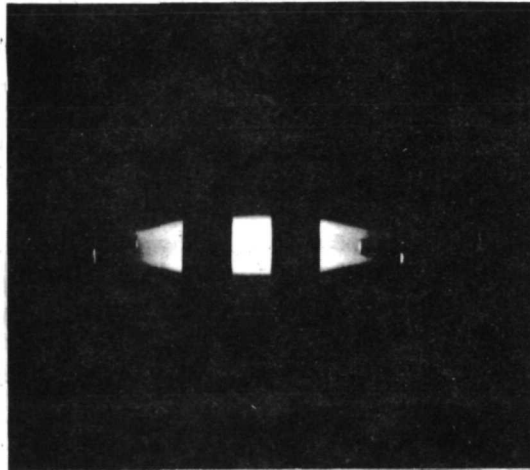
SIMULATED-FUEL  
INJECTION PROBES

(b) WITH ARGON RF PLASMA PRESENT

TEST CONDITIONS:

$Q_T = 46$  KW  
 $P_D = 20$  ATM  
 $W_A = 6.5$  g/SEC  
 $T^* = 2800^\circ$  K

SEE TABLE VI FOR  
ADDITIONAL TEST  
CONDITIONS ---  
CASE III



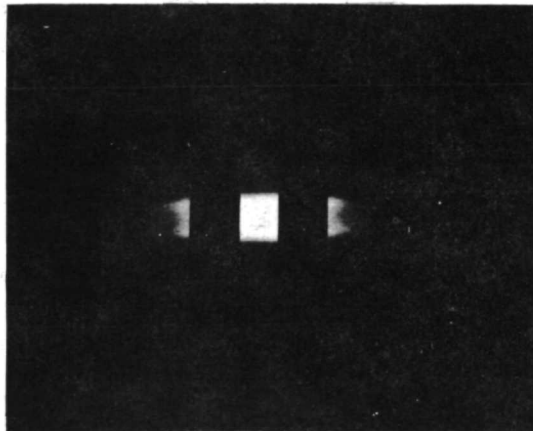
f/16 AT 1/250

(c) WITH 1 PERCENT  $UF_6$  INJECTION

TEST CONDITIONS:

$Q_T = 84$  KW  
 $P_D = 20$  ATM  
 $W_A = 6.5$  g/SEC  
 $T^* = 3380^\circ$  K

SEE TABLE VI FOR  
ADDITIONAL TEST  
CONDITIONS ---  
CASE III

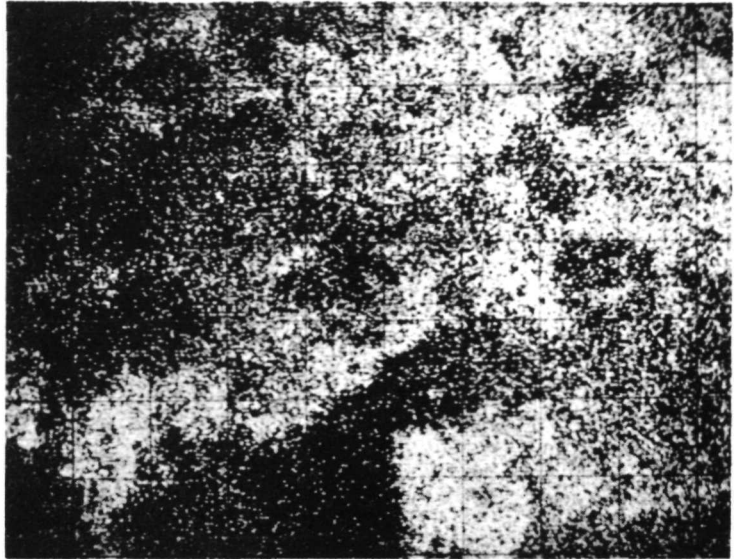


f/32 AT 1/250

PHOTOGRAPHS OF X-RAY DISTRIBUTION FOR U, O AND F ON A CLUSTER OF PARTICLES  
FROM PERIPHERAL-WALL AFTER UF<sub>6</sub> SIMULATED-FUEL INJECTION TEST

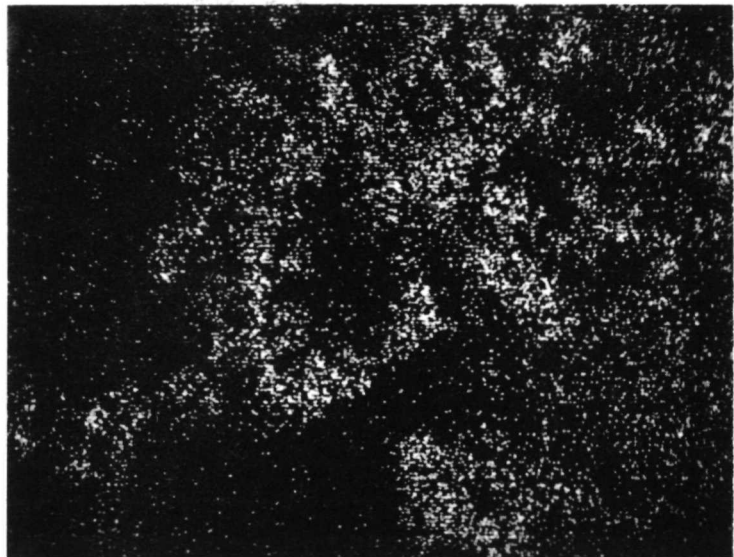
MAGNIFICATION IS 330X

(a) X-RAY SHOWING URANIUM  
(WHITE AREA)

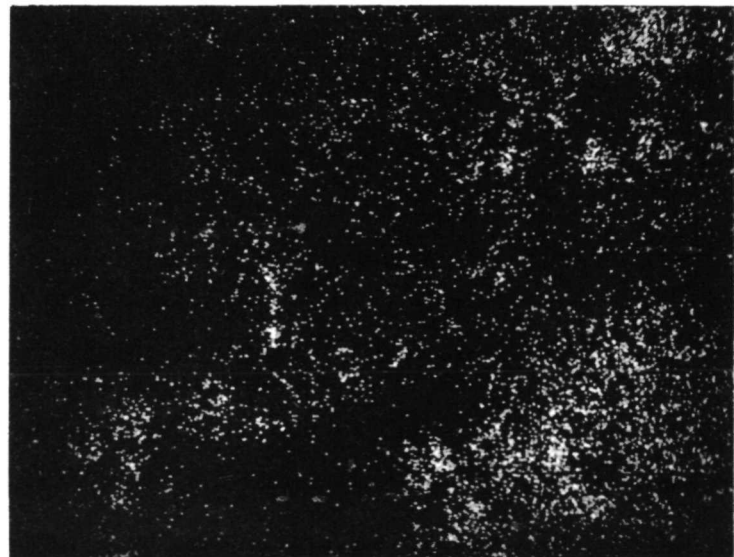


→ | 30 μ | ←

(b) X-RAY SHOWING OXYGEN

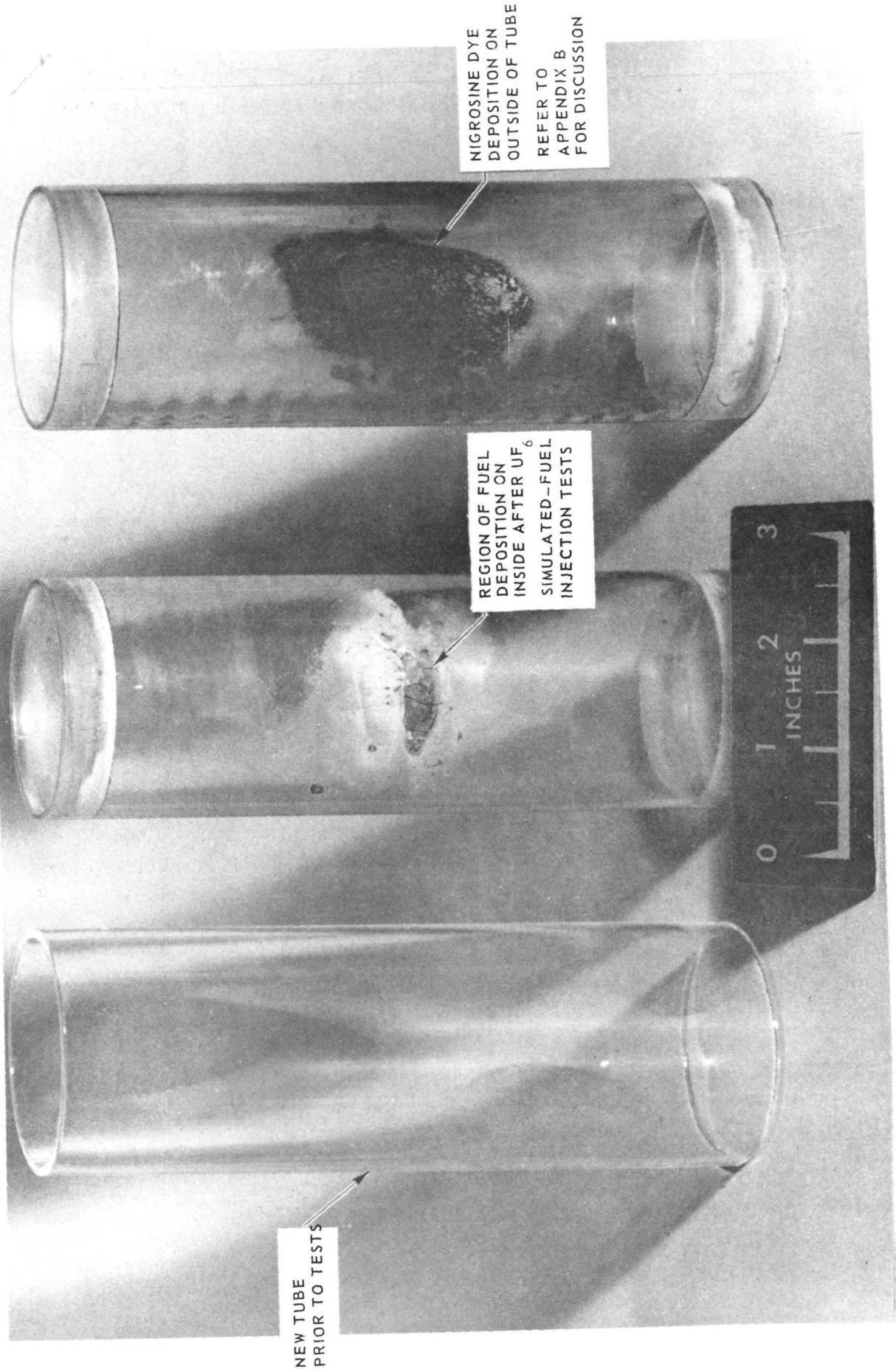


(c) X-RAY SHOWING FLUORINE



# PHOTOGRAPH OF THREE 57-MM-I.D. FUSED SILICA TUBES USED IN SIMULATED - FUEL INJECTION TESTS

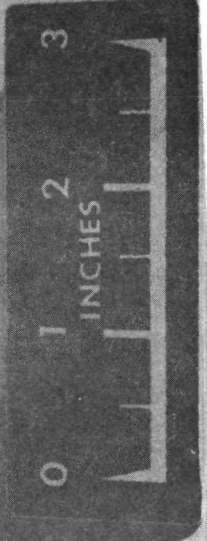
PHOTOS SHOW SIMULATED-FUEL DEPOSITION AFTER INITIAL TESTS AT HIGH BUFFER GAS INJECTION VELOCITIES AND DEPOSITION CAUSED BY DYE DETERIORATION DUE TO UV ABSORPTION



NEW TUBE  
PRIOR TO TESTS

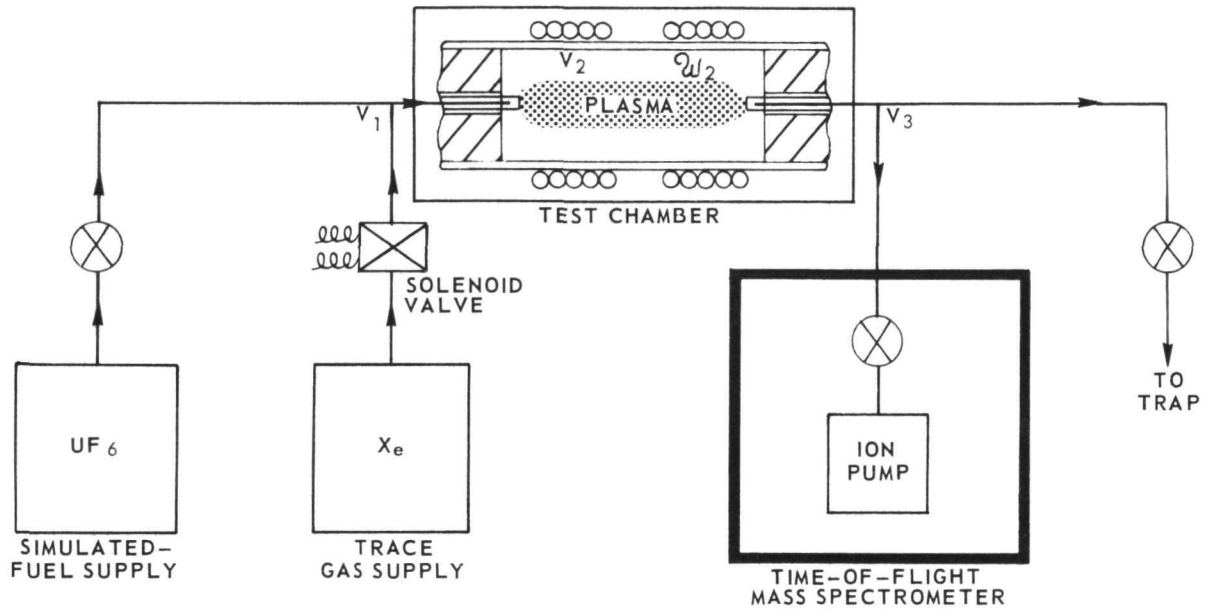
REGION OF FUEL  
DEPOSITION ON  
INSIDE AFTER U<sub>6</sub>  
SIMULATED-FUEL  
INJECTION TESTS

NIGROSINE DYE  
DEPOSITION ON  
OUTSIDE OF TUBE  
REFER TO  
APPENDIX B  
FOR DISCUSSION



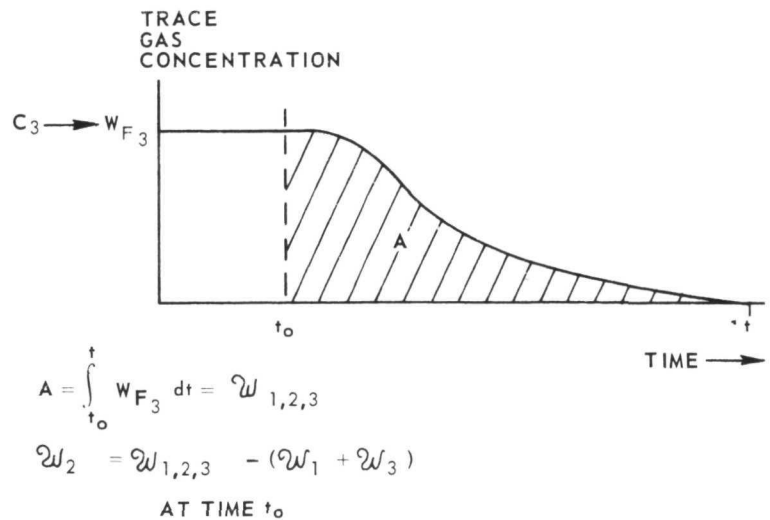
### SCHEMATIC OF TIME-OF-FLIGHT MASS SPECTROMETER SYSTEM FOR MEASURING SIMULATED-FUEL CONTAINED

MODEL CONFIGURATION SAME AS SHOWN IN FIG. 34

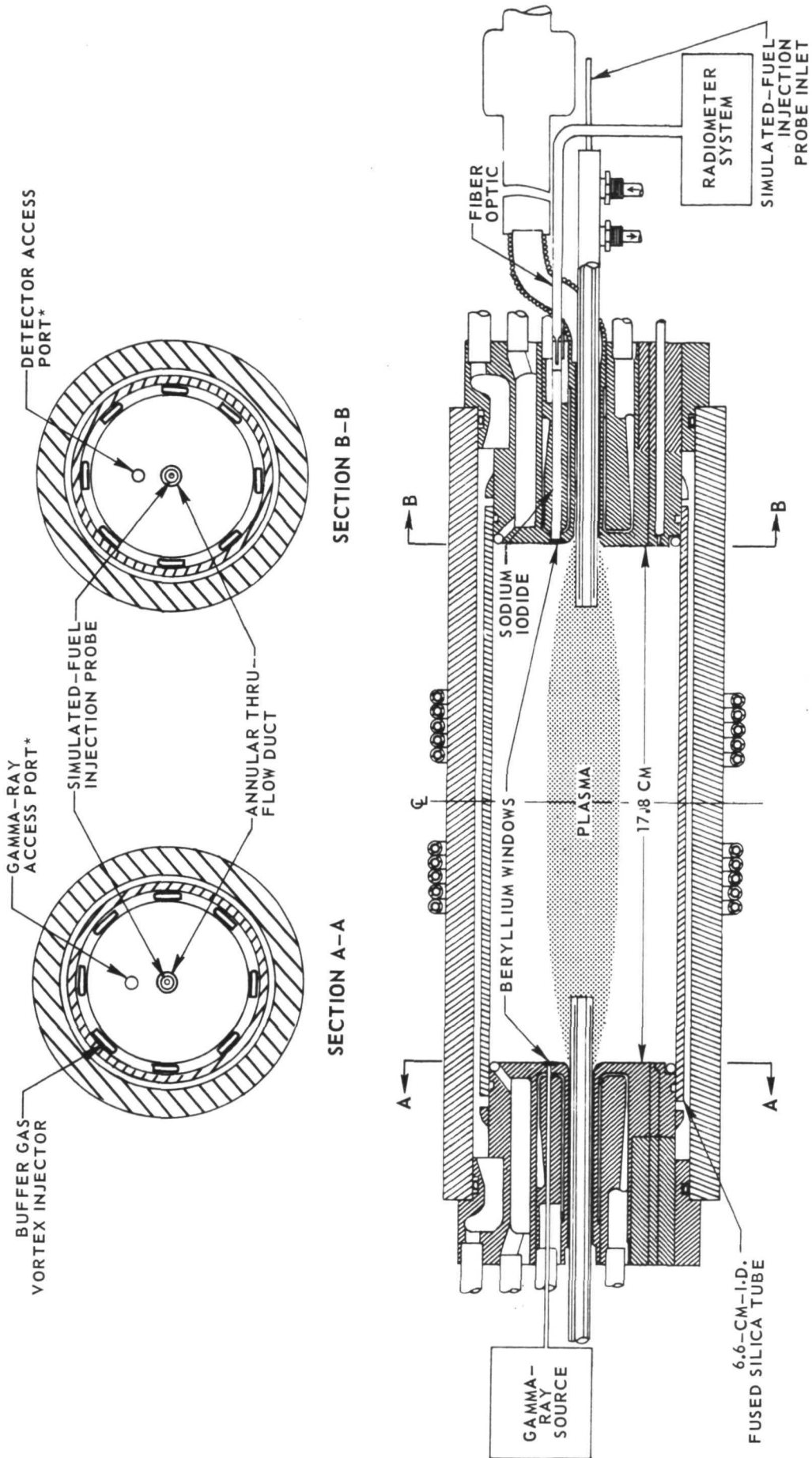


TYPICAL OUTPUT OF MASS SPECTROMETER

SYMBOL	EXPLANATION
SUBSCRIPT 1	SIMULATED FUEL INLET SYSTEM
SUBSCRIPT 2	PLASMA CHAMBER
SUBSCRIPT 3	TEST CHAMBER EXHAUST SYSTEM
V	VOLUME, CM <sup>3</sup>
W	AMOUNT OF SIMULATED FUEL, g
C	CONCENTRATION OF TRACE GAS, PPM
W <sub>F</sub>	SIMULATED FUEL FLOW RATE, g/SEC
t <sub>0</sub>	TIME AT WHICH TRACE GAS IS SHUT OFF, SEC
t	TIME AT WHICH NO TRACE GAS IS MEASURED, SEC
A	AREA UNDER SHADED PORTION OF CURVE



SKETCH OF 40 ATM CONFIGURATION USING  
GAMMA-RAY ABSORPTION METHOD FOR DETERMINING  
SIMULATED-FUEL CONTAINMENT



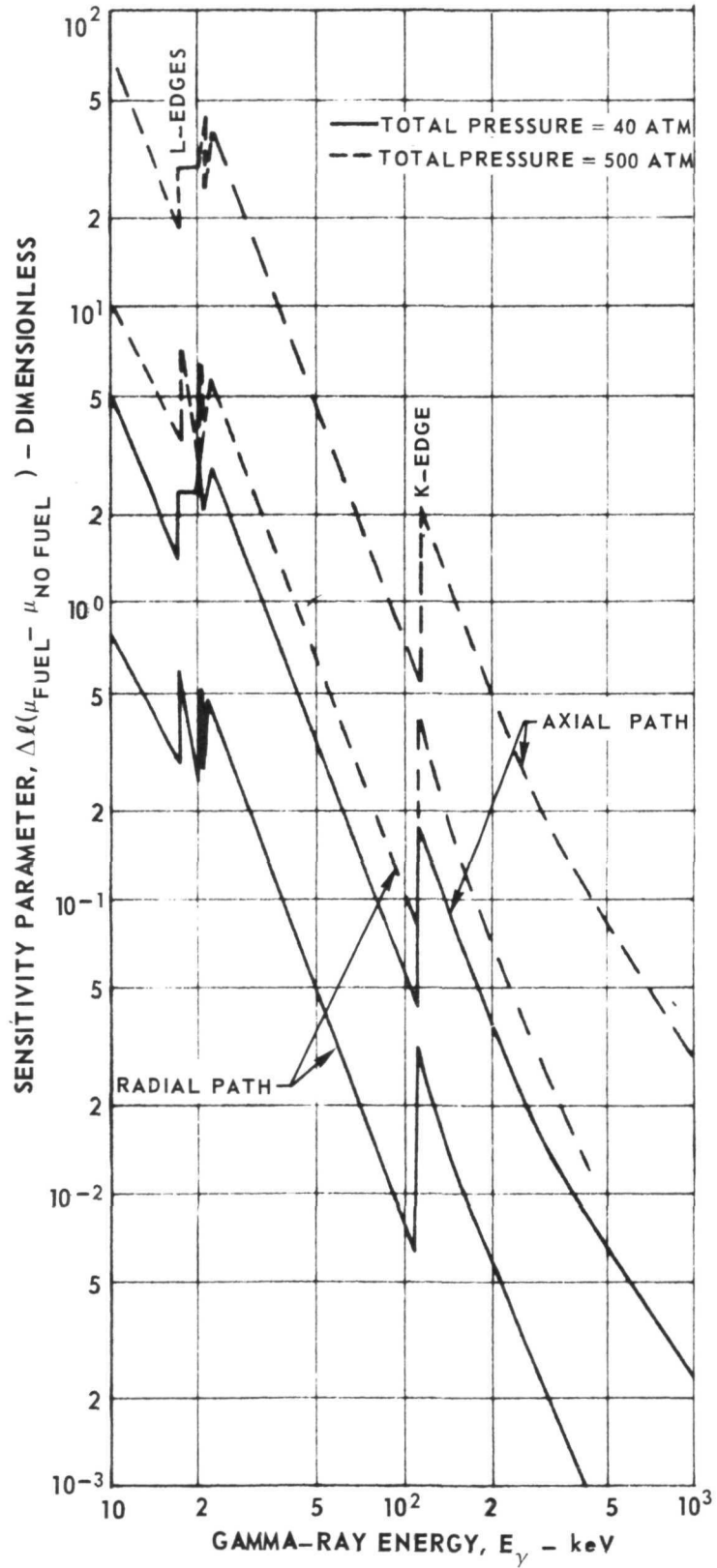
\*FOR SIMPLICITY ONLY ONE OF SEVERAL END WALL ACCESS PORTS  
LOCATED AT DIFFERENT RADII IS SHOWN



### VARIATION OF GAMMA-RAY ABSORPTION SENSITIVITY TO URANIUM FUEL WITH GAMMA-RAY ENERGY

SEE FIG. 43 FOR DETAILS OF TEST CONFIGURATION

$$\bar{\rho}_F / \rho_{B_6} = 0.7 \quad r_6 / r_1 = 0.5 \quad \rho_{B_6} = 3.2 \times 10^{-3} \text{ g/CM}^3 \quad r_1 = 3.3 \text{ CM}$$

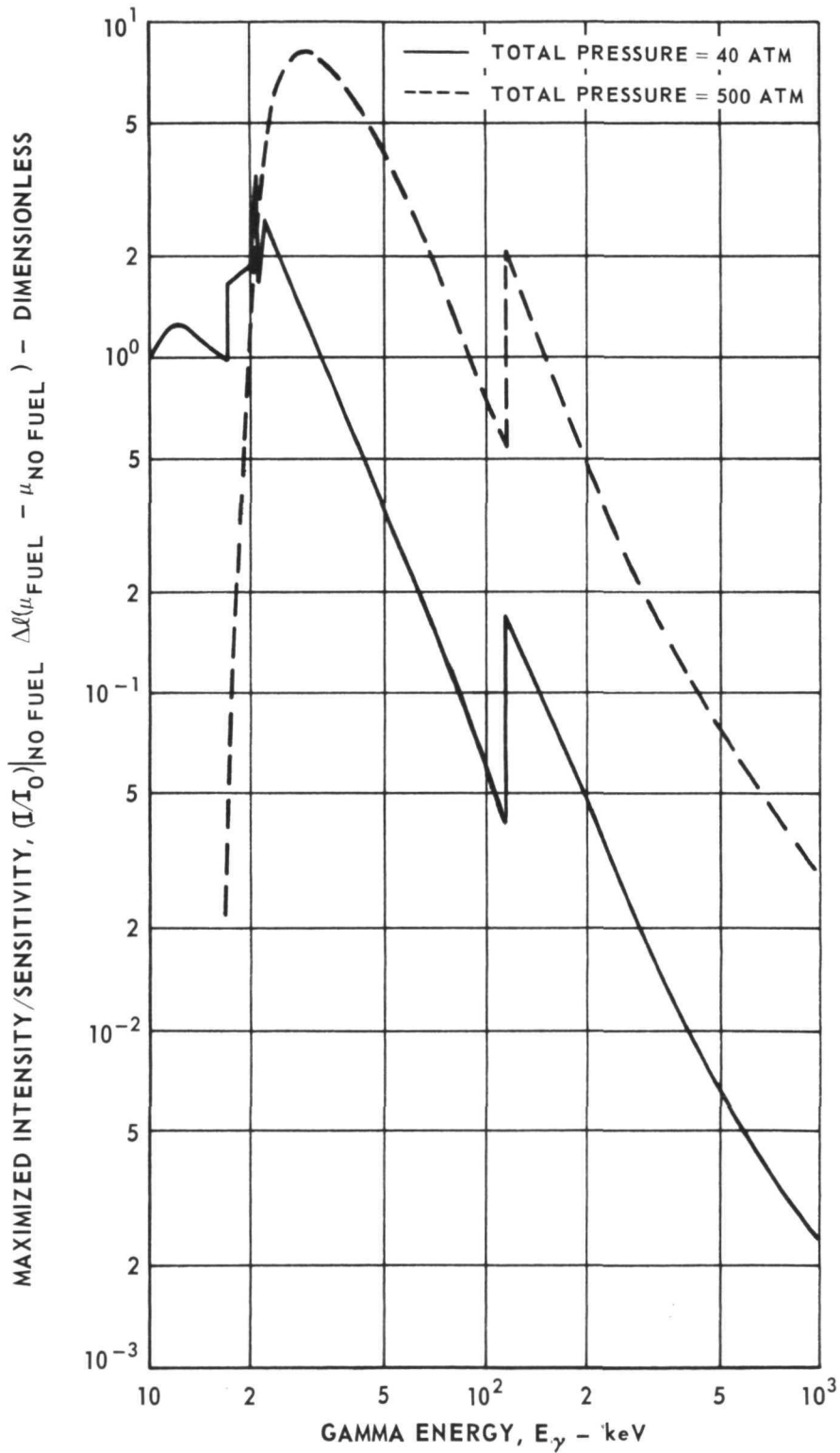




### VARIATION OF MAXIMIZED SOURCE BEAM INTENSITY/SENSITIVITY WITH GAMMA-RAY ENERGY

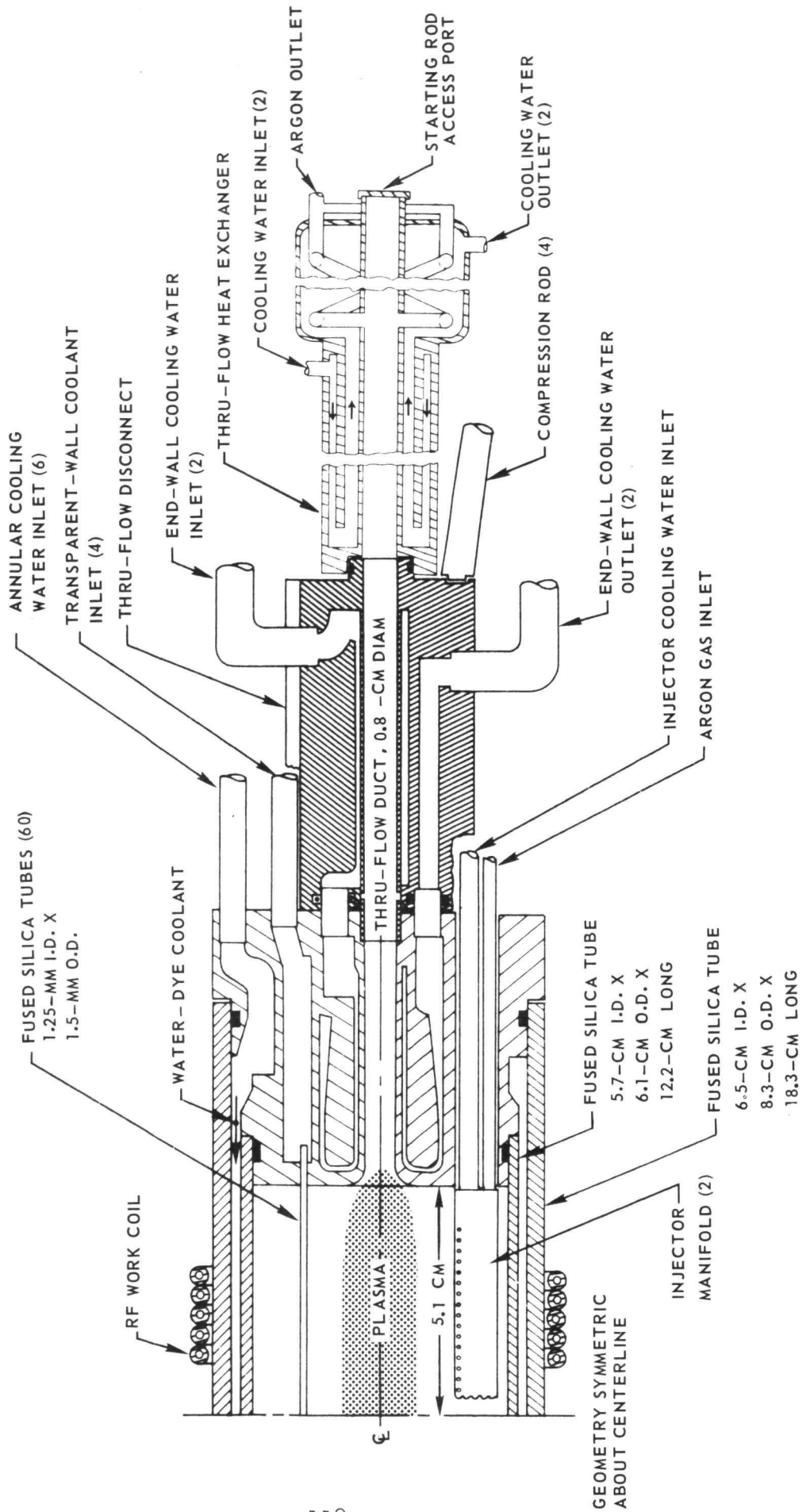
SEE FIG. 43 FOR DETAILS OF TEST CONFIGURATION

$\bar{\rho}_F / \rho_{B_6} = 0.7$        $r_6 / r_1 = 0.5$        $\rho_{B_6} = 3.2 \times 10^{-3} \text{ g/CM}^3$        $r_1 = 3.3 \text{ CM}$



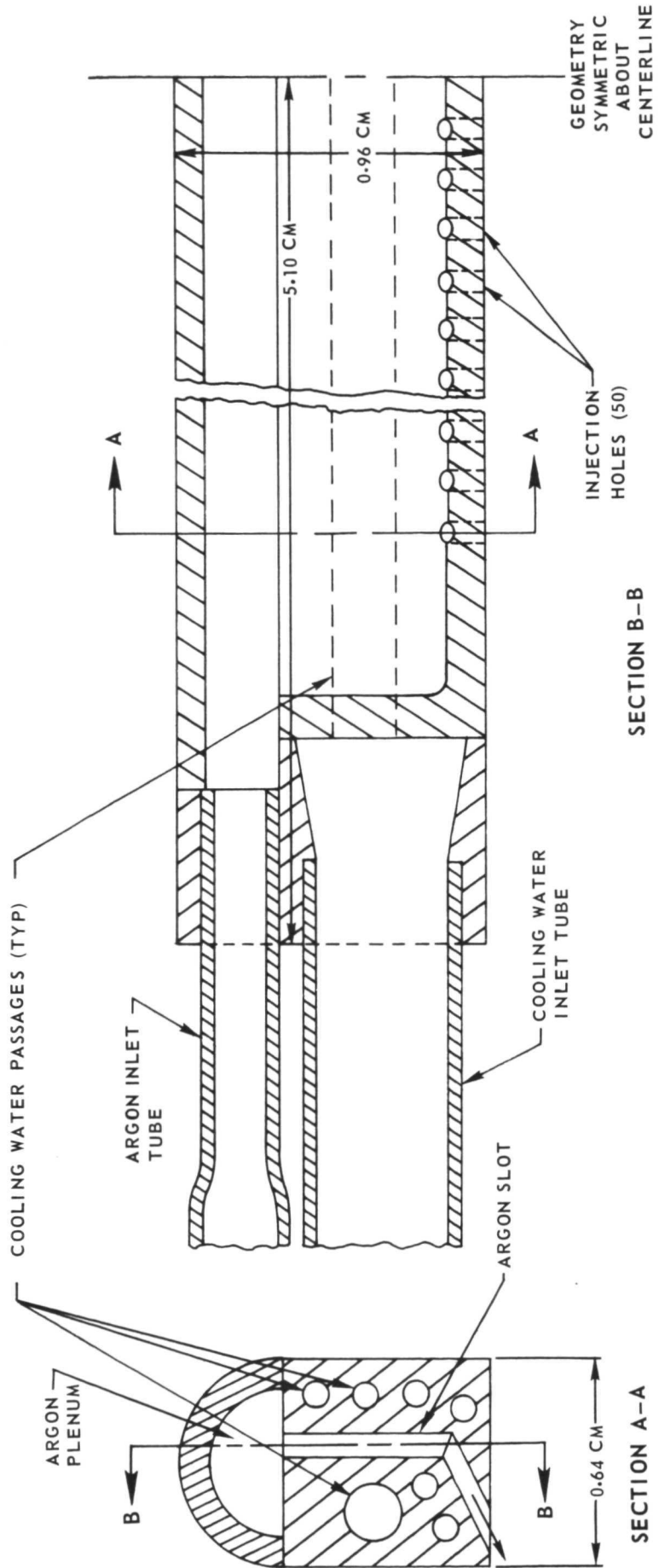
SKETCH OF TRANSPARENT-WALL MODEL CONFIGURATION  
USED IN RF PLASMA TESTS

SEE FIG. 47 FOR SKETCH OF INJECTOR MANIFOLD



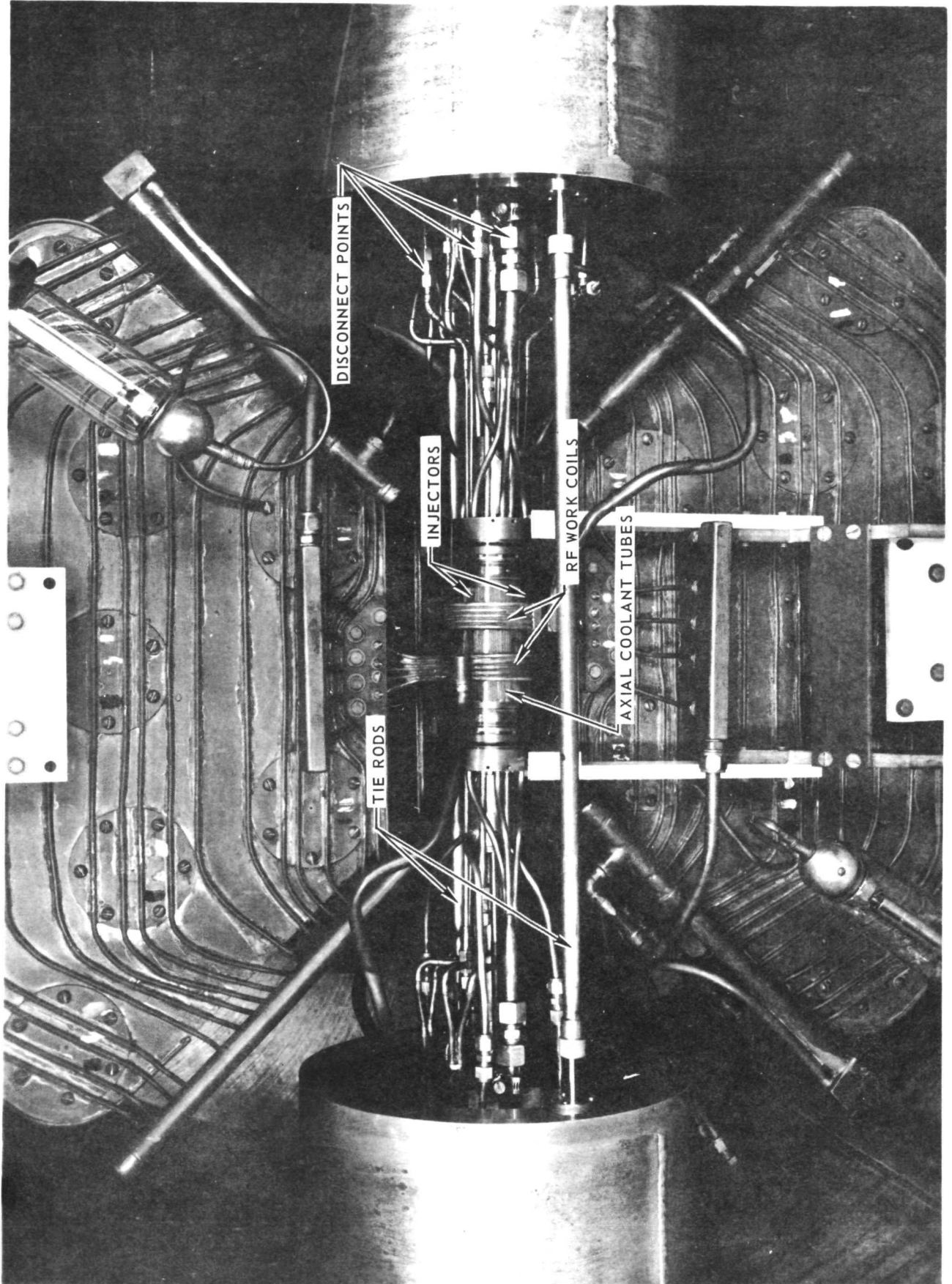
# GEOMETRY OF PERIPHERAL-WALL ARGON INJECTOR MANIFOLD FOR TRANSPARENT-WALL MODEL

SEE FIG. 46 FOR DETAILS OF ENTIRE MODEL CONFIGURATION



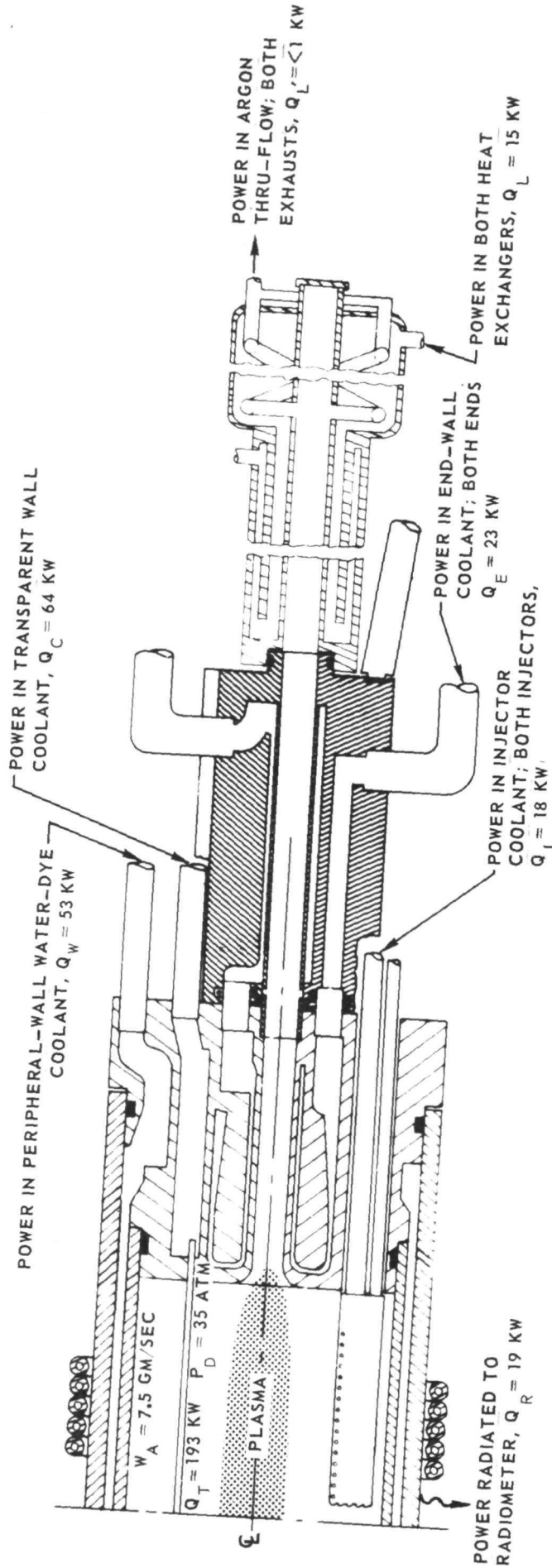
PHOTOGRAPH SHOWING TRANSPARENT-WALL MODEL INSTALLED IN 1:2-MW RF INDUCTION HEATER

SEE FIG. 46 FOR DETAILS OF TEST CONFIGURATION



SKETCH OF TRANSPARENT-WALL MODEL SHOWING POWER BREAKDOWN FOR HIGHEST-POWER/HIGHEST-PRESSURE OPERATING POINT

SEE FIG. 46 FOR DETAILS OF MODEL CONFIGURATION



TOTAL DC INPUT POWER,  $Q_I = 590 \text{ KW}$  AT 5.4824 MHz

TOTAL DISCHARGE POWER,  $Q_T = 193 \text{ KW}$

TOTAL POWER RADIATED THROUGH MODEL WALL,  $Q_R + Q_W = 72 \text{ KW}$

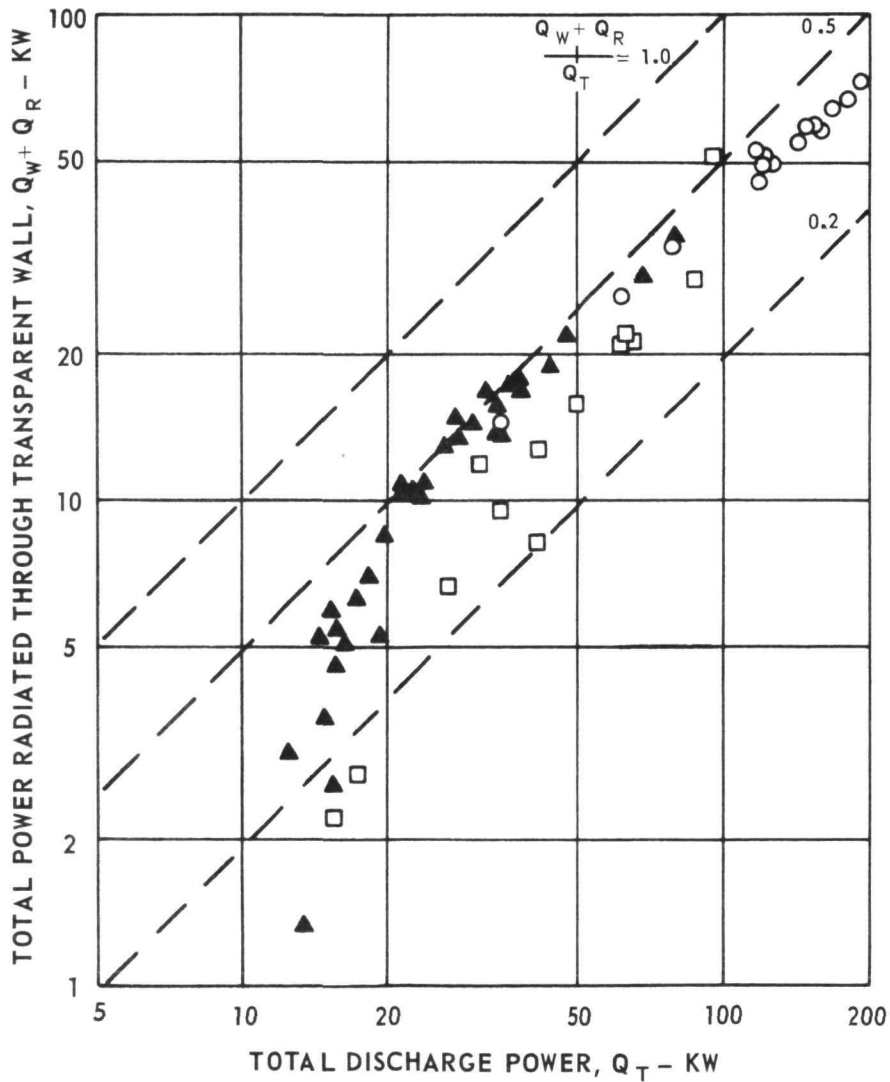
RADIANT ENERGY FLUX MODEL WALL,  $Q_{R,T}/A_M = 1.4 \text{ KW/CM}^2$

FIG. 49

VARIATION OF POWER RADIATED THROUGH AXIAL-COOLANT TUBES WITH TOTAL DISCHARGE POWER IN TRANSPARENT-WALL MODEL TESTS

SEE FIG. 46 FOR DETAILS OF MODEL CONFIGURATION

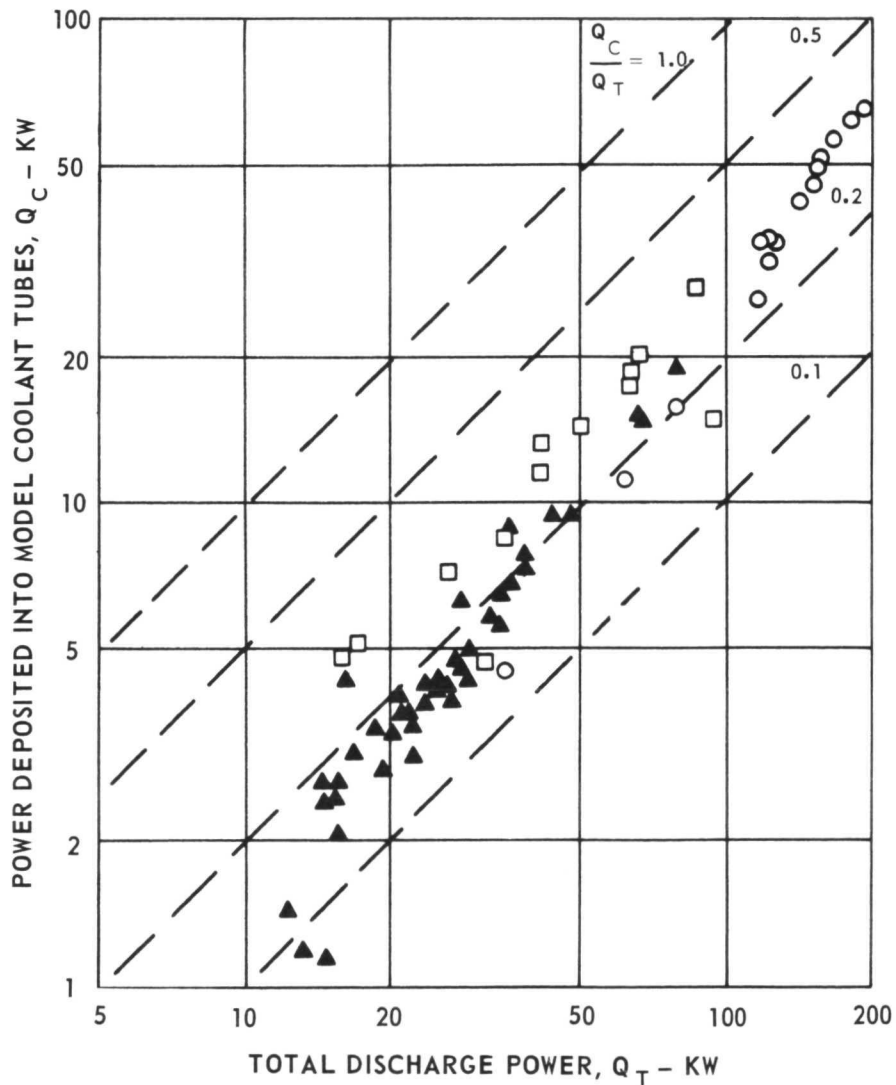
SYMBOL	TRANSPARENT WALL THICKNESS, CM	CHAMBER PRESSURE, $P_D$ - ATM	ARGON FLOW RATE $W_A$ - g/SEC	DATA FROM
○	0.0125	7-35	4.5-8.1	PRESENT PROGRAM
□	0.025	1-16.6	2.3-8.1	PRESENT PROGRAM
▲	0.0125	1-21	1.8-7.7	REF. 16



VARIATION OF POWER DEPOSITED IN AXIAL-COOLANT TUBES WITH TOTAL DISCHARGE POWER IN TRANSPARENT-WALL MODEL TESTS

SEE FIG. 46 FOR DETAILS OF MODEL CONFIGURATION

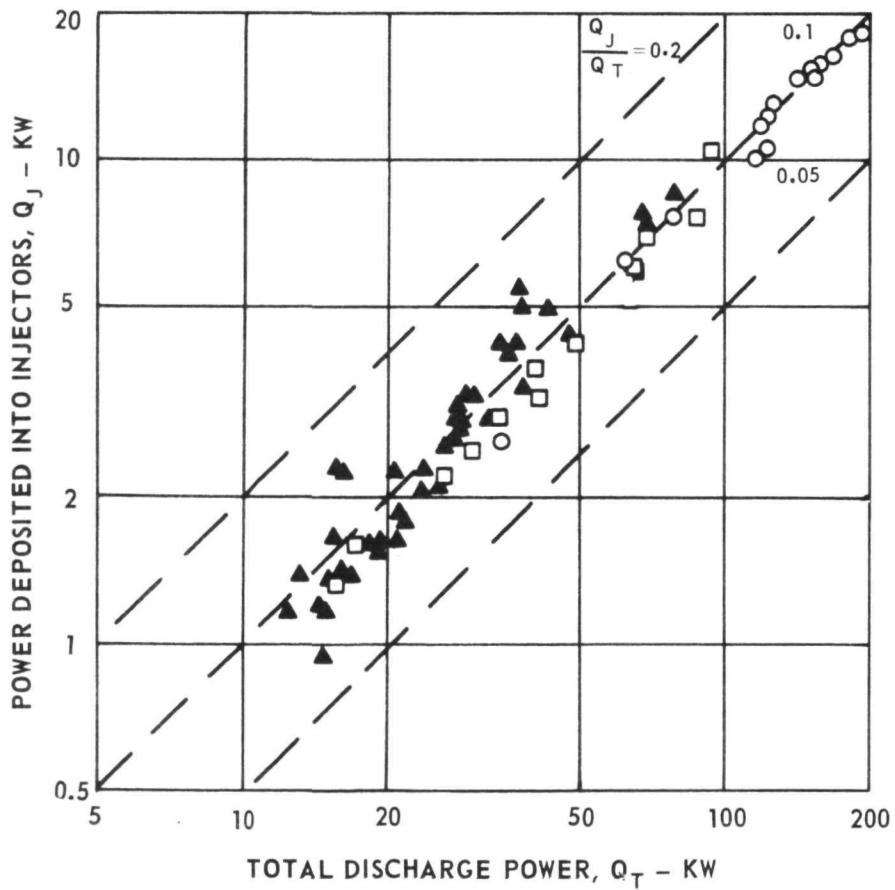
SYMBOL	TRANSPARENT WALL THICKNESS, CM	CHAMBER PRESSURE, $P_D$ - ATM	ARGON FLOW RATE, $W_A$ - g/SEC	DATA FROM
○	0.0125	7-35	4.5-8.1	PRESENT PROGRAM
□	0.025	1-16.6	2.3-8.1	PRESENT PROGRAM
▲	0.0125	1-21	1.8-7.7	REF. 16



### VARIATION OF POWER DEPOSITED INTO INJECTORS WITH TOTAL DISCHARGE POWER IN TRANSPARENT-WALL MODEL TESTS

SEE FIG. 46 FOR DETAILS OF MODEL CONFIGURATION

SYMBOL	TRANSPARENT WALL THICKNESS, CM	CHAMBER PRESSURE, P <sub>D</sub> - ATM	ARGON FLOW RATE W <sub>A</sub> - g/SEC	DATA FROM
○	0.0125	7-35	4.5-8.1	PRESENT PROGRAM
□	0.025	1-16.6	2.3-8.1	PRESENT PROGRAM
▲	0.0125	1-21	1.8-7.7	REF. 16

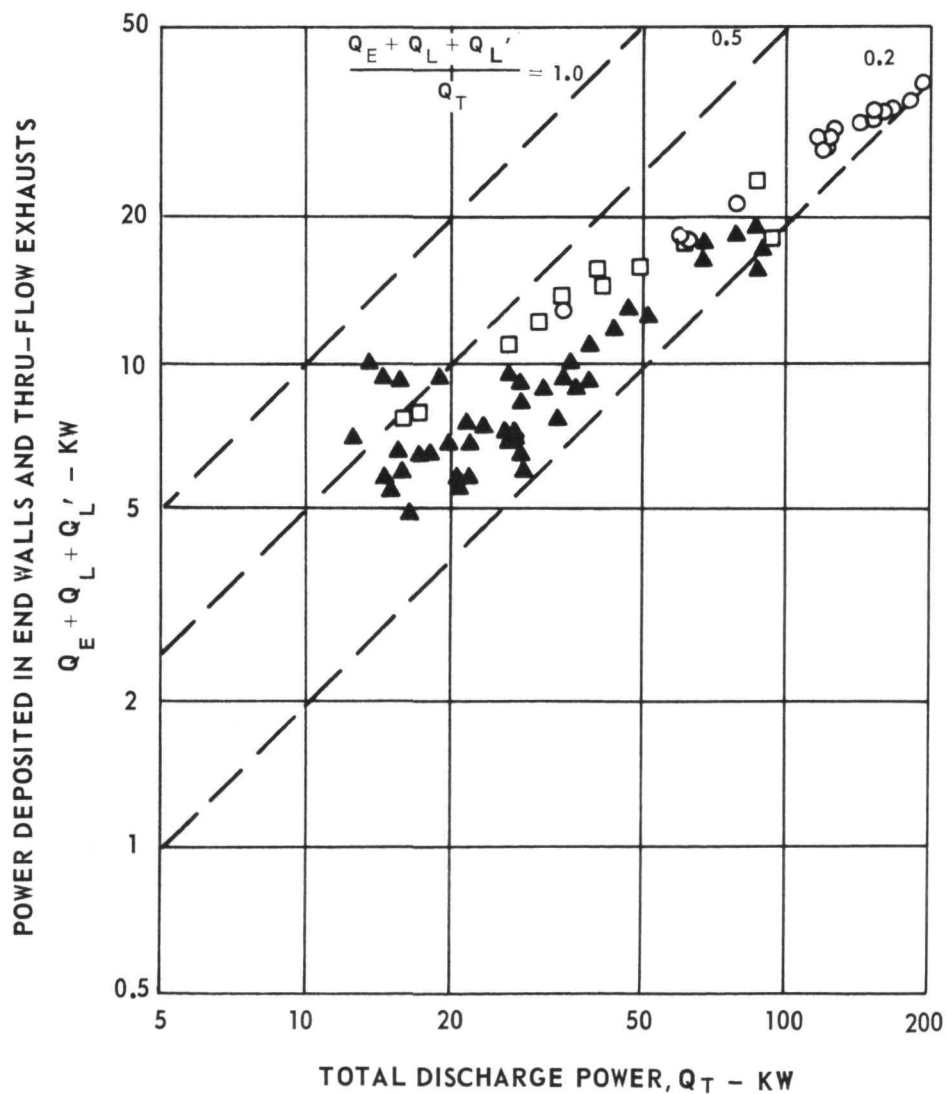




### VARIATION OF POWER DEPOSITED IN END WALLS AND THRU-FLOW EXHAUSTS WITH TOTAL DISCHARGE POWER IN TRANSPARENT-WALL MODEL TESTS

SEE FIG. 46 FOR DETAILS OF MODEL CONFIGURATION

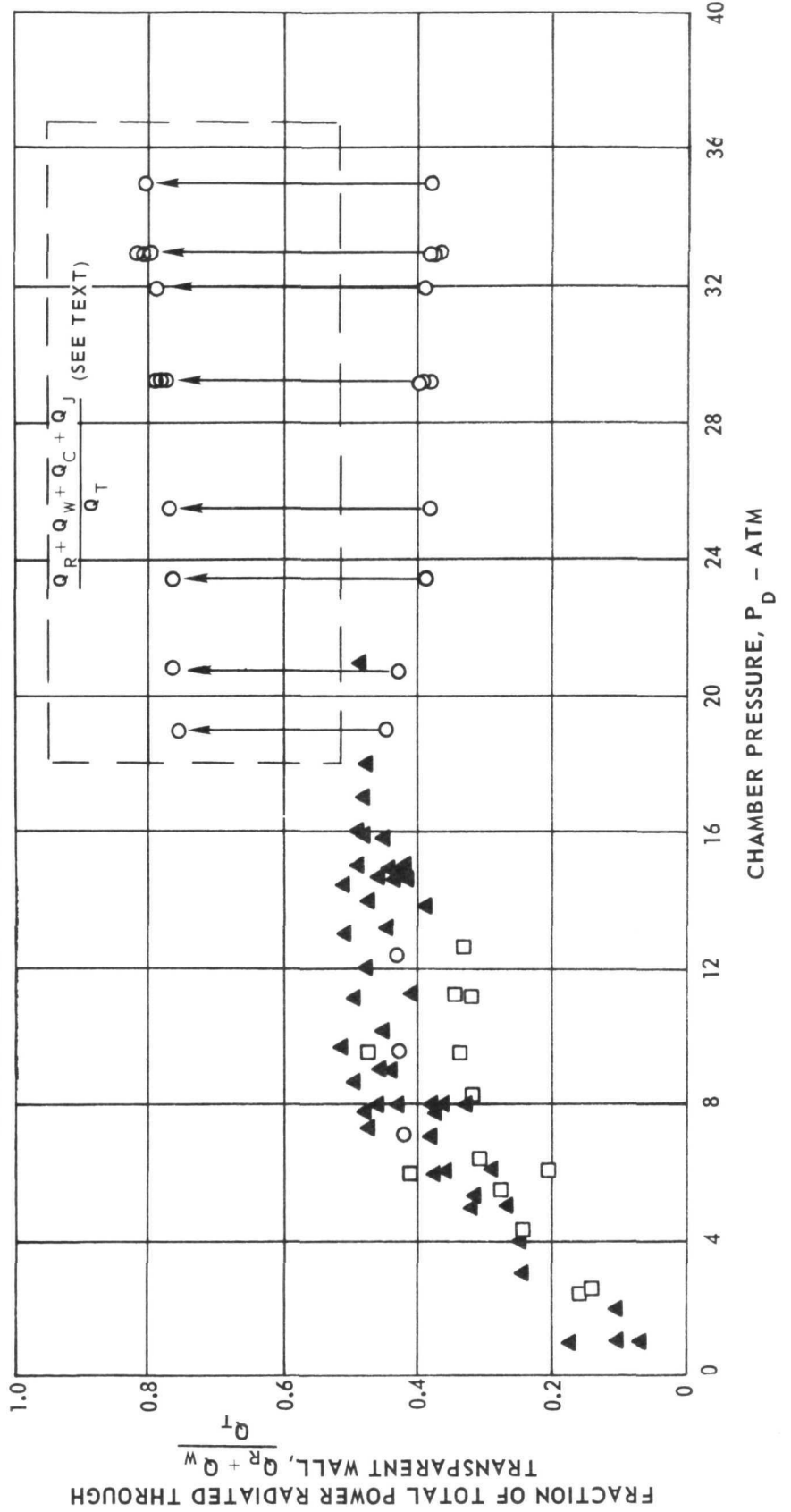
SYMBOL	TRANSPARENT WALL THICKNESS, CM	CHAMBER PRESSURE, $P_D$ - ATM	ARGON FLOW RATE, $W_A$ - g/SEC	DATA FROM
○	0.0125	7-35	4.5-8.1	PRESENT PROGRAM
□	0.025	1-16.6	2.3-8.1	PRESENT PROGRAM
▲	0.0125	1.8-7.7	REF 16	



EFFECT OF CHAMBER PRESSURE ON THE FRACTION OF TOTAL DISCHARGE POWER RADIATED THROUGH INNER PERIPHERAL-WALL IN TRANSPARENT-WALL MODEL TESTS

SEE FIG. 46 FOR DETAILS OF MODEL CONFIGURATION

SYMBOL	TRANSPARENT WALL THICKNESS, CM	TOTAL DISCHARGE POWER $Q_T$ - KW	ARGON FLOW RATE, $W_A$ - g/SEC	DATA FROM
○	0.0125	34.2-193.0	4.5-8.1	PRESENT PROGRAM
□	0.025	15.7-93.9	2.3-8.1	PRESENT PROGRAM
▲	0.0125	5.0-80.0	1.8-7.7	REF. 16

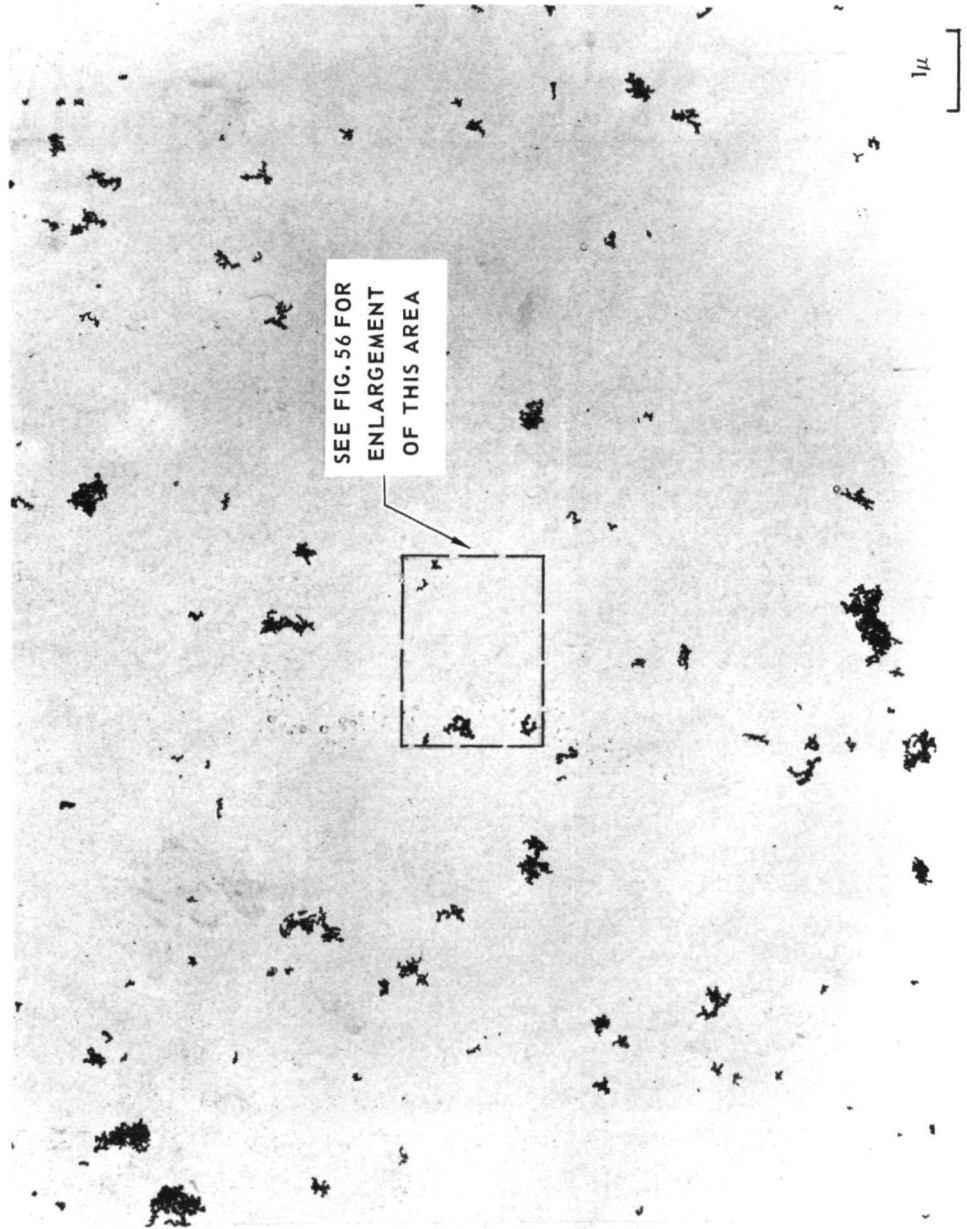


ELECTRON PHOTOMICROGRAPH OF TUNGSTEN PARTICLES COLLECTED ON GRID  
AFTER DISCHARGE FROM PARTICLE FEEDER SYSTEM

SEE FIG. 27 FOR SCHEMATIC OF PARTICLE FEEDER SYSTEM

MAGNIFICATION -  $9.6 \times 10^2$

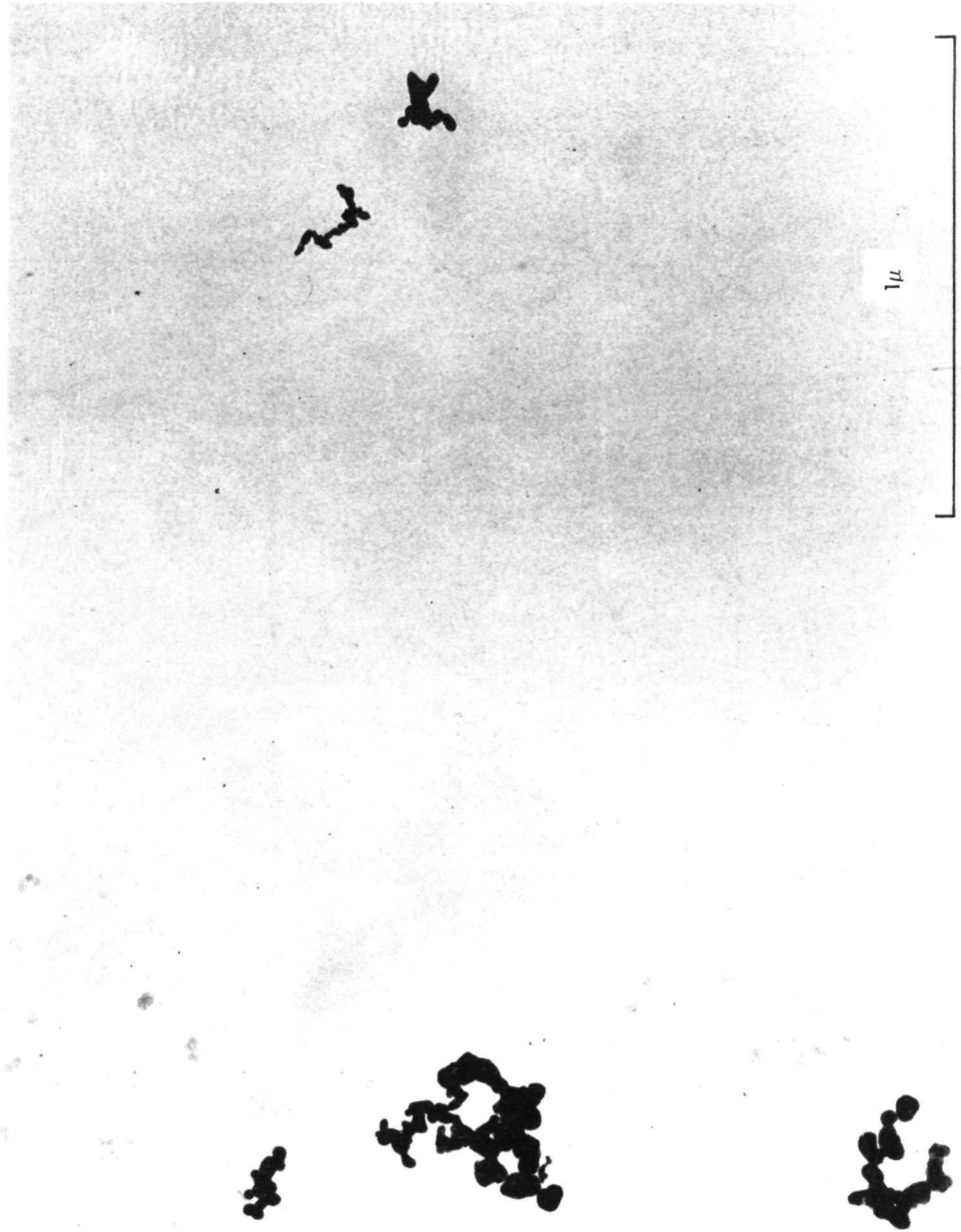
COLLECTOR GRID — 3 mm DIAM



MAGNIFIED ELECTRON PHOTOMICROGRAPH OF TUNGSTEN PARTICLES COLLECTED ON GRID AFTER DISCHARGE FROM PARTICLE FEEDER SYSTEM

SEE FIG. 27 FOR SCHEMATIC OF PARTICLE FEEDER SYSTEM

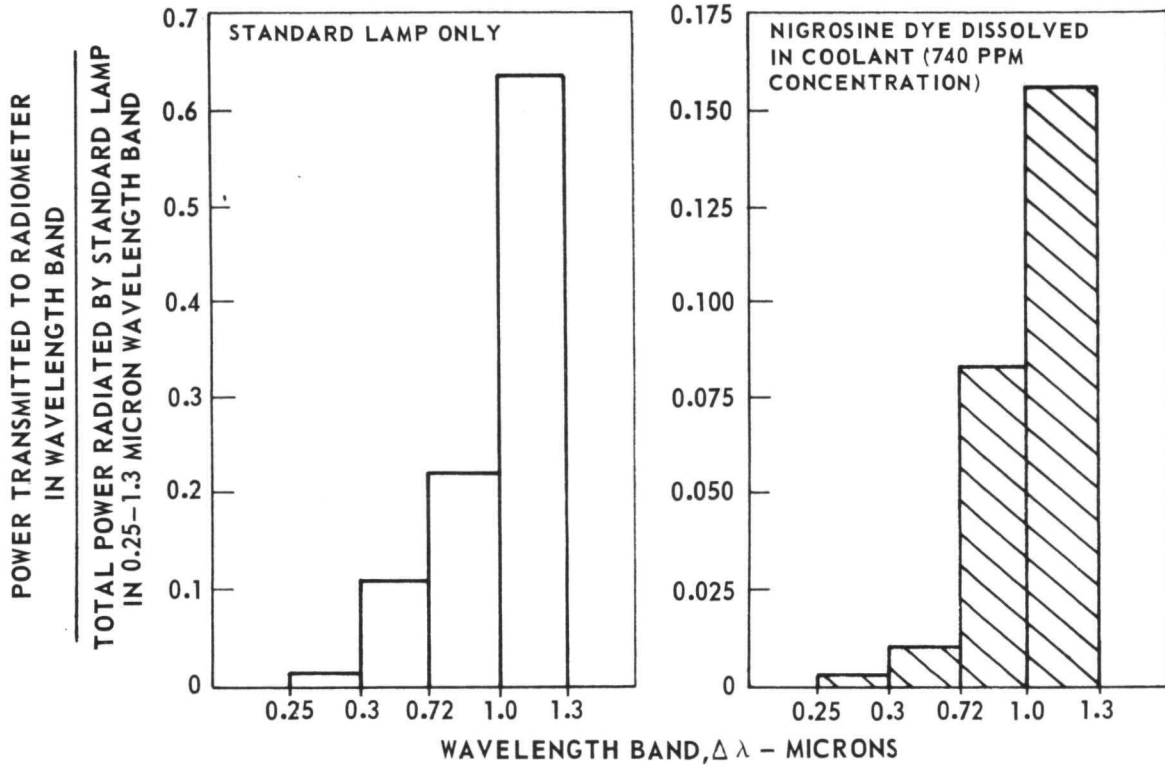
MAGNIFICATION -  $6.3 \times 10^3$



### SUMMARY OF WATER-DYE COOLANT RADIATION ATTENUATION CHARACTERISTICS

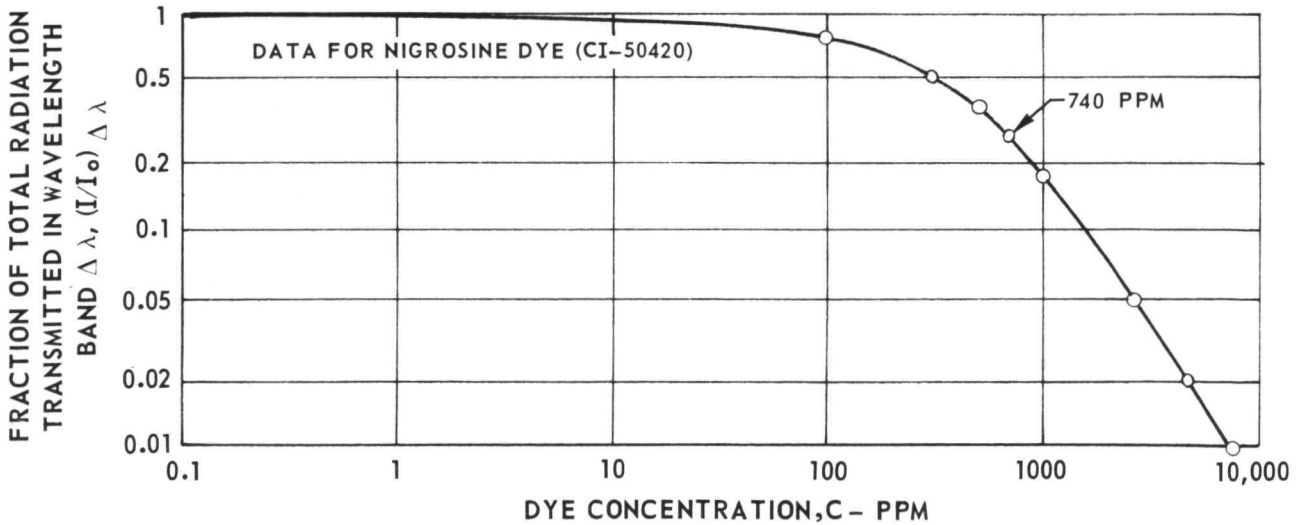
REFER TO APPENDIX B FOR DISCUSSION

(a) COMPARISON OF RELATIVE POWER TRANSMITTED THROUGH WATER-DYE COOLANT



(b) EFFECT OF DYE CONCENTRATION ON RADIATION ATTENUATION IN WATER-DYE COOLANT

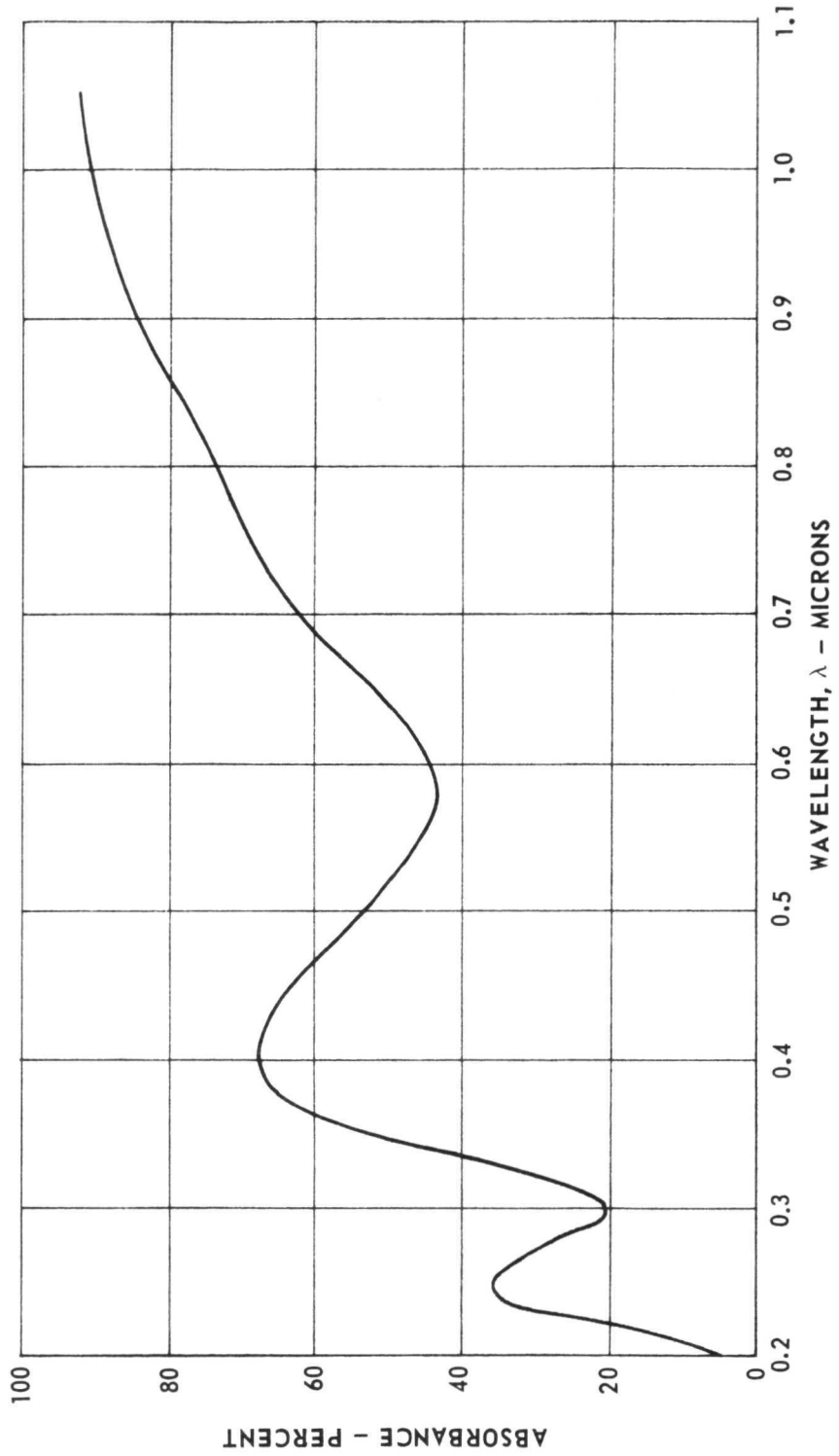
RF PLASMA SOURCE  
 PATH LENGTH = 2 MM  
 $\Delta \lambda = 0.25 \text{ TO } 1.3 \mu$



**ABSORBANCE OF NIGROSINE DYE IN THE WAVELENGTH BAND  
FROM 0.2 TO 1.1 MICRONS**

REFER TO APPENDIX B FOR DISCUSSION

PATH LENGTH = 1 CM



**United  
Aircraft  
Research  
Laboratories**



EAST HARTFORD, CONNECTICUT 06108